Assimilation de données satellitaires géostationnaires dans des modèles atmosphériques à aire limitée pour la prévision du rayonnement solaire en région tropicale

Frederik Kurzrock

UNIVERSITÉ DE LA RÉUNION

ECOLE DOCTORALE SCIENCES, TECHNOLOGIES ET SANTÉ

Assimilation de données satellitaires géostationnaires dans des modèles atmosphériques à aire limitée pour la prévision du rayonnement solaire en région tropicale

T H È S E

en vue de l'obtention du grade de

Docteur de l'Université de La Réunion

Spécialité: Physique atmosphérique

soutenue le 29/05/2019 par

Frederik KURZROCK

Jury:

Président:	Laurent LINGUET	-	Professeur, Université de Guyane
Rapporteurs:	Susanne CREWELL	-	Professeure, Université de Cologne, Allemagne
	Philippe BLANC	-	Directeur de Recherches, MINES ParisTech
Examinateur:	Roland POTTHAST	-	Professeur, Université de Reading, Royaume-Uni
Directeur:	Gilles LAJOIE	-	Professeur, Université de La Réunion
Co-directeur:	Fabrice CHANE MING	-	Maître de conférences HDR, Université de La Réunion
Invité:	Sylvain CROS	-	Docteur, Reuniwatt SAS

For my dear friend, colleague, and life coach Samuel Lalire.

Abstract

The variability of solar irradiance necessitates to limit the instantaneous feed-in of solar power to electricity grids. An improvement of solar irradiance forecasts would allow to increase the defined threshold limits, especially in non-interconnected zones such as Reunion Island. Achieving higher forecast accuracy is particularly challenging in the case of tropical islands due to pronounced convection and local thermal circulations. Limited-area numerical weather prediction (NWP) models allow to forecast cloud processes and solar irradiance at high spatio-temporal resolutions of a few kilometres and minutes. Nevertheless, they often fail to accurately predict cloudiness evolution and thus tend to overestimate solar irradiance. Refining the initial conditions of regional models in terms of clouds is an efficient means for improving short-term cloud cover and irradiance forecasts. The assimilation of geostationary meteorological satellite observations can achieve this improvement. Nevertheless, a variety of satellite data assimilation (DA) approaches exist and research has focused on mid-latitudes so far. This thesis deals with the assimilation of geostationary satellite observations with limited-area models in the southwestern Indian Ocean. In a first step, the state of the art in terms of existing approaches for radiance and cloud property retrieval assimilation with regional-scale models is reviewed. In consequence, one of the most promising approaches is identified and applied to the southwestern Indian Ocean. In the performed experiments, multi-phase cloud water path retrievals from NASA Langley's SatCORPS cloud products are assimilated with an ensemble Kalman filter using the Weather Research and Forecasting model. A 41-member ensemble at 12 km grid spacing is applied with a DA cycling interval of 6 hours. The Data Assimilation Research Testbed and its forward operator for cloud water path are used to assimilate gridded cloud water retrievals in the ice, supercooled liquid, and liquid phase. The impact of this assimilation approach on forecasts of global horizontal irradiance (GHI) is evaluated for austral summer 2017/2018 using pyranometer observations on Reunion Island. A distinct positive impact of the applied method on the first 14 hours of GHI forecasts is found. Different aspects of the forecast improvement due to DA are analysed by means of control experiments without DA, experiments with a nested domain at 4 km grid spacing, and a comparison with operational NWP models. As the utilised gridded cloud products are available globally, the method offers a portable and globally applicable approach that may also be evaluated for other regions of the Earth.

Keywords: Satellite data assimilation, solar irradiance forecasting, numerical weather prediction, limited-area models, geostationary meteorological satellite observations, tropical environment

Résumé

La variabilité de l'énergie solaire impose de limiter sa fraction d'injection instantanée dans le réseau électrique. Une amélioration des prévisions de l'ensoleillement conduirait à élever la limite de ce seuil, spécialement dans les zones non-interconnectées comme La Réunion. Une plus haute précision de prévision est particulièrement difficile à atteindre dans le cas des îles tropicales à cause de la convection prononcée et des circulations thermiques complexes au niveau local. Les modèles de prévision numérique du temps à aire limitée permettent de prévoir les processus liés aux nuages et l'éclairement solaire à de hautes résolutions spatio-temporelles, de l'ordre de quelques kilomètres et minutes. Néanmoins, ces modèles parviennent rarement à prévoir précisément l'évolution de la couche nuageuse et ont donc tendance à surestimer l'éclairement solaire. L'affinement des conditions initiales nuageuses des modèles régionaux par l'assimilation d'observations de satellites météorologiques géostationnaires est un moyen efficace pour améliorer les prévisions à court terme. Toutefois, une grande variété d'approches pour l'assimilation des données satellitaires existe et, jusqu'à présent, la recherche s'est concentrée sur les moyennes latitudes. Cette thèse aborde l'assimilation d'observations de satellites géostationnaires avec des modèles à aire limitée dans le sud-ouest de l'Océan Indien. Dans un premier temps, l'état de l'art des approches existantes pour l'assimilation de luminances observées et de propriétés physiques des nuageuse avec les modèles régionaux est dressé. Puis, l'une des approches les plus prometteuses est identifiée et appliquée au sud-ouest de l'Océan Indien. Dans les expériences effectuées, la concentration des nuages en eau est obtenue à partir des produits de propriétés nuageuses SatCORPS de la NASA. Ces observations sont assimilées avec un filtre de Kalman d'ensemble et le modèle Weather Research and Forecasting. Un ensemble de 41 membres et un espacement horizontal des points de grille de 12 km est appliqué avec un intervalle de cyclage de 6 heures pour l'assimilation. Le Data Assimilation Research Testbed et son opérateur d'observations de teneur en eau des nuages sont utilisés pour l'assimilation d'observations dans les phases solide, surfondue, et liquide. L'impact de cette approche d'assimilation sur des prévisions de l'éclairement horizontal global est évalué pour l'été austral 2017/2018 en utilisant des observations de pyranomètres sur l'île de La Réunion. Un effet positif de la méthode appliquée sur les prévisions de l'éclairement est constaté surtout pour les 14 premières heures de prévision. Différents aspects de l'amélioration des prévisions, grâce à l'assimilation de données, sont analysés par le biais d'expériences témoins sans assimilation, d'expériences avec un domaine de grille imbriquée avec un espacement horizontal des points de grille de 4 km et d'une comparaison avec des modèles opérationnels. Les observations quadrillées utilisées étant disponibles à l'échelle mondiale, la méthode offre une approche applicable et évaluable pour d'autres régions du monde.

Mots-clés : Assimilation de données satellitaires, prévision de l'irradiance solaire, prévision numérique du temps, modèle à aire limitée, observations de satellites météorologiques géostationnaires, milieu tropical

Zusammenfassung

Präzisere Vorhersagen der solaren Einstrahlung sind erforderlich um eine höhere Einspeisung von Photovoltaik in Stromnetze zu ermöglichen. Dies gilt insbesondere für nichtverbundene Stromnetze wie das der französischen Insel La Réunion im Indischen Ozean. Ausgeprägte Konvektion und lokale thermische Zirkulationen erschweren es, Wettervorhersagen für tropische Inseln wie La Réunion zu verbessern. Regionale Wettervorhersagemodelle ermöglichen es, Wolken und die solare Einstrahlung mit hohen Auflösungen von wenigen Kilometern und Minuten vorherzusagen. Allerdings gelingt die genaue Vorhersage der Bewölkung nicht immer, was oft zu einer Überschätzung der Einstrahlung führt. Die Verfeinerung der Anfangsbedingungen solcher Modelle ist ein wirksames Mittel um kurzfristige Vorhersagen der Bewölkung und der Einstrahlung zu verbessern. Durch die Assimilation von Beobachtungen geostationärer Satelliten kann diese Verbesserung erreicht werden. Dazu gibt es jedoch eine Vielzahl an Herangehensweisen, die bislang hauptsächlich für die mittleren Breiten ausgewertet wurden. Diese Dissertation befasst sich mit der Assimilation der Beobachtungen geostationärer Satelliten mit Regionalmodellen im südwestlichen Indischen Ozean. Zunächst wird der Stand der Forschung hinsichtlich existierender Konzepte zur Assimilation von Satelliten-Rohdaten sowie abgeleiteter Produkte über Wolkeneigenschaften mit Ausschnittsmodellen inspiziert. Dies führt zur Identifizierung einer der vielversprechendsten Herangehensweisen, die im Anschluss auf den südwestlichen Indischen Ozean angewandt wird. Dabei wird der Wolken-Wassergehalt in verschiedenen Aggregatzuständen dem SatCORPS Datensatz der NASA entnommen und mittels eines Ensemble Kalman Filters in das Weather Research and Forecasting Modell assimiliert. Das Ensemble bestehet aus 41 Mitgliedern mit einer Maschenweite von 12 km und hat ein Aktualisierungsintervall von 6 Stunden. Zur Assimilation der Beobachtungen des eisförmigen, unterkühlten, und flüssigen Wolken-Wassergehaltes wird der Vorwärtsoperator des Data Assimilation and Research Testbeds verwendet. Die Auswirkungen dieser Methode auf Vorhersagen der solaren Einstrahlung werden mittels Pyranometer-Beobachtungen auf La Réunion für den südlichen Sommer 2017/2018 ausgewertet. Ein deutlicher, positiver Effekt der Methode auf die ersten 14 Stunden der Vorhersage ist festzustellen. Verschiedene Aspekte werden analysiert, ermöglicht durch Kontroll-Experimente ohne Datenassimilation, Experimente mit einem verschachtelten Modellgebiet bei 4 km Maschenweite, und einen Vergleich mit operationellen Wettermodellen. Da die verwendeten, gerasterten Beobachtungen weltweit verfügbar sind, stellt die angewandte Methode eine portable Lösung dar, die auch für andere Regionen der Erde angewandt werden kann.

Schlüsselwörter: Assimilation von Satellitendaten, Vorhersage der solaren Einstrahlung, numerische Wettervorhersage, Regionalmodelle, Beobachtungen von geostationären Wettersatelliten, tropische Umgebung

Acknowledgements

After three exciting years I would like to thank all actors who have helped me in carrying out this work.

First of all, I wish to thank the jury, notably the two reviewers Susanne Crewell and Philippe Blanc, for carefully reviewing the manuscript and for their excellent remarks and questions.

This work is the result of a collaboration between Université de La Réunion and Reuniwatt. Therefore, I want to thank these two institutions for their contribution in preparing and realising this thesis.

I would like to express my gratitude to my supervisors Gilles Lajoie, Fabrice Chane Ming, Laurent Linguet and Sylvain Cros. Without their guidance and persistent help this thesis would not have been possible. I appreciate your scientific advice, your words of motivation, and the excellent and honest communication. Thanks to you, I always felt at ease and well taken care of and got much food for thought and many impulses for my personal development. I am also grateful for the support and encouragement of the members of Espace-Dev Reunion and its director Gwenaëlle Pennober. Thank you for accommodating me in this exciting interdisciplinary institution.

I owe my deepest gratitude to Nicolas Schmutz, the visionary founder and CEO of Reuniwatt, for encouraging me to do this thesis, for providing the financial means, and for giving me the opportunity to be part of the Reuniwatt fellowship. I received generous support from my amazing colleagues at Reuniwatt and I am proud to be part of this dynamic team. More specifically, I owe a very important debt to Niolas Sébastien for being my dream catcher in the seemingly endless nightmare of French administration. Your admirable persistence and diplomatic skills helped me untangle the knots of bureaucracy from the very beginning to the very end. I would also like to show my greatest appreciation to James Ringuin-Velleyen, the master of bits and bytes. Without your masterly IT support it would not have been possible for me to perform my experiments to this extent. Special thanks also to the interns that I had the pleasure to supervise in the course of my thesis: Norman Steinert, Benjamin Mairand, Hannah Nguyen and Jerome Sauer. Thanks a lot for your excellent work and your valuable contributions.

I have greatly benefited from my visits at the data assimilation and model development team at Deutscher Wetterdienst (DWD) under the supervision of Roland Potthast. Even if my COSMO-KENDA experiments have not found their way into the manuscript, during my research stays in Offenbach I learned a lot of useful things for the further course of the thesis, and I enjoyed the lovely work climate and inspiring atmosphere.

Advice and comments given by Jason Otkin and William Lewis from the University of Wisconsin-Madison has been a great help in setting up the WRF-DART experiments that have been carried out. In retrospect, becoming acquainted with Jason in Reading was a key moment in the course of the thesis.

Furthermore, I am grateful for the help of Nancy Collins and Glen Romine from the DART team at NCAR who kindly and thoroughly answered a long list of questions.

Thanks also goes to Thomas Jones from the University of Oklahoma who provided a lot of useful information about the CWP forward operator.

Moreover, I would like to thank Rabindra Palikonda, William L. Smith and Patrick Minnis from the NASA Langley Research Center for their technical support regarding the SatCORPS data and the fruitful discussions.

I would like to express the deepest appreciation to my family, notably my parents who always supported me during these long years of studies. My heartfelt appreciation also goes to Caroline, for her patience and warm support throughout the years. I am looking forward to writing the next chapter with you.

Finally, I would like to thank all those I did not mention explicitly for supporting me on my path.

List of Abbreviations

3D-Var	Three-dimensional variational data assimilation
3DEnVar	Three-dimensional ensemble–variational data assimilation
4D-Var	Four-dimensional variational data assimilation
ABEI	Adaptive background error inflation
ABI	Advanced Baseline Imager, the primary instrument aboard the GOES-R series of environmental satellites
ADAS	ARPS Data Analysis System
AMVs	Atmospheric motion vectors
ANN	Artificial neural network
AOEI	Adaptive observation error inflation
AROME	Application de la Recherche à l'Opérationnel à Méso-Échelle
ARPS	Advanced Regional Prediction System
ARW	Advanced Research WRF
BT	Brightness temperature
CBP	Cloud base pressure
CEP	Cloud effective pressure
CERES	Clouds and the Earth's Radiant Energy System
CIMSS	Cooperative Institute for Meteorological Satellite Studies
CLDDA	A cloud analysis method for WRF named CLouD Data Assimilation
CMVs	Cloud motion vectors
COSMO	COnsortium for Small-scale MOdeling
CRAS	CIMSS Regional Assimilation System
CRE	Commission de régulation de l'énergie
CRTM	Community Radiative Transfer Model
CSP	Concentrated solar power
CTH	Cloud top height
CTP	Cloud top pressure
CTT	Cloud top temperature
CWP	Cloud water path
DA	Data assimilation
DART	Data Assimilation Research Testbed
DHI	Diffuse horizontal irradiance
DNI	Direct normal irradiance
DWD	Deutscher Wetterdienst - the German meteorological service
ECA	Effective cloud amount
ECMWF	European Centre for Medium-Range Weather Forecasts
EnKF	Ensemble Kalman filter
ENSO	El Niño–Southern Oscillation
ESD	Empirical-statistical downscaling

ESRA	European Solar Radiation Atlas
EUMETSAT	European Organisation for the Exploitation of Meteorological Satellites
G3C	NASA Langley's Global Geostationary Gridded Cloud products, a former name for SatCORPS
GCM	Global circulation model
GDAS	Global Data Assimilation System
GEFS	Global Ensemble Forecast System
GFS	Global Forecast System
GHI	Global horizontal irradiance
GOES	Geostationary Operational Environmental Satellite
GSI	Gridpoint Statistical Interpolation
GTI	Global tilted irradiance
HIRLAM	HIgh Resolution Limited Area Model
ICON	ICOsahedral Nonhydrostatic model, DWD's global model
ICs	Initial conditions
IDW	Inverse distance weighting
IFS	Integrated Forecasting System, ECMWF's global model
IR	Infrared spectrum
IWP	Ice water path
JMA	Japan Meteorological Agency
JMA-NHM	JMA non-hydrostatic model
KENDA	The Kilometre-scale ENsemble Data Assimilation system of DWD
LAM	Limited-area model
LAPS	Local Analysis and Prediction System
LBCs	Lateral boundary conditions
LETKF	Local ensemble transform Kalman filter
LWP	Liquid water path
MAE	Mean absolute error
MBE	Mean bias error or simply bias
MJO	Madden-Julian Oscillation
MLEF	Maximum likelihood ensemble filter
MM5	PSU-NCAR's Mesoscale Model version 5, the predecessor to the WRF model
MMR	Multivariate Minimum Residual scheme
MODIS	MODerate-resolution Imaging Spectroradiometer
MOPS	Moisture Observation Preprocessing System
MPEF	Meteorological Products Extraction Facility
MSG	Meteosat Second Generation
MTG	Meteosat Third Generation
NAE	North Atlantic/European model, formerly operated by UKMO
NASA	National Aeronautics and Space Administration
NCAR	National Center for Atmospheric Research

NCEP	National Centers for Environmental Prediction
NIR	Near infrared spectrum
NOAA	National Oceanic and Atmospheric Administration
NWP	Numerical weather prediction
OCA	MPEF's Optimal Cloud Analysis product
OSSE	Observing system simulation experiments
pdf	Probability density function
POA	Plane of array
PSU	Pennsylvania State University
PV	Photovoltaics
QPF	Quantitative precipitation forecast
RAMDAS	Regional Atmospheric Modeling Data Assimilation System
RAMS	Regional Atmospheric Modeling System
RAP	RAPid refresh model
RMSE	Root mean squared error
RTM	Radiative transfer model
RTTOV	Radiative Transfer for TOVS
RUC	Rapid Update Cycle model
SatCORPS	NASA Langley's Satellite ClOud and Radiation Property retrieval System
SEVIRI	Spinning Enhanced Visible and InfraRed Imager - one of the instruments aboard the MSG series of EUMETSAT satellites
SWIO	Southwestern Indian Ocean
SWP	Supercooled water path
SZA	Solar zenith-angle
TIROS	Television and InfraRed Observation Satellite
TOVS	TIROS Operational Vertical Sounder
TSO	Transmission system operator
TSPRD	Total spread
UKMO	UK Met Office
VAS	VISSR Atmospheric Sounder
VIS	Visible spectrum
VISSR	Visible and Infrared Spin Scan Radiometer
WDM6	WRF double moment 6-class microphysics scheme
WP	Water path
WPS	WRF Preprocessing System
WRF	Weather Research and Forecasting model
WRFDA	WRF model data assimilation system
WV	Water vapour

Contents

Chapter 1

Introduction

Contents

Summary

The growth of the global total installed photovoltaic capacity is accompanied by an increasing need for more accurate short-term solar power forecasts. Those are especially important in the tropics, where the solar potential and the variability of solar irradiance reach their maximum. In the southwestern part of the Indian Ocean, the study region of this thesis, pronounced convection makes short-term cloud and solar irradiance forecasting challenging. Limited-area numerical weather prediction models have the potential to forecast cloud and radiation processes in the order of kilometres and minutes. Nevertheless, the accuracy of irradiance forecasts depends on the quality of the forecasts' initial conditions. As conventional in-situ observations are sparse in the study region, meteorological geostationary satellites provide valuable observations that can frequently be assimilated into LAMs. The context related to the work presented in this thesis is provided in this chapter. Three research questions, to be answered in the course of the thesis, are raised. Moreover, three main objectives are defined. The overall objective of this thesis is the improvement of solar irradiance forecasts in the southwestern Indian Ocean using limited-area NWP and geostationary satellite data assimilation (DA).

1.1 The context of photovoltaic power

In 2017, 99.1 GW of grid-connected photovoltaic (PV) power was installed worldwide making PV the fastest growing power generation source in the world. The global total installed PV capacity has exceeded 400 GW in 2017 (figure 1.1) and is expected to exceed 1 TW in 2022. Eight countries are expected to add at least 20 GW between 2018 and 2022 - China, India, USA, Japan, Spain, Germany, Australia, and Mexico (Schmela et al., 2018).

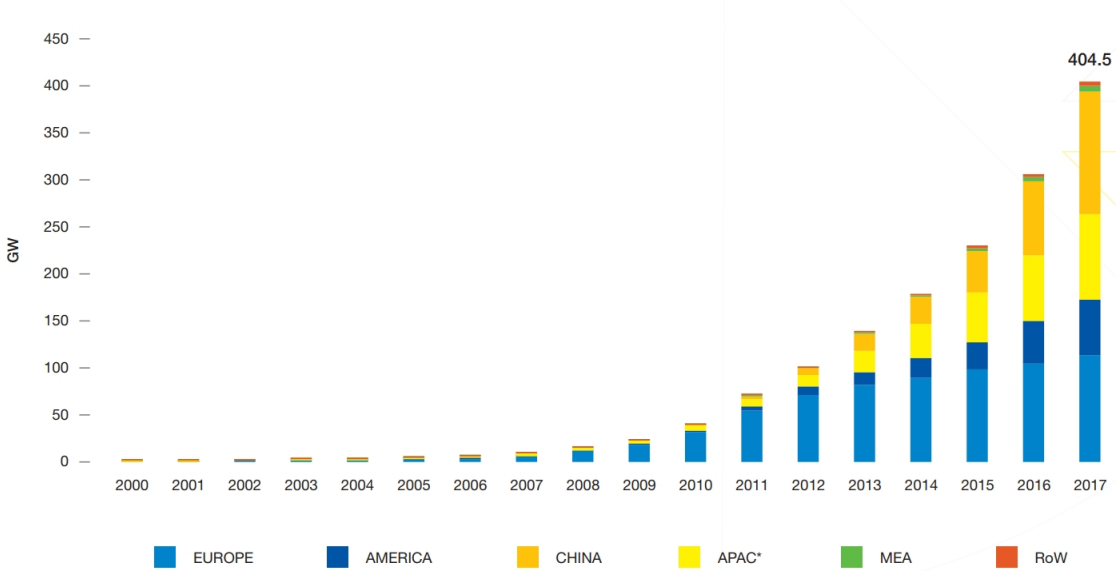

Figure 1.1 – Evolution of the global total installed PV capacity in 2000-2017. Europe is shown in light blue, America in dark blue, China in orange, the Asia Pacific (APAC) states (excluding China) in yellow, the Middle East and Africa (MEA) in green and the rest of the world (RoW) in red. Figure taken from Schmela et al. (2018). © 2018 SolarPower Europe.

An increase of the installed PV capacity over the last years has also happened in non-interconnected zones like the French overseas department Reunion Island in the southwestern Indian Ocean (SWIO) where the total installed PV capacity reached 186.4 MW in 2016 (SPLEnergiesRéunion, 2018). Being located in the tropics, the potential yield for PV is high on Reunion Island where up to 2900 annual sunshine hours are reached at some locations (Bessafi et al., 2018). Nevertheless, the increase of the installed PV capacity is stagnant (figure 1.2).

This may partly be explained by the defined limit of 30 % of instantaneous power injection (or "feed-in") of renewable energies in the energy mix that had been established in consequence of a decree of the Energy Regulatory Commission (Commission de régulation de l'énergie; CRE) issued 23rd April 2008 for non-interconnected zones in France (CRE, 2018). The PV feed-in currently needs to be limited because the variability of renewable energies can have a significant impact

on the stability of electric grids. The fundamental principle for the operation of power systems is that demand and supply are balanced. In mainland Europe, the normal power system operating frequency is 50 Hz. Above and below the limits of approximately 50.5 Hz and 49.5 Hz, a blackout is likely to happen and power does not reach the end users (Fox et al., 2007).

On Reunion Island the initial limit of 30 % of renewables feed-in had been increased to 35 % in 2018 and an increase to 45 % by 2023 is aimed for (DEAL-Réunion, 2017). Further reasons for the stagnation of the installed PV capacity on Reunion Island are decreasing feed-in tariffs, high costs of transport and local taxes, a lack of incentive access to credit for consumers, a lack of land for PV development, and a lack of coordination between authorities (Praene et al., 2012).

Besides the installation of energy storages, solar power forecasting allows to better handle variability and may help to increase the 35 % threshold in the future (CRE, 2014). Consequently, more accurate solar power forecasts are required in order to allow non-interconnected zones like Reunion Island to increase the PV feed-in and follow the global trend of an energy transition towards renewables.

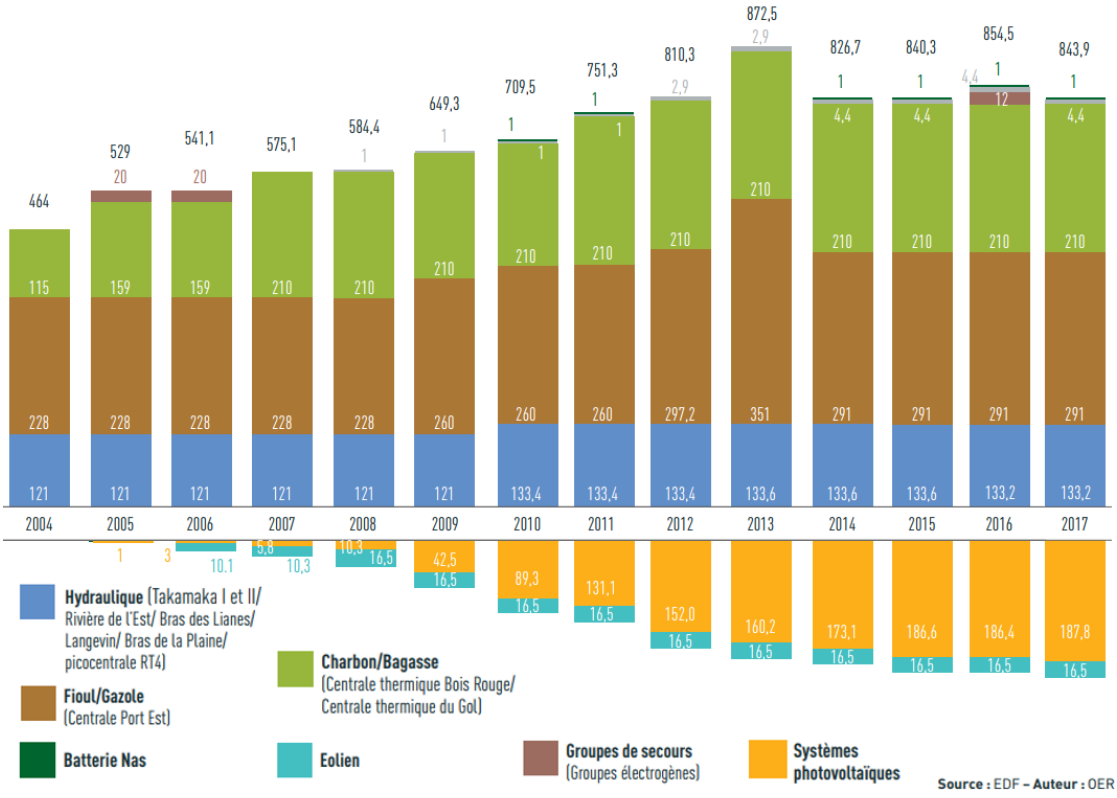

Figure 1.2 – Evolution of energy sources on Reunion Island in 2000-2017 in MW. Wind energy is shown in turquoise, PV in yellow, hydro energy in blue, fuel in golden brown, coal and bagasse in green, backup power generators in toast brown, biogas in grey and sodium-sulfur (NaS) batteries in dark green. Original figure adapted from SPLEnergiesRéunion (2018). Source: EDF. Author: oer.

1.2 Solar irradiance and power forecasting

PV systems convert solar radiation into electricity. The electricity production of a PV module therefore depends on the solar radiation arriving at its surface. Solar irradiance is a radiant flux density with the SI unit $\mathrm{W\,m^{-2}}$. In the context of solar power, it is commonly distinguished between different components of solar radiation arriving at the Earth's surface that are illustrated in figure 1.3. The direct normal irradiance (DNI) is the solar-beam radiation measured on a surface perpendicular to the Sun (figure 1.3 (a)). The diffuse horizontal irradiance (DHI) is the diffuse solar radiation measured on a horizontal surface (figure 1.3 (b)). It is a product of atmospheric scattering by clouds, aerosols and other atmospheric constituents. The global horizontal irradiance (GHI) is the total downward solar irradiance on a horizontal surface (figure 1.3 (c)) and is related to the components DNI and DHI by the equation:

$$GHI = DNI \times cos(SZA) + DHI \tag{1.1}$$

with SZA being the solar-zenith angle, i.e. the angle between the zenith and the centre of the Sun's disc.

Another variable that is crucial for PV is the global tilted irradiance (GTI) or plane of array (POA) irradiance (figure 1.3 (d)), describing the solar radiation measured on an inclined surface with any orientation, e.g. a PV module. GTI can be derived from DNI and DHI, and knowing the radiation reflected from the ground. More information about solar irradiance in the context of PV power can be found in Kleissl (2013) and Sengupta et al. (2017).

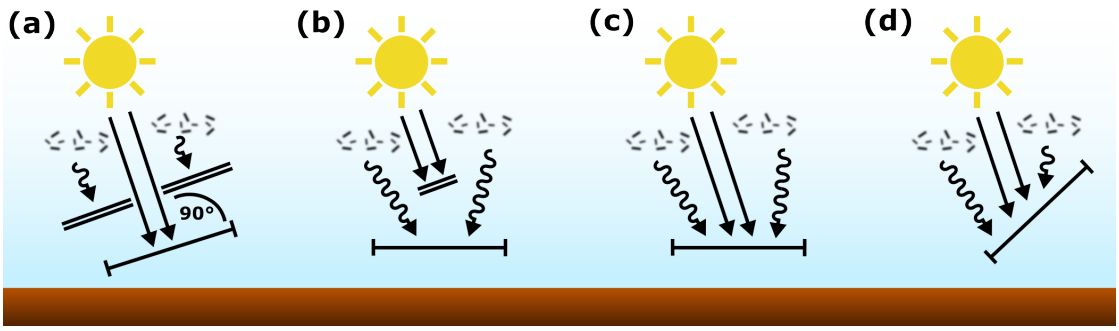

Figure 1.3 – Solar irradiance arriving at the Earth's surface: direct normal irradiance (DNI) (a), diffuse horizontal irradiance (DHI) (b), global horizontal irradiance (GHI) (c), and global tilted irradiance (GTI) (d).

Several factors affect the electricity production of a PV module. Besides the specific module performance and environmental factors such as shading, PV power mainly varies as a function of solar irradiance and PV module temperature. Wind can cause cooling of the PV modules and therefore also plays a role. Figure 1.4

illustrates the relationship between PV power, GTI and the PV module temperature. It is shown that at a given GTI of 800 W m^{-2} the spread of power production amounts to approximately 200 kW as a result of different PV module temperatures. While solar irradiance can vary by several hundred W m^{-2} within a few minutes, temperature is a more stable meteorological parameter, but its impact is not neglectable. Consequently, the variability of PV power is mainly dependent on the variability of solar irradiance. Hence, this thesis exclusively deals with GHI forecasts, since an improvement of these forecasts naturally has positive impacts on solar power forecasts.

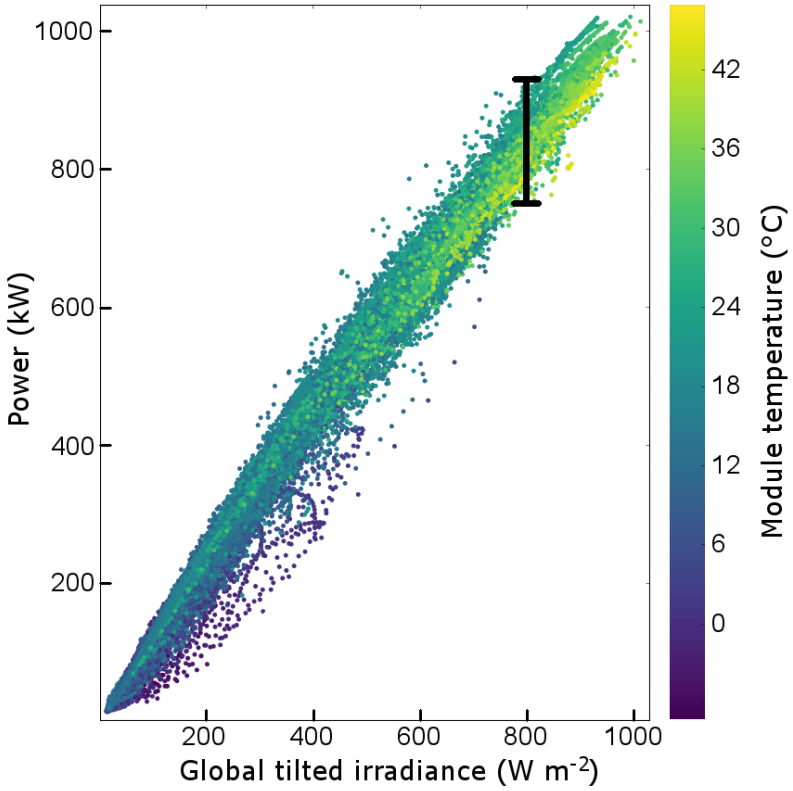

Figure 1.4 – Hourly means of PV power as a function of GTI and PV module temperature for a PV plant in southern France during several months. The black bar indicates the spread of power production at a given GTI of 800 W m^{-2} depending on PV module temperature. Source: Reuniwatt.

While aerosols, ozone, oxygen, nitrogen oxides, water vapour, carbon dioxide and other minor atmospheric components are known to affect the solar irradiance arriving at the Earth's surface by scattering and absorption, clouds can cause a significant reduction as well as sudden changes and pronounced variability of solar irradiance at ground level (Blanco and Malato, 2009).

The variability of irradiance, and subsequently PV power, along with the global increase of total installed PV capacity result in a growing need for solar power

forecasts. The users of such forecasts are utility companies, transmission system operators (TSOs), energy service providers, energy traders, and individual power producers (Diagne et al., 2013).

Depending on the forecast lead time and the forecast user requirements, different observation sources and forecasting methods are used to produce solar irradiance forecasts (Diagne et al., 2013; Sengupta et al., 2017). Up to a forecast horizon of roughly 30 minutes, ground-based sky imagers, that are installed on-site, typically provide the highest accuracy. A sky imager takes pictures of the sky on which clouds and the sun can be identified (figure 1.5 (a)). Subsequently, the motion of the clouds can be analysed and extrapolated to the future. Knowing the position of the sun, this eventually allows to generate solar irradiance forecasts (Liandrat et al., 2017).

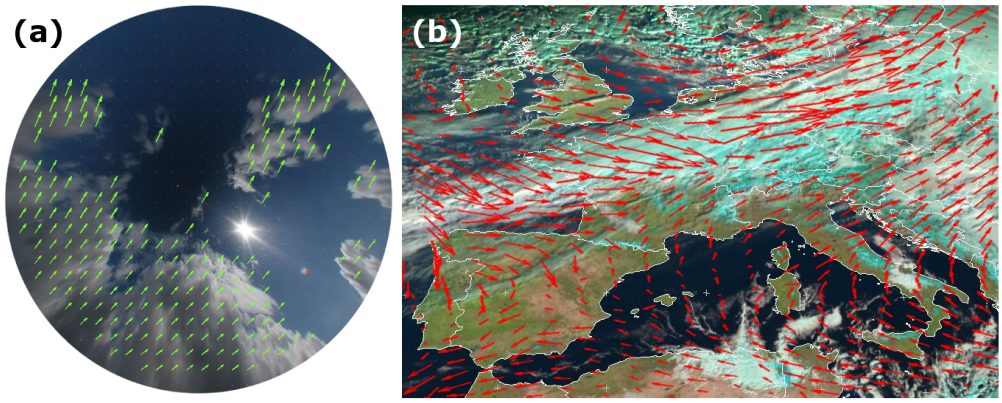

Figure 1.5 – Illustration of intraday cloud and solar irradiance forecasting methods. Visible images of the sky dome from a ground-based sky imager allow to derive cloud motion vectors (green) and extrapolate cloud motion (a). In a similar manner, cloud motion vectors (red) can be derived using satellite images (b), allowing to forecast the next hours ahead. Source: Reuniwatt.

Geostationary meteorological satellites are the most adequate source of cloud observations for forecasts with lead times of approximately 30 minutes to 6 hours ahead. Satellite images allow to identify clouds on scales that are larger than those of sky imagers (figure 1.5 (b)). In a similar manner than sky imager forecasting methods, the motion vectors of the clouds can be determined from consecutive satellite images. The satellite observations also allow to derive solar irradiance at ground level and irradiance forecasts can be produced by cloud motion extrapolation (Cros et al., 2018).

Beyond forecast lead times of 6 hours, numerical weather prediction (NWP) numerical weather prediction (NWP) models are currently the most suitable solution to provide forecasts of solar irradiance for up to approximately two weeks. NWP models are dynamical models that represent the atmosphere and a part of the Earth's surface on a three-dimensional grid (figure 1.6). A system of differen-

tial equations describing the physical and chemical atmospheric processes is solved numerically by a NWP model to predict the future state of the atmosphere. From a mathematical point of view, NWP is an initial-value problem: Knowing the present atmospheric state, the evolution of this state can be forecasted numerically (Kalnay, 2003). The computation of such a forecast on a supercomputer can take several hours, which is why the previously mentioned satellite-based methods for solar forecasting are more adequate than NWP models for forecast lead times of a few hours.

Figure 1.6 – Illustration of the difference in resolution between a GCM covering the whole globe, a LAM covering a defined region, and a nested LAM domain. Figure produced by Andreas Will.

It is commonly distinguished between global circulation models (GCMs), covering the whole globe, and regional-scale or limited-area models (LAMs), covering a defined region of the Earth. The maximal operational resolution of GCMs is limited since increasing the resolution also increases the computation time. The temporal and spatial resolutions of GCM output (typically more than 10 km and 1 hour) often do not permit accurate cloud forecasting since cloud processes occur over shorter temporal and spatial scales. LAMs compute the atmospheric state for a defined region of the Earth and require lateral boundary conditions (LBCs) at the border of the model domain. The LBCs are provided to the LAM by a GCM. This way, LAMs can use higher temporal and spatial resolutions than GCMs and potentially simulate cloud processes with more detail. Nevertheless, this may not always be the case, depending on the considered models and the local meteorological conditions. Consequently, a first research question arises:

Research question 1 *Do LAMs forecast ground-level solar irradiance more accurately than GCMs on Reunion Island?*

When talking about LAMs that use LBCs from a GCM to increase the spatio-temporal resolution of the NWP output, the term "dynamical downscaling" is often used. This term demonstrates the methodological difference to "statistical downscaling" that follows the same goal of increasing the resolution of meteorological parameters by applying statistical methods to NWP output. It is also possible to perform so-called "nesting" within the LAM domain to gradually increase the resolution by further "dynamically downscaling" the information (figure 1.6). However, the predictability of clouds is limited and increasing the model resolution to a computationally feasible maximum does not necessarily improve the forecast quality. Therefore, the second research question that arises is:

Research question 2 *What impact do high-resolution nested LAM domains have on GHI forecasts on Reunion Island?*

Since the influence of information provided by the GCM via the lateral boundaries of a LAM domain becomes larger with advancing forecast lead time, the information provided by the initial conditions vanishes at some point of the LAM forecast. This is why LAMs are typically used to forecast only a few number of days, while GCMs are used for longer forecast horizons (Kalnay, 2003).

For horizons of several months, seasonal prediction systems provide information that can be used to derive trends in solar irradiance (Copernicus, 2019). Figure 1.7 provides an overview and illustrates for which temporal and spatial scales the different solar forecasting methods apply. Statistical and machine learning methods are also used for all lead times, either additionally to the methods shown in the figure or for post-processing and blending of the different forecast sources. PV production data or on-site irradiance measurements are often used as an input for statistical forecasting or so-called "nowcasting" methods.

1.3 Solar forecasting in the tropics using NWP models

Many atmospheric and land surface processes are either too small-scaled, complex, poorly understood, or computationally expensive to be explicitely resolved by NWP models. The bulk effects of these processes are approximated by so-called physical parameterisation schemes (Stensrud, 2007). Figure 1.8 illustrates some of the processes that are typically parameterised in NWP models. The parameterisation of sub-grid scale processes induces important uncertainties of irradiance forecasts since these processes often cause a highly variable cloud cover within a given grid box.

As the downward solar irradiance at the ground level is strongly influenced by clouds, the ability of a given NWP model to forecast solar irradiance is closely

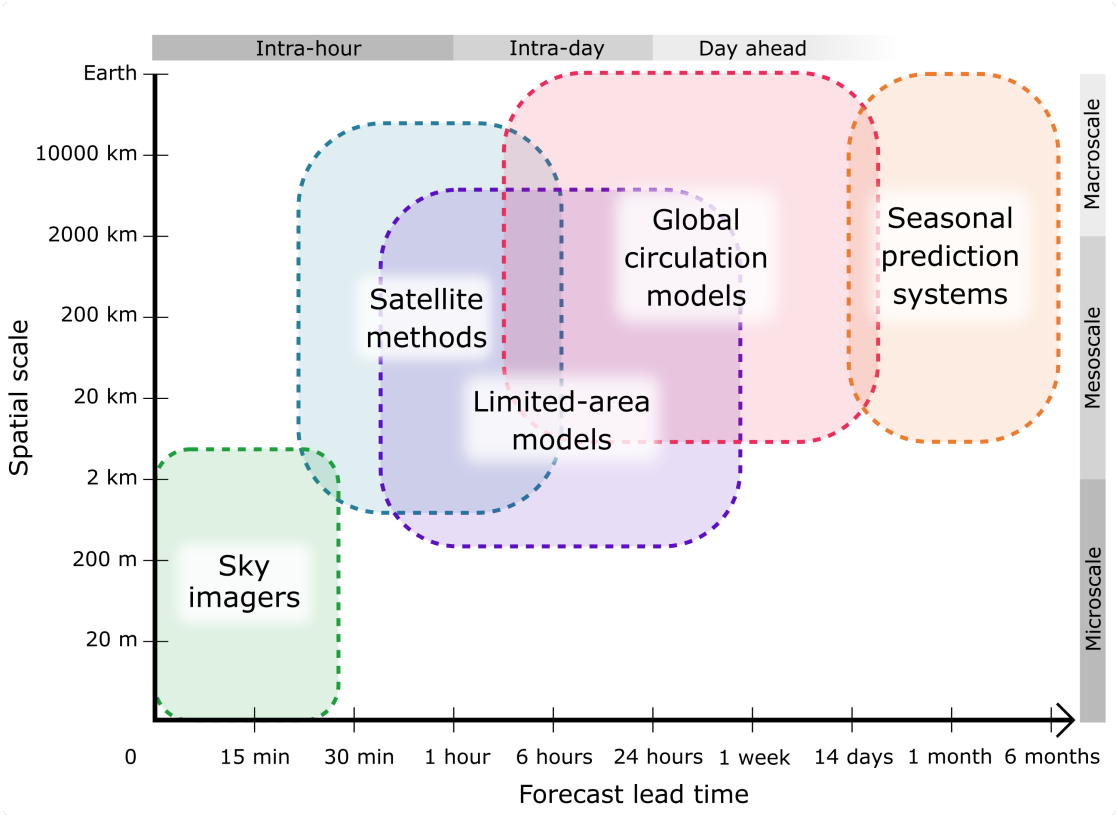

Figure 1.7 – Solar irradiance forecasting methods, the spatial scales at which they operate, and the forecast lead times to which they apply. Figure inspired by Diagne et al. (2013) and Sengupta et al. (2017).

linked to its ability to forecast cloudiness. One benefit of using LAMs for solar power forecasting is that the choice of the parameterisation schemes of such a model can be optimised for a certain geographical region and the model can be adapted to specific local PV forecasting requirements (López-Coto et al., 2013; Pérez et al., 2014).

Due to the parameterisation of complex and often non-linear cloud processes and associated impacts on radiation, NWP models tend to underestimate low-level cloud cover and thus overpredict solar irradiance at the surface. This concerns especially stratus clouds and coastal areas (Yucel et al., 2002; Inman et al., 2013; Haiden and Trentmann, 2015; Ruiz-Arias et al., 2016; Yang and Kleissl, 2016; Sahu et al., 2018). There are also large model uncertainties regarding the evolution of upper level cloudiness (Cintineo et al., 2014).

Among current initiatives to improve NWP models for solar power forecasting, the WRF-Solar project aims at taking the interactions between clouds, aerosols and radiation in the LAM named Weather Research and Forecasting (WRF) (Skamarock et al., 2008) better into account (Jimenez et al., 2016; Riihimaki et al., 2018). Besides, the choice and combination of various model settings, such as

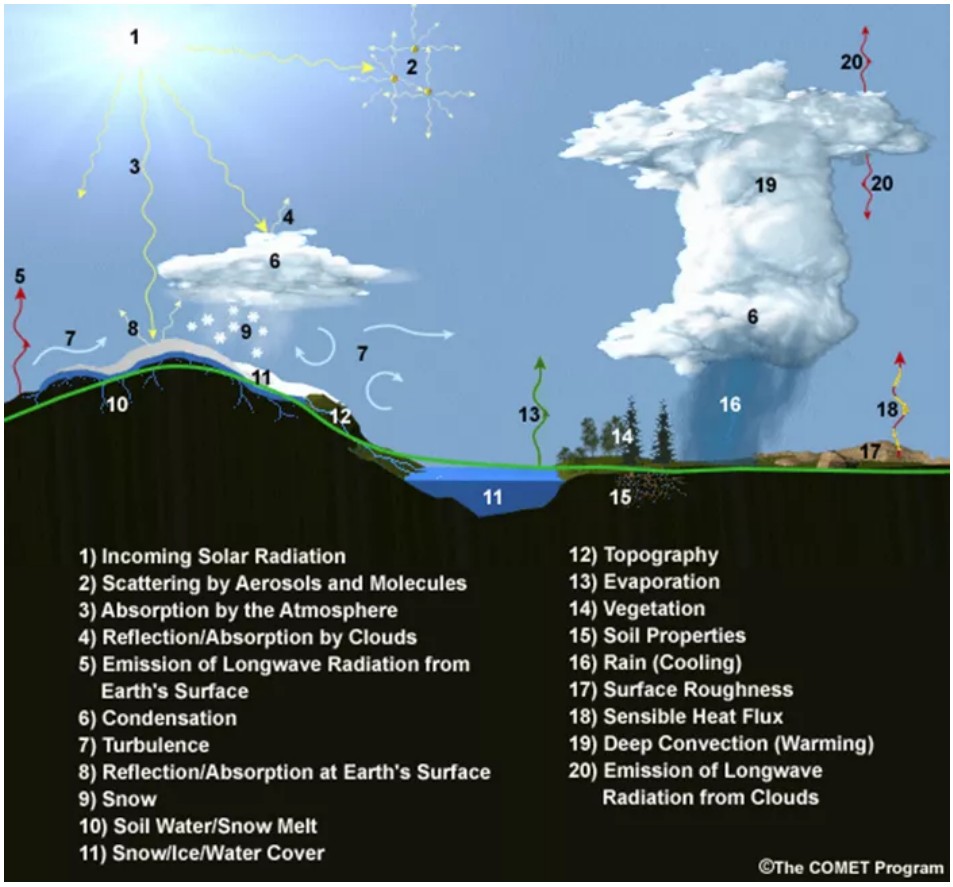

Figure 1.8 – Illustration of some of the atmospheric processes that are typically parameterised in NWP models. Image courtesy of MetEd, The COMET Program, UCAR.

convection, cloud microphysics, radiation and planetary boundary layer parameterisation, also influences the performance of NWP models (Otkin and Greenwald, 2008; López-Coto et al., 2013; Cintineo et al., 2014; Otkin et al., 2017).

In their review, Blaga et al. (2019) analyse a data set of 1705 entries of solar irradiance forecast evaluations in different climate zones and including different types of forecasting methods, e.g. statistical models, satellite and NWP based methods. The authors find that there is a reluctance in performing and evaluating day-ahead forecasts for tropical regions, compared to other regions. This underlines the importance of research question 1 and the need for comparison studies and evaluations of NWP model forecast accuracy in terms of GHI in the tropics.

In fact, achieving higher forecast accuracy for cloudiness is particularly challenging in tropical environments. Tropical air masses are generally more homogeneous than those in mid-latitudes and therefore lack distinct large-scale horizontal gradients of thermodynamic fields. The interplay of pronounced convection, local thermal circulations, and the trade winds complicates the prediction of cloud evolution (Beucher, 2010; Galvin, 2016).

On Reunion Island, solar irradiance forecast errors are especially pronounced in

the austral summer season (December-February) when convection is strong compared to winter (Badosa et al., 2015). Moreover, the specific topography of Reunion Island, with an elevation of up to 3069 m, results in an interplay of both breeze-induced clouds and orographic clouds due to the predominant south-easterly trade winds which are often extremely unpredictable.

Consequently, most of the recent studies in peer-reviewed literature that concern NWP models for solar irradiance forecasting in the tropics focus on post-processing methods (Diagne et al., 2014; Aryaputera et al., 2015; Badosa et al., 2015; Lauret et al., 2016; Lima et al., 2016; Verbois et al., 2018) rather than the direct improvement of NWP model accuracy. Their common goal is to refine NWP model output and thereby achieve a forecast error reduction. The majority of these studies apply the WRF model. Day-ahead WRF forecasts have been statistically refined using an artificial neural network (ANN) for the Brazilian Northeastern region (Lima et al., 2016), exponential smoothing (Aryaputera et al., 2015) and multivariate statistical learning for Singapore (Verbois et al., 2018), and a Kalman filter on Reunion Island (Diagne et al., 2014). Other post-processing approaches on Reunion Island are performed by Badosa et al. (2015) who apply an empirical-statistical downscaling (ESD) method to reanalysis output, and Lauret et al. (2016) who use a neural network to improve the accuracy of GCM forecasts.

The accuracy of cloud cover forecasts is limited by the predictability of clouds, the skill of the NWP model and its parameterisation schemes, and the quality of the initial conditions. In the case of LAMs, initial conditions can either be derived either by interpolating the lower resolution GCM information to the higher resolution LAM grid, or by applying data assimilation (DA) methods that statistically combine observations and background information such as previous forecasts (Kalnay, 2003).

This section shows that studies that aim at evaluating and improving the performance of NWP models in the tropics in terms of solar irradiance are rare. Moreover, although positive impacts of DA on LAM-based GHI forecasts have been observed multiple times for mid-latitudes (Lauwaet et al., 2011; Yang and Kleissl, 2016), a focus on the tropics is still missing in the literature. Therefore, in this thesis, the focus is set on DA with LAMs, rather than mere dynamical downscaling or the improvement of LAMs themselves.

1.4 Satellite data assimilation for irradiance forecasting

An area of research with great potential for improving cloud forecasts produced by NWP models is data assimilation (Geer et al., 2017). DA is used to determine the most likely state of the atmosphere at a given time, or in other words, to determine a so-called "analysis" of meteorological parameters. This analysis provides the initial conditions (ICs) for a NWP model forecast (figure 1.9). DA

requires two main ingredients to produce an analysis for the entire NWP model grid. The first ingredient are observations of the atmospheric state close to the time of the analysis. Since observations can never be provided for each grid box of the three-dimensional model grid, so-called "background information" is the second required ingredient. The "background" that fills the entire model grid is usually provided by previously performed NWP model forecasts. These forecasts are also called "first guess" forecasts. Figure 1.9 illustrates the process of data assimilation that combines first guess forecasts and observations to derive an analysis of a given weather situation. These analyses are used to produce new first guess forecasts, which leads to a cycling procedure. As indicated in the figure, both the background and the observations do not represent the truth, but they have errors. The background and observation errors are another important ingredient for data assimilation. More information about data assimilation in general can be found in Kalnay (2003).

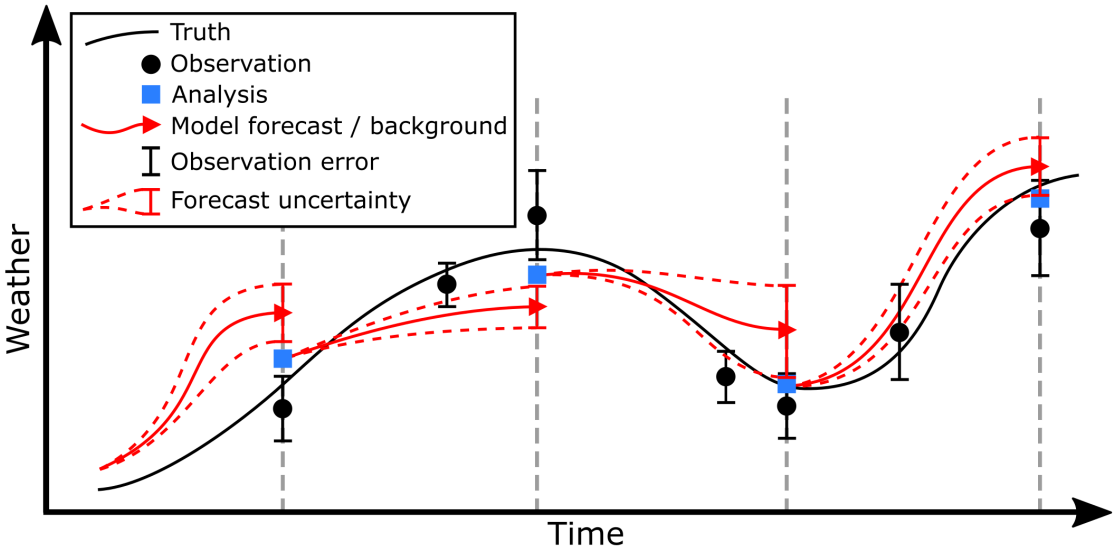

Figure 1.9 – Sketch of the course of an arbitrary weather-related variable in time, captured by observations, model forecasts and analyses. The vertical dashed grey lines show regular time intervals at which analyses (initial conditions for new forecasts) are determined.

In the past decades, a variety of DA methods and strategies, such as nudging, optimal interpolation, variational methods such as 3D-Var or 4D-Var, ensemble Kalman filters (EnKFs), and hybrid methods have been developed and successfully applied to numerous global and regional NWP models by diverse research institutions and weather offices around the world (Gustafsson et al., 2018; Lenfle, 2018).

The term "conventional observations" is used for in-situ observations of the variables used in NWP models (wind, temperature, humidity, and surface pres-

sure) (Kalnay, 2003). Such observations typically originate from sources that are available since several decades, such as synoptic stations, airports (metar), airplanes, radiosoundings, and ships. Examples of other sources of observations that rely on technologies such as remote sensing are precipitation radars, satellites, and GPS radio occultation. The density of conventional observations is low in the SWIO compared to mid-latitudes in the Northern Hemisphere (figure 1.10), which motivates the use of satellite observations. But even with a dense observation network, observations would not be available for every model grid box, therefore necessitating the use of DA methods that can spread observational information to other parts of the domain and to unobserved model variables.

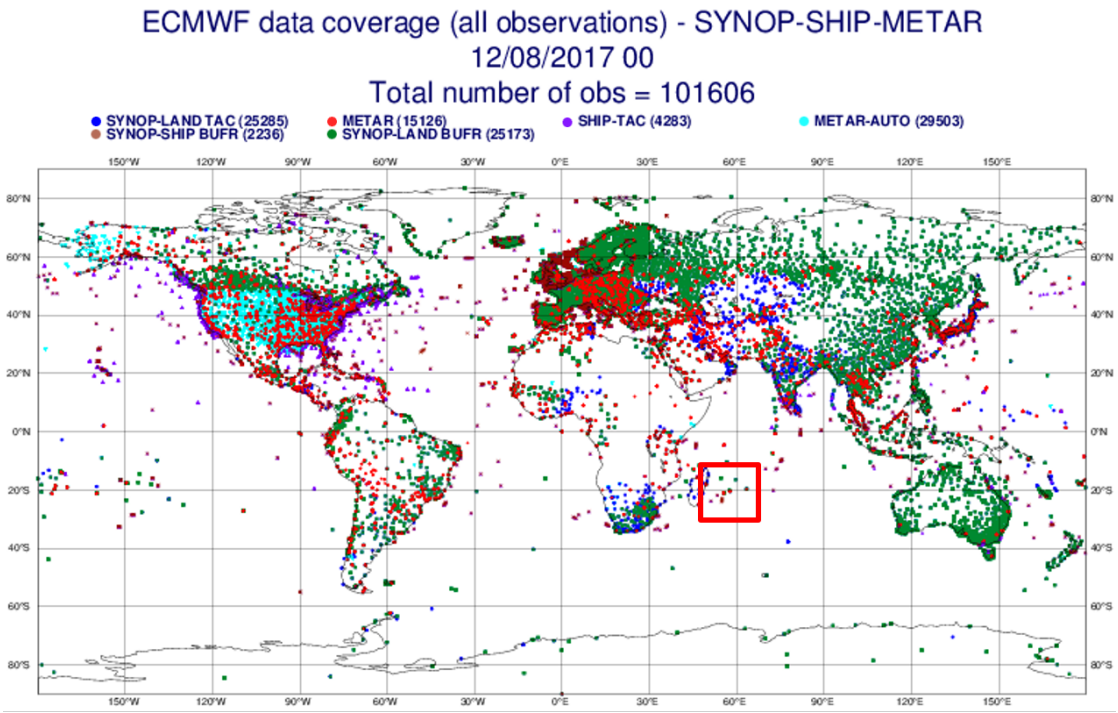

Figure 1.10 – Illustration of the spatial density of available conventional observations (here only synop, ship and metar) on 12 August 2017 at 0000 UTC. The study region in the southwestern Indian Ocean is highlighted by the red rectangle. Source: ECWMF.

Geostationary meteorological satellites provide atmospheric observations that are highly valuable for the determination of cloud analyses. This source of observation is the only one offering pertinent information about cloud presence, properties and evolution with high spatial (< 4 km) and temporal (5-15 min) resolution and global-scale coverage coverage. Thus, the assimilation of geostationary satellite observations in regional NWP models helps to better forecast cloud information at spatio-temporal resolutions that are required by the users of solar power forecasts. It is worth mentioning that the resolution of geostationary satellite observations decreases with increasing distance from the subsatellite point over the Equator. This circumstance is especially important with increasing latitude (e.g. Scandina-

vian countries) while the majority of the tropics is covered at high resolutions.

Satellites do not measure quantities like temperature or humidity, but radiances, which are radiometric signals. The on-board sensors of geostationary satellites measure radiances at different wavelengths or channels, mainly in the infrared (IR) spectrum with channel centre wavelengths of approximately 3.8-13.3 µm, in the near infrared (NIR) spectrum at 1.4-2.3 µm, and in the visible (VIS) spectrum at 0.4-0.9 µm. The IR channels are often distinguished between those that are primarily sensitive either to water vapour (WV), temperature, atmospheric trace gases (e.g. ozone) or so-called window channels. The latter are channels at which radiation is not significantly absorbed by atmospheric gases. Consequently, window channels provide useful information about cloud top properties when clouds are present and about the surface when clouds are missing from a given scene.

Example satellite images of VIS, IR and NIR channels are shown in figure 1.11. It can be seen that the visible channel offers the possibility to identify various types of clouds. Moreover, information about the land surface can be derived in the cloud-free case. Water vapour sensitive channels provide information about the water vapour distribution in different layers of the troposphere, and about the wind field. The observations of the thermal IR channel are influenced by both the tropospheric temperature and the land or sea surface. Figure 1.11 reveals that low clouds - often underestimated by NWP - can be detected more effectively using VIS than IR channels. However, cloud detection using VIS channels is limited to daytime. Combining information from different channels of geostationary meteorological satellites allows for the estimation of many physical cloud properties (also called cloud property "retrievals"), such as cloud cover, cloud type, cloud top pressure (CTP), cloud top height (CTH), cloud top temperature (CTT), liquid water path (LWP), ice water path (IWP), single-layer or double-layer cloud amount, effective cloud amount (ECA), cloud optical depth, phase and effective particle size (Derrien and Le Gléau, 2005; Minnis et al., 2008; Suzue et al., 2016).

In the case of cloudiness and solar irradiance forecasting, a precise cloud analysis has a bigger influence than non-related parameters (e.g. ozone concentration or land surface parameters). Thus, depending on the application of the regional modelling efforts, it is appropriate to focus on the assimilation of a subset of observation types that are linked with clouds and cloud formation. For the forecasting of clouds, these are most commonly satellite radiances or retrieved cloud properties. Global DA experiments have shown that the skill of weather forecasts largely depends on the accuracy of the initial conditions in cloud-covered areas (McNally, 2002). Pincus et al. (2011) performed perfect model experiments with two global models that showed that the assimilation of cloud information is especially advantageous in regions where other observations are sparse.

In radiance assimilation the NWP model variables must be converted into synthetic radiances while in retrieval assimilation the satellite-based variables are converted into model variables. Both techniques have the potential to significantly increase the cloud-related information content of an analysis and thus contribute

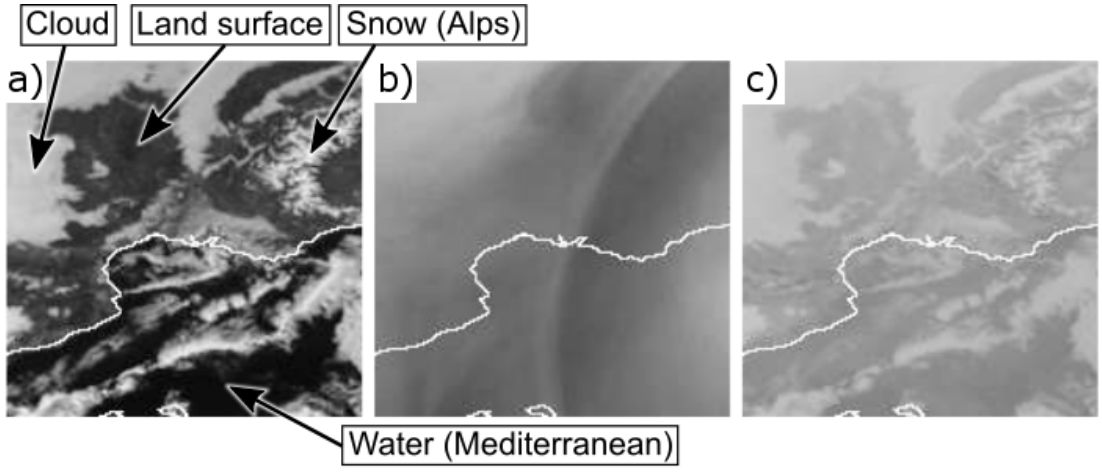

Figure 1.11 – Example images of three different channels of the SEVIRI (Spinning Enhanced Visible and InfraRed Imager) instrument onboard Meteosat-10 taken on January 1st 2017 at 1200 UTC. The images show the Mediterranean coast line of Spain and France seen by the channels VIS at 0.6 µm (a), water vapour sensitive IR at 6.2 µm (b), and thermal at IR 10.8 µm (c). Images provided by EUMETSAT.

to better short-term forecasts of cloud features. Nevertheless, the large variety of existing methods for cloud analysis determination with LAMs necessitates a thorough literature review (chapter 2).

As the influence of the LBCs becomes larger than that of the ICs in a LAM forecast with advancing forecast lead time, the third major research question to be answered is:

Research question 3 *Until what forecast lead time is the impact of satellite data assimilation on GHI forecasts noticeable?*

1.5 Scientific objectives

Besides attempting to answer the three research questions raised above, three main scientific objectives are followed in this thesis. Under the hypothesis that a literature review reveals promising strategies for satellite DA with LAMs in the tropics, the first objective of this thesis is:

Objective 1 *The identification of a promising geostationary satellite data assimilation approach for regional-scale NWP regarding clouds and solar irradiance forecasts in the tropics.*

Consequently, the application of this approach leads to the second objective:

Objective 2 *The improvement of cloud analyses in the southwestern Indian Ocean using limited-area NWP and geostationary satellite DA.*

Once this improvement is achieved, the next step is to quantify the impact on irradiance forecasts, leading to the third and last objective:

Objective 3 *The quantification of the impact of the applied DA approach on short-term (5 to 40 hours) solar irradiance forecasts on Reunion Island.*

1.6 Novelty and scope of the thesis

As this chapter shows, the topic of this thesis is placed on the interface of several comprehensive fields of atmospheric research: limited-area NWP, satellite data assimilation, and energy meteorology. In order to address the raised research questions and objectives at best, the scope of this thesis is limited as follows.

The thesis is about the quantification of the impact of geostationary satellite DA on cloud analyses and short-term GHI forecasts (5 to 40 hours) of a limited-area model in a tropical environment. Moreover, the effects of nested domains are examined, and a comparison between the performed LAM experiments and existing operational NWP model forecasts is performed.

The thesis is not about various related topics that are active fields of research. Some examples are: Improvements of parameterisation schemes; DNI or concentrated solar power (CSP) forecasting; advancement of WRF-Solar components; the relationship between GHI and large-scale oscillations like El Niño–Southern Oscillation (ENSO) or Madden-Julian Oscillation (MJO); advancements in remote sensing of clouds; ramp or variability forecasting metrics; the assimilation of observations from polar orbiting satellites.

1.7 Outline of the thesis

This thesis is structured as follows:

Chapter 2 addresses the first objective and gives a review of the use of geostationary satellite observations in regional-scale models for short-term cloud forecasting. The methodology that is used in the following chapters is based on the conclusions drawn in this chapter.

Chapter 3 explains the methodology applied in this thesis and the experiments that were conducted. Furthermore, the different data sources that are used for model initialisation, evaluation, and comparison are presented.

Chapter 4 evaluates the results of the conducted experiments regarding the impact of data assimilation on the cloud analyses. Moreover, a case study establishes the link between cloud analyses and their influence on solar irradiance forecasts.

Chapter 5 analyses the long-term impact of the applied method on forecasts of solar irradiance. Different aspects such as forecast lead time and nesting are examined, and a comparison with other NWP models is performed.

Chapter 6 summarises the thesis and provides conclusions. Some future perspectives are also given.

Supplementary material is provided in the appendix.

Parts of this thesis are identical to parts of the publications that have been accomplished in the framework of the thesis and that are listed below. Additional elements are given in the thesis.

Journal articles

Kurzrock, F., Cros, S., Chane Ming, F., Otkin, J.A., Hutt, A., Linguet, L., Lajoie, G., Potthast, R., 2018. A Review of the Use of Geostationary Satellite Observations in Regional-Scale Models for Short-term Cloud Forecasting. Meteorologische Zeitschrift.

Kurzrock, F., Nguyen, H., Sauer, J., Chane Ming, F., Cros, S., Smith, Jr., W.L., Minnis, P., Palikonda, R., Jones, T.A., Lallemand, C., Linguet, L., Lajoie, G., *submitted*. Evaluation of WRF-DART multi-phase cloud water path assimilation for short-term solar irradiance forecasting in a tropical environment. Geoscientific Model Development.

Conference communication

Kurzrock, F., Cros, S., Chane-Ming, F., Potthast, R., Linguet, L., Lajoie, G., 2016. Satellite Data Assimilation in Regional Numerical Weather Prediction as a Key for Better Cloud Cover Forecasts in Tropical Environments. Presented at the European PV Solar Energy Conference and Exhibition, Munich, Germany.

Kurzrock, F., Cros, S., Chane-Ming, F., Potthast, R., Linguet, L., Lajoie, G., 2016. Enhanced solar power forecasting in the tropics using satellite data assimilation. Presented at the International Conference on Earth Observations and Societal Impacts, Keelung, Taiwan.

Kurzrock, F., Cros, S., Chane-Ming, F., Potthast, R., Linguet, L., Sébastien, N., 2016. The use of satellite data assimilation methods in regional NWP for solar irradiance forecasting, in: Geophysical Research Abstracts. Presented at the European Geosciences Union General Assembly 2016, Vienna, Austria.

Kurzrock, F., Cros, S., Chane Ming, F., Linguet, L., Potthast, R., Lajoie, G., 2017. Meteosat-8 radiance assimilation for solar irradiance forecasting using COSMO-KENDA over Reunion Island. Presented at the EUMETSAT Meteorological Satellite Conference 2017, Rome, Italy.

Kurzrock, F., Cros, S., Chane Ming, F., Linguet, L., Potthast, R., Lajoie, G., 2017. Improving short-term irradiance forecasts in the tropics with ensemble data assimilation in limited-area models using Meteosat-8 IODC observations. Presented at the European Conference for Applied Meteorology and Climatology, Dublin, Ireland.

Kurzrock, F., Nguyen, H., Sauer, J., Cros, S., Chane Ming, F., Linguet, L., Lajoie, G., 2018. Multi-Phase Cloud Water Path Assimilation Using WRF-DART for Short-Term Solar Irradiance Forecasting in the South-West Indian Ocean. Presented at the AGU Fall Meeting 2018, Washington, DC, USA.

Kurzrock, F., Nguyen, H., Sauer, J., Cros, S., Chane Ming, F., Linguet, L., Lajoie, G., 2019. Forecasting of solar irradiance at Reunion Island using numerical weather prediction models. Presented at the EGU General Assembly, Vienna, Austria.

Chapter 2

State of the art review

Contents

Summary

Today, limited-area numerical weather prediction models (LAMs) have the potential to provide short-term forecasts of clouds at kilometre and hourly scales. However, the forecast accuracy during the first 24 hours is strongly influenced by the accuracy of the initial condition, i.e. the analyses of the atmospheric state and cloud parameters. Geostationary meteorological satellites provide valuable observations that can be used in DA for cloud analysis determination. This chapter provides an up-to-date review of the state of the art in cloud-related geostationary satellite DA with LAMs, dedicated to improve cloudiness forecast accuracy. Research and operational studies are reviewed by differentiating between satellite radiance and cloud property retrieval assimilation. The literature review gives insight into the best practices considering the large variety of LAMs, data assimilation methods, satellite sensors and channels, cloud property retrieval products and various methodological challenges. Cloud analysis methods for regional models have become more sophisticated in recent years and are increasingly able to exploit observations from geostationary satellites. Important proofs of concept have been performed in this decade, paving the way for an optimal synergy of geostationary satellite data assimilation and convection-permitting LAM forecasts. At the same time, the increasing amount of channels of geostationary satellite instruments leads to more opportunities and challenges for data assimilation methods. This chapter allows the identification of a promising DA approach that is explained in detail in the next chapter. Its application and the evaluation of its impact on solar irradiance forecasts is subject of chapters 4 and 5.

2.1 Introduction

Data assimilation constitutes a wide and complex research domain where various efforts around the globe have been made in the past decades in order to improve different specific aspects of weather forecasting (Lenfle, 2018). Bauer et al. (2011b) list recommendations for improving various aspects regarding the assimilation of satellite-based cloud observations, such as modelling, verification, data assimilation and the exploitation of observations, and call for more collaboration between the different communities. Despite recent progress in the field, the potential for cloud data assimilation in cloud resolving NWP models using geostationary sensors is far from being fully exploited (Gustafsson et al., 2018). Many issues faced with

LAMs are different than those faced with global models. One reason for this is that GCMs rely far more heavily on polar-orbiting satellite sensors that have a much lower temporal resolution than geostationary ones.

Consequently, a detailed review of geostationary satellite data assimilation in regional-scale NWP models for cloudiness forecasting is provided in this chapter. The most promising methods and their associated limitations are identified and described, paving the way for developments aimed at improving cloudiness forecasts for demanding applications such as solar energy management.

Section 2.2 introduces basic concepts of cloudiness forecasting using regional NWP and geostationary data assimilation approaches. While section 2.3 details the use of radiances as assimilated observations, section 2.4 presents the recent efforts concerning the assimilation of satellite-based cloud properties. Different comprehensive aspects of current research and operational cloud analysis systems are discussed in section 2.5. Section 2.6 provides conclusions that eventually inform the methodology that is chosen for the following chapters. Large parts of this chapter are extracted from the publication:

Kurzrock, F., Cros, S., Chane-Ming, F., Otkin, J.A., Hutt, A., Linguet, L., Lajoie, G., Potthast, R., 2018. A Review of the Use of Geostationary Satellite Observations in Regional-Scale Models for Short-term Cloud Forecasting. Meteorologische Zeitschrift.

2.2 Basic concepts

2.2.1 Data assimilation methods

This section provides an overview of basic data assimilation concepts, following the explanations that are given in training courses (ECMWF, 2016; DARC, 2016) and text books (Kalnay, 2003; Lahoz et al., 2010) on data assimilation.

The common goal of data assimilation methods is to determine an analysis $\boldsymbol{x}^a(t)$ of the atmospheric state on the NWP model grid at a given time t. The analysis serves as initial condition for the NWP model $\mathcal{M}$ which can then be applied to compute a forecast of a future atmospheric state:

$$\boldsymbol{x}^b(t+1) = \mathcal{M}(\boldsymbol{x}^a(t)) \tag{2.1}$$

The forecast $\boldsymbol{x}^b$ may be used as a so-called "background", "first guess" or "prior" information for the determination of a new analysis at the forecasted time, together with observations (figure 1.9).

Data assimilation has a long history within meteorology and it evolves continuously (Lenfle, 2018). To understand why a multitude of data assimilation methods exists today, it is helpful to consider Bayes' theorem as the basis of DA. In the context of DA, Bayes' theorem may be expressed as:

$$pdf(\boldsymbol{x}|\boldsymbol{y}) = \frac{pdf(\boldsymbol{y}|\boldsymbol{x})pdf(\boldsymbol{x})}{p(\boldsymbol{y})} \tag{2.2}$$

In this equation, $pdf(\boldsymbol{x}|\boldsymbol{y})$ is the posterior probability density function (pdf), meaning the pdf of the state variables $\boldsymbol{x}$ given the observations $\boldsymbol{y}$. The term $pdf(\boldsymbol{y}|\boldsymbol{x})$ is the pdf of the observations given a values of the state variables. The prior, or the pdf of the state variables coming from the NWP model is $pdf(\boldsymbol{x})$, while $p(\boldsymbol{y})$ is the marginal pdf of the observations. Knowing the characteristics of $pdf(\boldsymbol{x}|\boldsymbol{y})$ allows to determine the optimal analysis. However, it is virtually impossible to estimate this pdf for large dimensional systems such as an atmospheric model. Therefore, approximate solutions are required to determine the nature of $pdf(\boldsymbol{x}|\boldsymbol{y})$. The main reason why different DA methods exist today, is that such approximate solutions may be found following different approaches. A convenient and frequently made assumption in several DA methods, with the explicit exception of particle filters, is a Gaussian distribution of errors. This way, the pdf is defined by its mean and covariance. In a nutshell, variational methods aim at solving for the mode of the posterior, Kalman-based methods solve for the mean and covariance of the posterior, and particle filters find sample representations of the posterior pdf. In summary, DA methods are approximate solutions to Bayes' theorem.

In what follows in this section, a brief introduction of the basics of the methods 3D-Var, 4D-Var and the ensemble Kalman filter (EnKF) is given. These are among the most commonly applied methods in today's meteorological operation and research. It should be noted that recent particle filter developments may further improve operational data assimilation (Zhu et al., 2017).

In variational DA methods the minimisation of a cost function has to be found to maximise the posterior probability $pdf(\boldsymbol{x}|\boldsymbol{y})$, and thus to determine the analysis. The goal of the cost function is to ensure that the analysis does not derive too far from both the background and the observations. The cost function of the three-dimensional variational analysis method (abbreviated as 3D-Var) is given by:

$$J(\boldsymbol{x}^a) = \frac{1}{2}(\boldsymbol{x}^a - \boldsymbol{x}^b)^T\boldsymbol{B}^{-1}(\boldsymbol{x}^a - \boldsymbol{x}^b) + \frac{1}{2}(\boldsymbol{y}^o - \mathcal{H}(\boldsymbol{x}^a))^T\boldsymbol{R}^{-1}(\boldsymbol{y}^o - \mathcal{H}(\boldsymbol{x}^a)) \tag{2.3}$$

with $\boldsymbol{y}^o$ being the observations, $\boldsymbol{B}$ the background error covariance matrix, $\boldsymbol{R}$ the observation error covariance matrix and $\mathcal{H}$ the observation operator (or forward operator). The forward operator maps the model state to the observation space and enables the comparison of model and observations. A radiative transfer model (RTM) that converts model fields (i.e. meteorological variables) into synthetic satellite radiances is a common example of an observation operator. Analyses for given times as obtained by 3D-Var can be determined by using available observations and first guess forecasts in a cycling procedure (figure 1.9).

For a given observation, the role of $\boldsymbol{B}$ is to provide statistically consistent increments at the neighbouring grid boxes of the NWP model grid. Moreover, $\boldsymbol{B}$

ensures that the observations of one state variable (e.g. temperature) produce dynamically consistent increments in terms of the other model variables. The determination of $\boldsymbol{B}$, which is a very large matrix of approximately $10^7 x 10^7$ elements in case of a GCM (ECMWF, 2016), is not straightforward. Since the true state of the atmosphere is unknown, the errors in the background are unknown as well. Therefore, in order to estimate B, it is necessary to either make use of observation-minus-background statistics (Hollingsworth and Lönnberg, 1986), or consider the difference between multiple background forecasts that are valid for the same analysis time. These different forecasts may be forecasts originating from different analysis times such as a 24 hour and a 48 hour forecast (Parrish and Derber, 1992), or from an analysis ensemble (Fisher, 2003). An ensemble prediction system generates a multitude of forecasts using the NWP same model. The initial conditions of each ensemble member are slightly different from one another. These differences between the ensemble members increase with advancing forecast lead time since the atmosphere is a chaotic system.

The 3D-Var method considers the three spatial dimensions and aims at minimising the cost function for a given analysis time. 4D-Var also includes the temporal dimension to derive the atmospheric analysis. The evolution of the NWP model and the observations is considered during a certain timeframe before the analysis time (usually several hours). This timeframe is called the "assimilation window".

In 3D-Var, the observations, analysis, and background are valid for the same time, meaning that $\mathcal{H}$ in equation 2.3 includes only spatial, but no temporal interpolation. Since 4D-Var also includes the temporal dimension, a generalised observation operator $\mathcal{G}$ may be introduced. $\mathcal{G}$ propagates the model state $\boldsymbol{x}$, valid at a given time t_0, to the various times for which the observations are valid. Moreover, $\mathcal{G}$ spatially interpolates these propagated fields and, just like $\mathcal{H}$, converts model variables to observed quantities. It is convenient to group the different types of observations that are valid at a given time t_k into sub-vectors $\boldsymbol{y}_k$. Assuming that the observations are uncorrelated in time makes $\boldsymbol{R}$ block diagonal, with blocks $\boldsymbol{R}_k$ corresponding to the observation sub-vectors $\boldsymbol{y}_k$. The 4D-Var cost function is formally identical to the 3D-Var cost function (equation 2.3). Using the generalised observation operator $\mathcal{G}$ the 4D-Var cost function may be expressed as:

$$J(\boldsymbol{x}^a) = \frac{1}{2}(\boldsymbol{x}^a - \boldsymbol{x}^b)^T \boldsymbol{B}^{-1}(\boldsymbol{x}^a - \boldsymbol{x}^b) + \frac{1}{2}\sum_{k=1}^{K}(\boldsymbol{y}_k - \mathcal{G}_k(\boldsymbol{x}^a))^T \boldsymbol{R}_k^{-1}(\boldsymbol{y}_k - \mathcal{G}_k(\boldsymbol{x}^a)) \quad (2.4)$$

Each generalised observation operator $\mathcal{G}_k$ performs an integration of the NWP model from time t_0 to time t_k followed by a spatial interpolation and transformation from model variables to observations:

$$\mathcal{G}_k = \mathcal{H}_k \mathcal{M}_{t_0 \rightarrow t_k} \quad (2.5)$$

The gradient of the 4D-Var cost function is required in the minimization procedure. The so-called "tangent linear model" provides a computationally efficient way to calculate the model trajectory, and subsequently the cost function. The so-called "adjoint model" is used to compute the gradient of the cost function. The gradient of equation 2.4 may be expressed as:

$$\nabla J(\boldsymbol{x}^a) = \boldsymbol{B}^{-1}(\boldsymbol{x}^a - \boldsymbol{x}^b) + \sum_{k=1}^{K}(\boldsymbol{M}'^{T}(t_k, t_a)\boldsymbol{H}_k'^{T}\boldsymbol{R}_k^{-1}(\mathcal{G}_k(\boldsymbol{x}^a) - \boldsymbol{y}_k) \tag{2.6}$$

with $\boldsymbol{H}^T$ being the adjoint of the observation operator and $\boldsymbol{M}^T$ the adjoint of the forecast model. This implies that if one wants to apply 4D-Var assimilation, the adjoint code is required for each line of the NWP model code.

The 4D-Var assimilation window length has to be restricted to a few hours since 4D-Var assumes linear dynamic processes because of the need for an adjoint model and also that the NWP model is perfect. These issues limit the utility of this method for high-resolution simulations and motivate using the EnKF.

In classical variational DA, the $\boldsymbol{B}$ matrix is static and therefore does adapt to changing weather conditions or "the flow". The use of an ensemble allows for better quantification of flow-dependent covariances important for clouds, and also allows fully nonlinear forward observation operators. Ensemble forecasting provides a sample of atmospheric states which can be used to estimate the evolution of the mean state and the covariance or the model background uncertainty. Any EnKF implementation updates the prior estimate of the atmospheric state of a given ensemble member using the observations according to the equation:

$$\boldsymbol{x}^a(t) = \boldsymbol{x}^b(t) + \boldsymbol{K}(\boldsymbol{y}^o - \mathcal{H}(\boldsymbol{x}^b(t)) \tag{2.7}$$

where $\boldsymbol{K}$ is the so-called Kalman Gain that is computed as:

$$\boldsymbol{K} = \boldsymbol{P}^b\mathcal{H}^T(\mathcal{H}\boldsymbol{P}^b\mathcal{H}^T + \boldsymbol{R})^{-1} \tag{2.8}$$

Evensen (1994), who added the "Ensemble" notion to the standard Kalman filter proposed by Ghil and Malanotte-Rizzoli (1991), suggested that an ensemble can be used to approximate the covariance matrix of the background error $\boldsymbol{P}^b$, with the size of the ensemble K being much smaller than n, the dimension of the model ($K \ll n$):

$$\boldsymbol{P}_n^b \approx \frac{1}{K-1}\sum_{k=1}^{K-1}(\boldsymbol{x}_{n,k}^b - \overline{\boldsymbol{x}}_n^b)(\boldsymbol{x}_{n,k}^b - \overline{\boldsymbol{x}}_n^b)^T \tag{2.9}$$

with the overline in $\overline{\boldsymbol{x}}_n^b$ indicating the ensemble mean.

Another important concept of state-of-the-art EnKF implementations is "localisation". Since $K \ll n$ in the estimation of $\boldsymbol{P}_n^b$, sampling errors at long distances

from the location of interest are introduced when following equation 2.9. Localisation damps long distance correlations to zero by multiplying each term of the covariance with an approximation of the Gaussian function $exp(-r_{ij}^2/2L^2)$, with r_{ij} being the distance between two grid points i and j, and L the localisation scale (Hamill et al., 2001; Houtekamer and Mitchell, 2001; Gaspari and Cohn, 1999).

More detailed explanations about DA methods in general are given by Kalnay (2003) and Lahoz et al. (2010). The advantages, disadvantages and differences between variational, ensemble-based, and hybrid methods that combine aspects of variational and ensemble DA (e.g. three-dimensional ensemble–variational data assimilation (3DEnVar)) are discussed in Bannister (2017) and Kalnay et al. (2007). A detailed review of the EnKF is given by Houtekamer and Zhang (2016). The latter authors discuss, among other things, different EnKF notions such as the ensemble square root filter, the ensemble adjustment Kalman filter, and the ensemble transform Kalman filter.

2.2.2 The double penalty issue

Verifying the accuracy of cloudiness forecasts amounts to verifying forecasts of spatial fields. It is unrealistic to expect that highly resolved NWP models may produce perfect forecasts of cloud locations. A NWP model may forecast a given cloud at a slightly shifted location. In terms of standard verification measures that consider the absolute error, the small displacement error would be counted twice, firstly because the cloud is missing where there should be one, and secondly because the cloud is present where it should not be. This issue is known as the "double penalty" issue (Jolliffe and Stephenson, 2012).

It is especially of importance when forecasts at different horizontal resolutions, for example from two different models, are compared with each other. The high-resolution model might forecast a given cloud correctly sized but with a slight spatial displacement. The coarser model might forecast a rather smooth cloud cover and agree better with the observation. The double penalty issue thus applies to the higher resolved model compared to the model with coarser resolution, although the highly resolved model is able to forecast a more realistic cloud extent.

Comparing cloud cover forecasts of different models is therefore not straightforward and requires sophisticated verification methods, which is why cloud-related parameters such as irradiance or precipitation are often used for verification, since standard verification methods and metrics can be applied.

2.2.3 Cloud analysis determination

Determining an atmospheric analysis in the presence of clouds is a complex issue because clouds are captured differently by observations and NWP models. Figure 2.1 can be understood as a two-dimensional illustrative example of this issue. The goal is to build a two-dimensional cloud analysis (e) with a certain grid spac-

ing containing the simplified information whether clouds are present or not in a given grid box. In this example the "truth" (a) is a situation with four cloud systems. It is observed by a satellite (b) with a certain resolution and error. A NWP model provides a first guess of the situation (c) with the respective model grid spacing. The satellite observations are mapped to the model grid (d). In the actual DA procedure the cloud analysis (e) is determined by taking into account the first guess, the mapped observations and their respective uncertainties. In reality the situation is much more complex since the vertical and temporal dimensions and other cloud-related parameters like cloud fraction, phase, optical thickness or precipitation are also important and may be part of the cloud analysis that is to be determined.

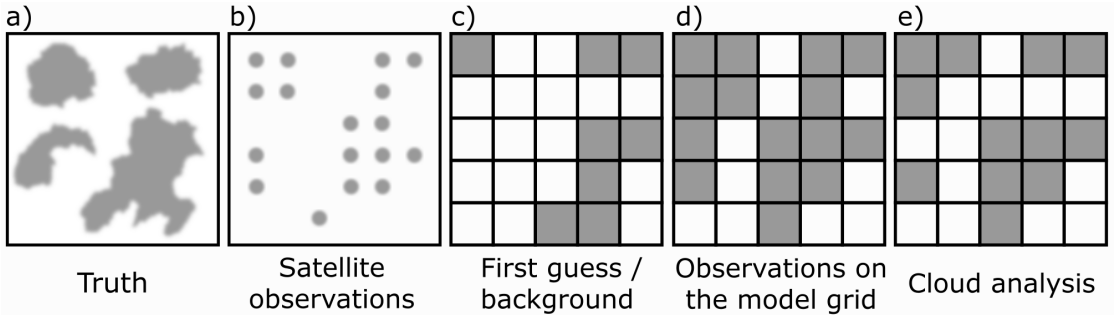

Figure 2.1 – Two-dimensional (horizontal) sketch of different representations of a partly cloudy region as seen from above. The grey areas represent cloud presence while white means no cloud. a) "True" situation of cloud presence. b) Cloud presence observation as seen by the satellite. c) Example of a first guess produced by a regional NWP model. d) Mapping of the satellite observation to the model grid. e) Cloud analysis resulting from c) and d) using data assimilation.

Depending on their spectral characteristics, the assimilation of different satellite channels involves different issues. For example, the successful assimilation of window channels requires accurate information about the land-surface emissivity, which is difficult to obtain. Because of this, such observations are typically excluded in satellite DA (Harnisch et al., 2016). Most observations obtained from geostationary satellites for a given location are significantly influenced by clouds (figure 2.2). The figure depicts that different channels (A and B) are sensitive to different levels of the atmosphere. The vertical height of their maximum sensitivity strongly depends on the presence and vertical location of clouds. While the yellow sensitivity curve in figure 2.2 serves as an example of a water vapour channel, the red and blue curve are examples of the sensitivity of a thermal IR channel in the cloud-free and cloudy case. Either information about the temperature of the lower atmosphere or of the cloud top can be derived. The sensitivity curve of a VIS channel would either peak at the surface or at the cloud top.

As mentioned previously in chapter 1, satellite observations can either be assimilated directly or converted into retrievals prior to their assimilation. Figure 2.3

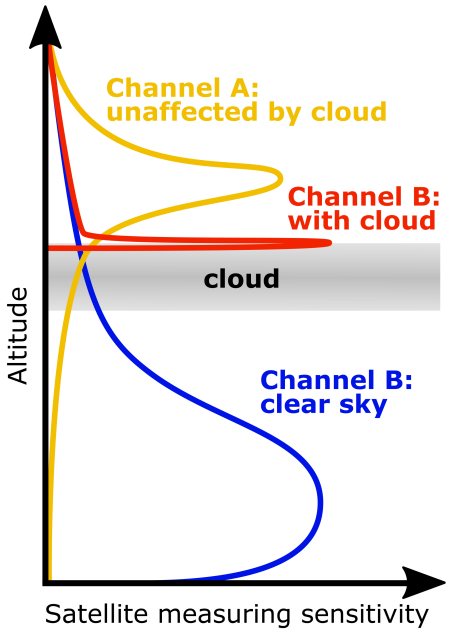

Figure 2.2 – Sketches of the sensitivity of two different satellite channels in the clear-sky and cloudy case. Yellow: channel A is generally unaffected by the cloud; Red: channel B is affected by cloud; Blue: channel B in the clear sky case.

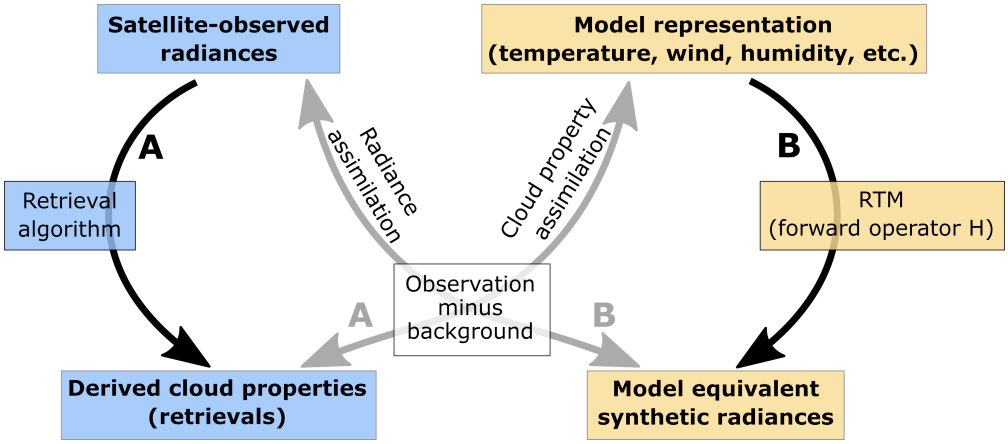

Figure 2.3 – Schematic illustration of the difference between retrieval or cloud property assimilation (path A) and radiance assimilation (path B).

illustrates these two approaches. In radiance assimilation the NWP model variables must be converted into synthetic radiances (path B) while in retrieval assimilation the satellite-based variables are converted into model variables (path A). It is important to keep in mind that uncertainty is introduced both by the retrieval algorithm (black path A) and the forward operator (black path B), meaning that retrievals and synthetic radiances are never free of erros. Both techniques have the potential to significantly increase the cloud-related information content of an

analysis and thus contribute to better short-term forecasts of cloud features.

Sections 2.3 and 2.4 provide a review of recent efforts in the two fields of radiance and cloud property assimilation. Current methods are assessed regarding their potential to improve the accuracy of limited-area short-term forecasts of cloud-related parameters like cloud extent, incoming solar irradiance at the surface, or precipitation.

2.3 The assimilation of radiances

The assimilation of satellite radiances is the most widely used method to assimilate satellite observations into NWP models. This technique is especially being performed and enhanced for operational GCMs by weather services around the world (Bauer et al., 2011b; Geer et al., 2017).

In the process of radiance assimilation, synthetic radiance observations are calculated from the model variables using a forward RTM as the observation operator ($\mathcal{H}$ in equations 2.3 and 2.7). During the data assimilation step, the difference between these synthetic and observed radiances is considered. This difference is called an "innovation". The so-called "analysis increment" is the impact on the observed and unobserved fields as a consequence of the combination of the innovation with all other assimilated observations, observation errors, background error covariance and covariance localization. This ultimately leads to the final analysis, i.e. the updated initial model state for the next model run.

The methodological advantage of radiance assimilation is that it makes direct use of the observed radiances or brightness temperatures (BT) without the need to first convert the observations into some retrieved property. Retrievals are generally more uncertain than radiances since they are no direct measurements. They often rely on assumptions and auxiliary information, possibly from NWP models. The quantification of the radiance observation error is thus more accurate (Migliorini, 2012).

For locations at which clouds are not present between the ground and the satellite sensor, the obtained radiances are often referred to as clear-sky radiances. It is prudent to distinguish between cloud-free and cloud-affected radiance assimilation. Before reviewing recent advances in cloud-affected radiance assimilation in section 2.3.2, section 2.3.1 focuses on clear-sky radiance assimilation.

2.3.1 Clear-sky radiance assimilation

While the assimilation of clear-sky radiances has already been performed for several decades in operational global models, it is still a recent topic in regional modeling. One reason for that is that the analysis is strongly influenced by the initial and lateral boundary conditions of the driving global model. Other reasons include difficulties associated with bias correction given the lack of global data and

uncertainties associated with the land surface specification. The latter aspect is more important for regional-scale models given that they are typically located over land. Furthermore, GCMs largely rely on polar-orbiting satellite sensors, which are less useful for regional-scale models given their infrequent coverage of a regional domain.

Several recent studies evaluated the impact of clear-sky radiance assimilation on cloud-related parameters, e.g. water vapour profile, cloud mask and precipitation. In the study of Zou et al. (2011) and the follow-up study of Qin et al. (2013) coastal quantitative precipitation forecasts (QPF) were improved by assimilating GOES (Geostationary Operational Environmental Satellite) clear-sky IR radiances in the WRF model using the NCEP (National Centers for Environmental Prediction) GSI (Gridpoint Statistical Interpolation) 3D-Var system (Shao et al., 2016). The assimilation of the GOES observations results in a large added value compared to solely conventional data (like synoptic stations, radiosondes, aircraft reports and wind retrievals) in the study of Zou et al. (2011) and likewise in a positive impact in addition to the assimilation of multiple polar-orbiting satellite observations in Qin et al. (2013). Zou and Da (2014) further developed the assimilation strategy and aim at a full utilisation of cloud-free radiance observations. They implemented a regime-dependent cloud mask for the removal of cloud-affected GOES radiance observations. The outcome is a more precise cloud mask determination when assessed using a MODIS (MODerate-resolution Imaging Spectroradiometer) derived cloud mask. These studies prove that even without considering cloud-affected radiances, the assimilation of radiances observed in regions without clouds prior to convective initiation has a positive impact on short-term cloud and QPF forecasts.

A positive impact of clear-sky radiance assimilation on tropospheric moisture in WRF has also been found in experiments by Singh et al. (2010, 2016) with the WRFDA (WRF model data assimilation system) 3D-Var system (Barker et al., 2012) and model domains centred over India: The first-time assimilation of clear-sky water vapour-sensitive radiances of the Indian satellite Kalpana into WRF results in improved analyses and short-term forecasts, especially for mid-upper tropospheric moisture (Singh et al., 2010). While the month-long simulations prove the benefits of this practice, extended experiments with more than one channel are desirable. Consequently, in the experiments of Singh et al. (2016) several channels of the most recent Indian satellite INSAT-3D (Indian National Satellite System) have been considered for the first time. Assimilating INSAT-3D clear-sky temperature and water vapour-sensitive radiances results in improved tropospheric moisture and temperature profiles in the analysis and improved forecasts of moisture, wind, temperature and precipitation.

As Yang et al. (2017) demonstrate by applying a 3DEnVar approach with WRFDA, hybrid methods of variational and ensemble DA methods offer a great potential to improve convection-permitting LAM forecasts of clouds. The case study results over Mexico using GOES imager clear-sky radiances show analysis improvements in terms of temperature and humidity that ultimately lead to

improved 24 h precipitation forecasts.

The results of these various studies with WRF are proof of the positive impact of clear-sky radiance assimilation on regional forecasts of cloud-related parameters. In order to avoid radiation from the surface, clear sky radiance assimilation is usually performed using channels whose sensitivity profiles peak in the middle and upper troposphere. To a large extend this explains the positive impact on temperature and humidity profiles in these altitudes, ultimately impacting clouds and precipitation. With a horizontal grid spacing of 25 and 30 km the experiments of Singh et al. (2010, 2016) were performed with rather coarse horizontal resolutions of the LAM. In contrast, Zou et al. (2011) and Qin et al. (2013) used 10 km while Yang et al. (2017) used 4 km. The impact of different domain sizes and resolutions on the assimilation outcome should be the subject of future work. Moreover, all of these studies present case studies. Exhaustive evaluations for several months have not been performed. Those would strengthen the significance of the results, especially regarding the use of new satellites like INSAT-3D. Long-term evaluations of clear-sky radiance assimilation with 4D-Var or ensemble DA systems are likewise missing in the literature. Such studies could bring forth important information about the dependency of clear-sky radiance DA on the lateral boundary conditions and different synoptic weather conditions. Nevertheless, avoiding the use of cloud-affected radiances and only assimilating clear-sky radiances is not comprehensive. While some authors focus exclusively on the impact of clear-sky radiance assimilation, most of the research community has focused on the assimilation of cloud-affected radiances aiming to improve analyses with respect to clouds.

2.3.2 Cloud-affected radiance assimilation

2.3.2.1 General issues

Since the past decade, there have been more concentrated efforts to assimilate cloud-affected radiances into global NWP models (Geer et al., 2017). Processing clear-sky and cloud-affected radiances in a uniform way in global models is currently one of the top priorities in operational satellite data assimilation. Concerning LAMs, cloud-affected radiance assimilation is also increasingly investigated. The assimilation of cloud-affected radiances is considerably more challenging in both global and limited-area models for several reasons, discussed by several authors (Vukicevic et al., 2006; Seaman et al., 2010; Polkinghorne and Vukicevic, 2011; Kostka et al., 2014). The main aspects are:

(1) The nonlinearity of moist processes is difficult to take into account.

The observation operators have to take into account water, which appears in all phases in the cloudy atmosphere, i.e. as vapour, liquid, mixed-phase or glaciated. Radiative transfer processes involving clouds and precipitation are nonlinear, which conflicts with the fact that variational DA systems require linearized and adjoint forms of the forward operators during short time windows (Otkin, 2010; Bauer

et al., 2011a,b). Otherwise the convergence of the minimization of the cost function is not guaranteed (Kostka et al., 2014). Errico et al. (2000, 2007a) show that the cost function can become multimodal when moist processes are involved and that the minimization algorithm finds local minima of the cost function but not its global minimum. Consequently, more iterations are needed which increases the computational requirements and spurious noise can be introduced in the adjoint model which then leads to numerical instability (Polkinghorne and Vukicevic, 2011).

(2) Detailed information about cloud microphysical variables and their uncertainties are required.

Clouds and precipitation are discontinuous in time and space. The associated processes and uncertainties are generally not well modelled by NWP models (Vukicevic et al., 2006; Bauer et al., 2011b). This poses problems for the forward operators that require precise profiles of cloud parameters (Weng, 2007). Bennartz and Greenwald (2011) discuss radiative transfer issues related to this circumstance. The accurate description of cloud-resolving model background errors is a highly complex problem regarding the structure of the error covariance matrix (Weng, 2007) that is usually assumed to be isotropic and homogeneous and constant during the assimilation window for variational data assimilation (Bauer et al., 2011a).

(3) Cloud location errors are difficult to handle.

Regarding clouds, four cases are possible in satellite data assimilation: (1) Both the model and satellite have clouds (2) the model has a cloud that is not observed by the satellite (3) the satellite observes a cloud while the model simulates a cloud-free atmosphere (4) or both are clear (figure 2.1 (c) and (d)). This uncertainty is referred to as model cloud misplacement or location errors (Polkinghorne and Vukicevic, 2011; Kostka et al., 2014). Location errors also cause problems in the adjoint calculation when observed clouds do not exist in the model. These aspects limit the ability of cloud-affected radiance assimilation in generating new clouds in the model (Seaman et al., 2010; Polkinghorne and Vukicevic, 2011). As in the case of the nonlinearity problem, EnKFs are more robust than variational techniques concerning cloud location errors (Otkin, 2010; Zupanski et al., 2011).

Another challenge regarding LAMs is the development of bias correction schemes, especially in the situation where both clear and cloudy sky observations are assimilated. Compared to global NWP models, bias correction is more challenging in LAMs because their small geographic extent makes it unlikely that they will capture a wide range of synoptic weather conditions. This is important because biases may be dependent on the prevailing weather and in the case of all-sky radiance assimilation will also be tied to different cloud types (Otkin et al., 2018). This issue is crucial for polar-orbiting satellite sensors because they only observe the LAM domain two times each day, but it will be less of an issue for geostationary sensors since they provide complete domain coverage, likely with temporal resolutions < 15 min. Even so, the above issues still necessitate development of innovative bias correction methods suitable for application in LAMs.

The diverse issues that radiance assimilation faces explain the fact that up to the present day a large amount of cloud- and/or rain-affected radiance observations are not considered in operational data assimilation systems (Bauer et al., 2011b; Geer et al., 2017). The complex observation operators and the strongly increasing number of channels of new-generation satellite sensors make radiance assimilation computationally costly, which is another disadvantage regarding operational NWP (Migliorini, 2012).

In the following subsections it is investigated how recent studies have approached the above-mentioned problems and their implications for future work.

2.3.2.2 Observation operators for cloud-affected radiance DA

Several publications tackle the problem of the nonlinearity of moist processes by the implementation and testing of new observation operators for cloud-affected radiances. The assimilation strategies for cloudy radiances are adapted to the relevant NWP models and their available assimilation methods, while the general goal is to overcome the problems related to cloudy radiance assimilation. Since variational and ensemble-based methods work differently regarding the handling of nonlinearity and other issues, it is important to consider the findings of the studies with respect to the applied DA method.

One early example of an observation operator for both cloud-free and cloudy situations in a LAM is the one that was developed for the 4D-Var DA system of the RAMS model RAMDAS (Regional Atmospheric Modeling Data Assimilation System). It has been developed and firstly evaluated by Greenwald et al. (2002, 2004). The multi-scattering radiative transfer model computes synthetic radiances of GOES IR and VIS channels under all weather conditions. An important finding of the adjoint sensitivity analysis is that radiances of different channels are sensitive to different types of clouds in terms of their thickness or phase. The system has been further evaluated by Vukicevic et al. (2004, 2006) in case studies of stratus and multi-layered clouds without convection where a positive impact on analyses and short-term cloud forecasts could be found in both cases. So far, the system has not been extensively evaluated for the case of complex and convective cloud situations or in other geographical regions using other satellites.

More fundamental work on cloud-affected radiance assimilation using a 4D-Var system has been done by Stengel et al. (2009, 2010, 2013). The utilised HIRLAM (High Resolution Limited Area Model) model is the first LAM that assimilated SEVIRI (Spinning Enhanced Visible and InfraRed Imager) radiances using 4D-Var (DA scheme initially described by Gustafsson et al. (2001) and Lindskog et al. (2001)). The developed observation operator uses the RTTOV (Radiative Transfer for TOVS) RTM that is maintained by EUMETSAT and a simplified moist-physics scheme that was developed at ECMWF (European Centre for Medium-Range Weather Forecasts). The application of the new observation operator results in a reduction of the analysis errors of the total integrated water

vapour and a forecast error reduction for geopotential height, humidity and wind direction at most model levels and especially in the upper troposphere. A shortcoming of the experiments is the relatively coarse grid spacing of 22 km. Further experiments should be performed in order to investigate the performance of the system at convection-permitting resolutions where the high spatial resolution of SEVIRI can be better utilised.

RAMS and HIRLAM are two prominent examples using new and functional observation operators for geostationary cloud-affected radiance assimilation for 4D-Var in LAMs in mid-latitudes. Thanks to the frequently available satellite observations 4D-Var takes into account how the atmospheric state evolves. The main achievement of the method that becomes evident in the studies is that especially tropospheric humidity increments are improved, which positively impacts cloud evolution after the model initialisation. However, the computational cost of the adjoint of the observation operator is high for a large number of observations. Moreover, using 4D-Var, the analysis and forecast quality largely depends on the capacity of the model to represent cloud processes. Especially in convective situations and at high resolutions the method reaches its limits, which is to be investigated by future studies. For example, the evaluation of tropical convective events would be an extreme performance test.

Kostka et al. (2014) criticise that not much work has been done regarding the assimilation of VIS and NIR radiances and list several advantages of VIS and NIR compared to IR radiances concerning cloud information content. They tackle this issue with the development of a new observation operator for NIR and VIS reflectances for the COSMO (COnsortium for Small-scale MOdeling) model and its LETKF (Local ensemble transform Kalman filter) DA system. The kilometre-scale ensemble data assimilation (KENDA) system for the COSMO model, developed by the German meteorological service (Deutscher Wetterdienst, DWD) constitutes an ensemble modelling system that includes the assimilation of geostationary satellite observations in a cloud-resolving model. The KENDA system is outlined by Schraff et al. (2016) while further insight is given by Harnisch et al. (2016) and Sommer and Weissmann (2014). In their simulations with the new NIR and VIS observation operator using Meteosat observations Kostka et al. (2014) obtain the best results by horizontally smoothing the observations and by applying a parallax correction, which accounts for the slant satellite viewing angle through the atmosphere. Nevertheless, the usage of VIS observations is constrained to the day-time, which limits their utility. Yet, the development of observation operators for VIS channels constitutes an important contribution to maximise the use of geostationary satellite observations.

2.3.2.3 Handling observation and model background errors

With an increasing cloud amount the observation and forward operator errors often acquire non-Gaussian error characteristics, which is not in line with the com-

mon DA assumption of normally distributed errors. Recent works using COSMO-KENDA attempt to account for this circumstance with new methods for error estimation and bias correction (Harnisch et al., 2016; Otkin et al., 2018). Harnisch et al. (2016) apply a dynamic observation error estimate depending on the cloud impact with COSMO-KENDA – a technique that has previously been applied in the assimilation of microwave observations in a GCM (Geer and Bauer, 2011) and thus been transferred to infrared radiance assimilation in a LAM. The positive result is that the first-guess departure (observation minus first-guess) statistics become closer to a normal distribution. Otkin et al. (2018) present a new bias correction approach based on a Taylor series polynomial expansion of the observation departures that is able to remove both linear and nonlinear conditional biases from all-sky satellite brightness temperatures. Passive monitoring experiments using BTs from two WV channels on SEVIRI showed that the bias in the observation departures was greatly reduced when using higher order Taylor series terms and bias predictors sensitive to clouds and water vapour. Although these studies present important proofs of concept to improve all-sky (cloud-free and cloud-affected) IR radiance assimilation with a highly-resolved LAM (2.8 km grid spacing), a long-term evaluation of the methods and an extension to more channels would be desirable.

Further studies with the RAMS model and cloud-affected GOES radiances have been performed, addressing the above-mentioned problems (2) and (3). Polkinghorne et al. (2010) compute mean model background error statistics at cloud-resolving grid spacing of 4 km in order to further improve the RAMDAS 4D-Var assimilation system. They introduce a simple cloud mask and distinguish between clear-sky observations and those with either low or high clouds. This way, cloud location errors can be reduced during the assimilation by choosing only points with the same type of cloud in both the model background and the observations. Nevertheless, the cloud type agreement between observations and model is often poor due to the imperfect representation of the modelled cloud situation. Polkinghorne and Vukicevic (2011) further evaluate the impact of the established model background error statistics in a larger domain while Seaman et al. (2010) investigate the assimilation of cloud-affected IR radiances with a cloud-free model background of RAMS at a grid spacing of 6 km. The latter investigation also addresses the cloud location error problem. In the studied case a mid-level cloud is present in the observations (figure 2.4 (c)) but not in the dry model background (figure 2.4 (a)). The difficulty for the 4D-Var system is to generate a physically consistent state between temperature, humidity, wind and clouds. The authors find that the temperature and humidity profiles are modified in the correct direction after the assimilation of GOES radiances, bringing the model closer to the generation of the observed mid-level cloud (figure 2.4 (b)). Nevertheless, the model does not necessarily assume a consistent and realistic cloud as a consequence of the assimilated radiances (figure 2.4 (d)). The study of Seaman et al. (2010) is one of the rare ones that explicitly examines the influence of the domain size on the DA results.

In the studied case, increasing the domain size changes the initial model state and the observed cloud covers a smaller proportion of the domain which does not necessarily lead to improved results. The impact of different LAM domain sizes needs to be studied with other models, at different resolutions and under various meteorological conditions.

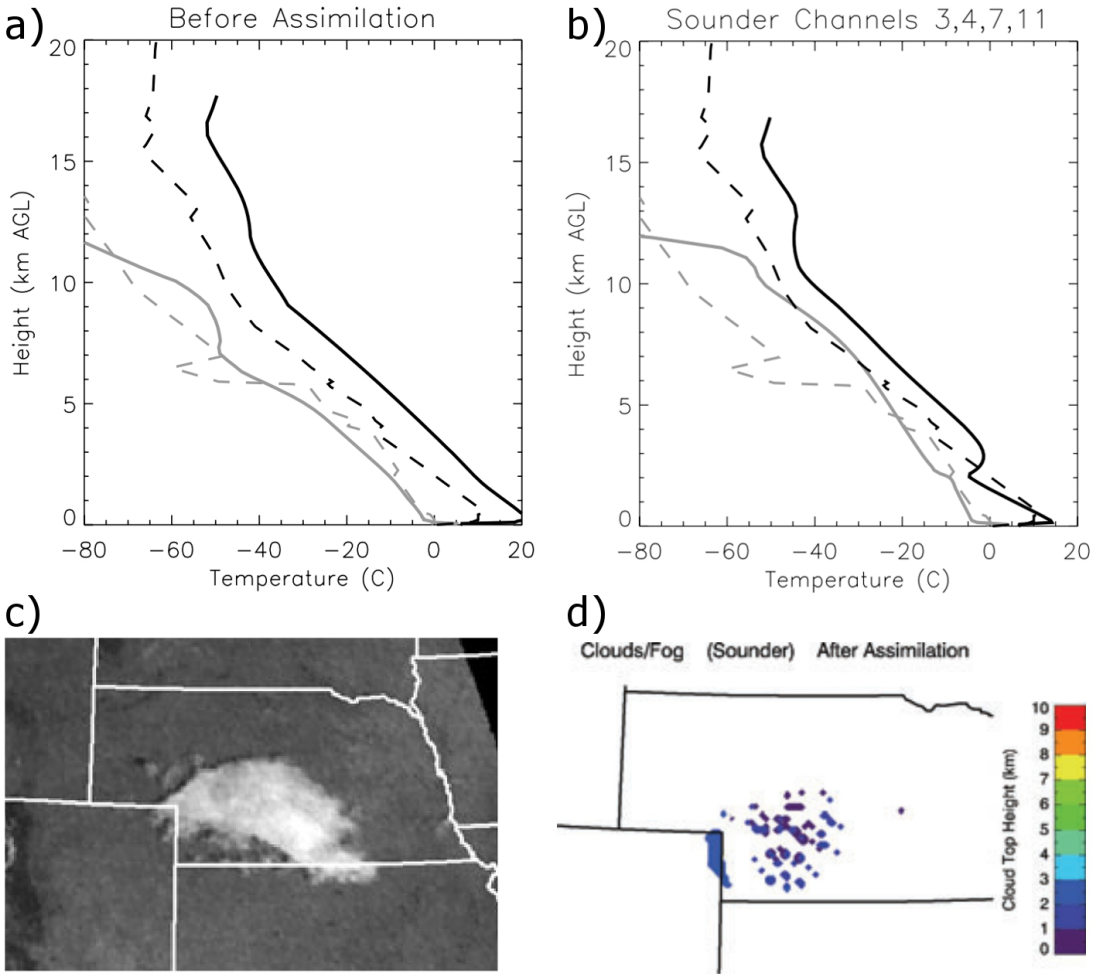

Figure 2.4 – Illustrations of RAMS 4D-Var radiance assimilation experiments over Nebraska on 2 November 2001 with a cloud-free RAMS background. a-b) Soundings of temperature (black) and dew point (grey) at North Platte, Nebraska observed at 1200 UTC (dashed lines) and simulated by RAMS at 1145 UTC (solid lines) before assimilation (a) and after assimilation of GOES Sounder channels 3, 4, 7 and 11 (b). c) GOES visible image of an altocumulus cloud extending between 4.2 and 4.7 km above mean sea level taken at 1445 UTC. d) Model location and height of cloud top in km above ground level (AGL) after assimilation of GOES Sounder channels 7 and 11 with decorrelation lengths doubled revealing the largest cloud (along the Nebraska-Colorado border) from any experiment that may be considered 'mid-level' with a top height of 2.5 km AGL. Original figures adapted from Seaman et al. (2010).

Adaptive error inflation methods for observation errors (Minamide and Zhang, 2017) and background errors (Minamide and Zhang, 2019) for all-sky radiance DA with an EnKF have recently been developed and evaluated with WRF. The adaptive observation error inflation (AOEI) inflates the radiance observation error if the increment is large and keeps a minimum error of 3 K when the increment is small. Adaptive background error inflation (ABEI) aims at a better initiation of clouds by defining inflation factors that are proportional to the difference between observed and simulated BTs in the case of a cloud-free model background with cloudy observations. The authors of these inflation methods suggest that a combination with other adaptive inflation techniques might further improve the outcome.

The different RAMS case study experiments (Polkinghorne et al., 2010; Polkinghorne and Vukicevic, 2011; Seaman et al., 2010) show a high sensitivity of the 4D-Var DA system to diverse parameters like assimilation window length, allowed difference of observed and modelled BT, background error decorrelation length, domain size and the studied case. These are important findings that stress the difficulty of correctly configuring a 4D-Var cloud-affected radiance DA scheme for a cloud-resolving LAM. The works are a step forward in solving the cloud location error problem, but do not completely solve or circumvent it. The generation of model clouds with 4D-Var radiance assimilation in case of a cloud-free background is a major issue for which no comprehensive solution exists today.

2.3.2.4 The assimilation of new generation geostationary satellite observations

On the side of EnKF systems, besides the above-cited works with the COSMO model, several observing system simulation experiments (OSSE) have been performed with the WRF model and the DART (Data Assimilation Research Testbed) (Anderson et al., 2009) system (Otkin, 2010, 2012a,b; Jones et al., 2013a, 2014; Cintineo et al., 2016; Jones et al., 2017). While Jones et al. (2017) evaluate the potential impact of geostationary hyperspectral observations, the other studies have in common that they aim at evaluating the impact of assimilating simulated GOES-R radiance observations at cloud-resolving resolutions. Otkin (2010) showed that the assimilation of both clear-sky and cloud-affected synthetic GOES-R ABI (Advanced Baseline Imager) IR brightness temperatures improved cloud analyses for a convective case across the central U.S. Otkin (2012a) subsequently showed that the analysis and forecast accuracy are noticeably impacted by the choice of the covariance localization radius. Following these studies, the impact of WV-sensitive IR brightness temperatures was firstly evaluated by Otkin (2012a) resulting in improved cloud and moisture analyses for a cool season weather event. Cintineo et al. (2016) and Jones et al. (2013a, 2014) assimilate both synthetic GOES-R BT and radar observations, showing that the two complement each other and that the satellite observations are vital. Distinct improvements of analysis and forecast

accuracy and the simulated cloud field can be found throughout the experiments thanks to the assimilated synthetic satellite observations. The works constitute an important preparation for the usage of real GOES-R ABI observations with state-of-the-art cloud-resolving ensemble DA modelling systems.

The first real-world case study of all-sky GOES-16 ABI radiance assimilation is presented by Zhang et al. (2018). They present a case study including highly-resolved (1 km grid spacing) WRF simulations of a tornatic thunderstorm event in the US using the Pennsylvania State University (PSU) WRF-EnKF cycling data assimilation system (Zhang et al., 2009; Weng and Zhang, 2016), and the AOEI and ABEI techniques. The results indicate that the assimilation can help to better forecast such events and improve operational warning processes for severe weather. Since GOES-R is now operational as the GOES-16 and GOES-17 satellites, more evaluations of real cases using more of the available channels on these satellites are expected to be performed.

Efforts to assimilate Himawari-8 all-sky radiance observations with an EnKF at cloud-resolving resolutions are also being made (Okamoto, 2017; Honda et al., 2018b,a; Minamide and Zhang, 2018; Sawada et al., 2019). Okamoto (2017) performed the first evaluation of simulated Himawari-8 all-sky IR radiances from four channels with the JMA (Japan Meteorological Agency) non-hydrostatic model (JMA-NHM). This study is one of the few ones on radiance assimilation that compares the performance of the two most widely used observation operators RTTOV and Community Radiative Transfer Model (CRTM, Han et al. (2006)). A slightly better performance is found for the CRTM. However, this finding is to be confirmed in more extensive experiments and with other models and DA systems. The authors suggest to continue with the assimilation of only WV-sensitive channels for further developments, which is the case in the work of Sawada et al. (2019) who present a case study with focus on very frequent (every 10 minutes) assimilation of two moisture-sensitive channels. The studies of Minamide and Zhang (2018), Honda et al. (2018b) and Honda et al. (2018a) find positive impacts of all-sky radiance assimilation on the prediction of a Tropical Cyclone and associated heavy rainfall. It is emphasised in these studies that the successful assimilation of cloud-affected IR radiances requires improvements of both the NWP model and the RTM. The diverse problems (1-3, section 2.3.2.1) and especially the difficult case of a cloud-free model background with cloudy observations are thus left unsolved once more.

2.3.2.5 Alternative methods

Alternative assimilation methods to 3D-Var, 4D-Var or EnKF have been tested by Raymond et al. (2004) and Zupanski et al. (2011). The former study assimilated GOES brightness temperatures from a channel sensitive to upper-tropospheric water vapour by iteratively modifying the upper-tropospheric humidity in the CRAS (CIMSS (Cooperative Institute for Meteorological Satellite Studies) Regional As-

similation System) model at 40 km grid spacing. Zupanski et al. (2011) perform a WRF case study with a grid spacing of 15 km of an extratropical cyclone over Europe with a maximum likelihood ensemble filter (MLEF) and the assimilation of synthetic all-sky IR GOES-R radiances of a window channel. It is an ambitious case study because of strong cloud location errors. Both studies are successful proofs of concept showing positive impacts of the assimilation on cloud-related parameters like upper-tropospheric moisture (Raymond et al., 2004) and cloud ice (Zupanski et al., 2011). Extended studies of the methodologies at cloud-resolving scales, over a longer evaluation period, with more channels and real observations from GOES-R or SEVIRI or synthetic observations of Meteosat Third Generation (MTG) would strengthen the proofs of concept.

2.3.2.6 Concluding remarks

In summary, radiance assimilation is the common approach for satellite data assimilation adapting the NWP model's representation of the atmosphere to the satellite's view of the atmosphere. All-sky IR radiance assimilation holds a lot of promise but has not traditionally been performed with LAMs because of the many challenges associated with it. Diverse problems occurring in cloudy situations are difficult to handle and solutions for these problems are being developed and tested. Meanwhile, radiance assimilation proves to be very beneficial for cloudiness forecasting, even if cloud-affected observations are not considered. Some important proofs of concept have been performed that still have to be supported by long-term evaluations. In particular, the topic of cloud-affected radiance assimilation in LAMs at cloud-resolving resolutions has received limited attention so far. Since 4D-Var systems struggle with accurate estimates of the model background error and the capacity of the models to simulate clouds, convection-permitting simulations with these systems are challenging and require a thorough adjustment of the modelling and DA system. Especially in the case of a cloud-free model background when clouds have to be entirely generated, the 4D-Var approach reaches its limits as a result of the unknown formulation of a balanced B-matrix for cloud parameters. This is less critical for EnKFs which would draw more attention to members already containing clouds. EnKFs are thus more robust and allow to focus more directly on the assimilation of cloud-affected radiances in combination with the general improvement of LAMs and forward operators. So far, no peer-reviewed article could be identified that evaluates hybrid (meaning both variational and ensemble-based) DA methods for all-sky radiance assimilation with LAMs.

2.4 The assimilation of physical cloud properties

Observed radiances of geostationary meteorological satellites are routinely converted into various meteorological quantities, such as physical cloud properties. This section focuses on the assimilation of cloud property retrievals since they are

expected to have the largest impact on cloudiness forecasts. The goal of cloud property assimilation is to convert the satellite observations into vertical distributions of cloud water and ice for each model column (Yucel et al., 2002).

Cloud property assimilation can be advantageous compared to radiance assimilation. This is because most satellite-derived cloud properties can be directly compared to the properties derived by NWP models. This avoids the computationally costly and complex application of RTMs in the data assimilation procedures (Jones et al., 2013b) and makes the assimilation process more independent of a given satellite.

2.4.1 Historical overview

In the last two decades, various approaches aimed at deriving atmospheric analyses for limited-area models with more realistic cloud presence estimations, using geostationary satellite observations. The first works on this subject appeared in the 1990s, e.g. with the works of (Lipton and Vonder Haar, 1990a,b). They compared several analysis methods using retrievals of atmospheric temperature and water vapour mixing ratio profiles and surface temperatures, retrieved by the VISSR (Visible and Infrared Spin Scan Radiometer) Atmospheric Sounder (VAS) on GOES and assimilated the observations using a model first-guess of the RAMS model. The applicability of the method was proven in a two-dimensional simulation of a vertical cross section in a mountainous region (Lipton and Vonder Haar, 1990a) and a summertime case study (Lipton and Vonder Haar, 1990b).

Afterwards, studies using cloud shading retrievals were performed. Lipton (1993) and McNider et al. (1995) made use of GOES visible observations in cloud shading assimilation experiments where they analysed the impacts of the modified surface temperature due to cloud shading on the planetary boundary layer and cloud development. The method of McNider et al. (1995) was later used by several other authors for land surface and air quality related experiments.

Also in the 1990s, Macpherson et al. (1996) applied the DA system MOPS (Moisture Observation Preprocessing System) and the UKMO (UK Met Office) mesoscale model, testing the assimilation of Meteosat IR imagery together with other sources of observations. The observations were used to generate a three-dimensional analysis of cloud fraction that has been converted into synthetic humidity profiles that are assimilated the same way as radiosondes. The concept of generating a three-dimensional cloud analysis from several observation sources had also been applied operationally with the limited-area model NAE (North Atlantic/European) using a 4D-Var DA system (Taylor et al., 2008; Renshaw and Francis, 2011).

Another often-cited cloud analysis scheme that makes use of several sources of observations is the ARPS (Advanced Regional Prediction System) Data Analysis System (ADAS). Souto et al. (2003) present a historical overview of the development of ADAS, whose cloud initialization procedure is an advanced version of

NOAA's LAPS (Local Analysis and Prediction System) system (described by Albers et al. (1996)). Numerous physical cloud properties are implemented in the analysis package, which enables the determination of a three-dimensional cloud and precipitation analysis.

2.4.2 Modern methods

The historical overview shows that many early studies on cloud property assimilation are still relevant since the concepts are often transferred to new models. Common conceptions and difficulties of state-of-the-art methods are examined in the following, and particularly important works are highlighted.

2.4.2.1 Handling the four possible clear-cloudy cases

As mentioned earlier, four cases can be distinguished in all-sky DA, depending on whether cloud presence is satellite-observed (yes/no) and model-simulated (yes/no). Several recent studies considered these four cases and designed the cloud analysis scheme in a way that it can handle each case. Evidently, the case in which clouds are observed by the satellite but not simulated by the model is the most difficult one since the complete three-dimensional cloud characterisation has to be created in the model. Generally, cloud property assimilation offers more possibilities to improve the cloud analysis than radiance assimilation, since it allows a more direct and distinct modification of modelled cloud fields.

Yucel et al. (2002) developed an innovative cloud analysis scheme for the RAMS model that handles the four cases. The scheme makes use of GOES VIS imager derived estimates of the vertically integrated cloud water/ice. The critical case in which clouds are not simulated by the model but observed by the satellite is solved by incrementally increasing the whole-column mass of cloud water until it equals the satellite observation. Positive impacts of this cloud injection procedure on short-term forecasts of downward surface shortwave and longwave radiation and cloud cover are found. A major disadvantage of the method is that it is based on VIS observations and thus not suitable for night-time simulations. Yucel et al. (2003) accounted for this by including IR derived cloud-top BT and height observations in the cloud injection algorithm. The improved method was tested in a case study with the fifth-generation Pennsylvania State University–National Center for Atmospheric Research (PSU–NCAR) Mesoscale Model (MM5) at 4 km grid spacing. A positive impact on short-term forecasts of downward surface solar irradiance and precipitation can be found. The biggest problem is that this positive impact rapidly decreases with increasing forecast lead time due to the mismatch between the updated model cloud cover and the unchanged vertical wind speed field. The problem of finding a consistent atmospheric state in the cloud analysis scheme has been tackled in some studies which are mentioned in the next subsection.

2.4.2.2 Assimilating cloud-top information

As in the works of Yucel et al. (2002, 2003), in many recently developed cloud property assimilation methods that have been applied to diverse LAMs the focus is mostly set on the assimilation of cloud-top information, e.g. cloud top temperature or pressure/height (Guidard et al., 2006; Taylor et al., 2008; Renshaw and Francis, 2011; Mathiesen et al., 2013; van der Veen, 2013; de Haan and van der Veen, 2014; Schomburg et al., 2014; White et al., 2018), since optical and thermal sensors are not able to directly capture information inside clouds. As satellite-derived cloud properties may have large errors, all methods have in common that the vertical position, extent, and number of cloud layers may not represent the truth. Some authors make use of other sources of observations (e.g. cloud base height or radiosondes) to better account for this limitation. Using additional observations is obvious in regions where several types of observations and a dense ground-based observation network are available. Nevertheless, this means that the respective methods are not globally applicable. In regions where geostationary satellites are the only considerable source of observations, more sophisticated methods to derive the vertical properties of clouds are needed.

One technique for the determination of the cloud-top height of the modelled clouds has been applied by several authors: In the DA methods of Yucel et al. (2003), Guidard et al. (2006), Mathiesen et al. (2013) and van der Veen (2013) the CTH is defined by the model layer whose temperature equals the satellite-derived CTT. This is a suitable approach since satellite-derived cloud-top information are rather accurate in the presence of optically-thick clouds and no additional information than the satellite observation is necessary. The shortcoming of this method is that it implies that the simulated vertical temperature profile is correct, which is not necessarily the case. Schomburg et al. (2014) use a different approach to determine the model cloud top and find a compromise between observation and model. In their approach the layer that is at the same time close to the observation and close to saturation is found by minimising a cost function. Since ensemble DA is used in their study, the ensemble members that are closer to the observation get a higher weight. Further approaches are imaginable to optimize the CTH assignment in the cloud analysis. For example, future methods might consider uncertainty information about CTH provided by an ensemble, considering all ensemble members.

2.4.2.3 The modification of vertical profiles

A common technique to initialise clouds is the direct modification of modelled profiles and fields according to the observed retrievals, e.g. profiles of humidity or water vapour, temperature and/or liquid/ice water content (Yucel et al., 2002; Mathiesen et al., 2013; van der Veen, 2013). The technique is risky since it might introduce numerical instability. That is because the entirety of atmospheric fields is not coherent anymore after the cloud analysis - A problem which can be reduced

by horizontal and vertical smoothing (Mathiesen et al., 2013) or digital filtering (van der Veen, 2013). This circumstance shows that cloud property assimilation is more experimental than radiance assimilation. Most cloud property assimilation methods focus on vertical columns at the analysis time rather than including the temporal and three-dimensional evolution of cloud properties. This is another major general point of criticism that should be approached with greater detail by future methods. Some methods which are oriented towards that direction are discussed in section 2.4.2.7.

2.4.2.4 Impacts on the wind field analysis

As mentioned before, a major conceptual difficulty of cloud property assimilation is that the focus is often exclusively set on cloud-related atmospheric parameters like humidity, without changing the initial three-dimensional wind field of the model (Yucel et al., 2002; Guidard et al., 2006; Taylor et al., 2008; Lauwaet et al., 2011; Mathiesen et al., 2013; van der Veen, 2013). Hence, the cloud analysis might be more accurate after the assimilation but the short-term forecast does not necessarily improve due to the unsuitable wind field. It can be assumed that this problem becomes more important with increasing horizontal resolution and at cloud-resolving scales. This circumstance has not yet been analysed in peer-reviewed literature. Introducing a cloud into the analysis where there was none before might subsequently change the dynamic fields (e.g. the wind field). Therefore, Chen et al. (2015) suggest to analyse the interactions between cloud microphysics and the model dynamics in order to further enhance cloud analysis schemes. A nudging approach which tackles the problem entirely from the dynamical point of view has been tested by White et al. (2018). In their method that has been applied to WRF, CTT and cloud albedo observations are used to modify the vertical velocity and divergence fields of the WRF analysis. The changes of vertical velocity have a direct impact on convection and thus the generation and dissipation of clouds. Nevertheless, since a purely dynamic approach is used, this method is not capable of considering the vertical cloud structure and cloud type or multi-layered clouds. Future cloud analysis methods based on cloud products should take account of the dynamical response of an "injected" cloud analysis.

Wind field adjustments could be provided from a different observing system such as radar, atmospheric motion vectors (AMVs) or cloud motion vectors (CMVs). A review of the assimilation of these properties is beyond the scope of this thesis. Nevertheless, the literature review does not show evidence that geostationary-observed AMVs or CMVs have yet been used within geostationary-observed cloud property assimilation schemes for LAMs. This is a potential future field of research.

2.4.2.5 Multi-layered cloud analyses and the use of multiple cloud properties

Cloud property assimilation methods generally manage to place clouds at the correct locations, according to the satellite observations, but not necessarily their true characteristics and vertical properties. For example, many methods do not favour the development of multi-layered clouds in the NWP model (Guidard et al., 2006; Taylor et al., 2008; Mathiesen et al., 2013; van der Veen, 2013; Kumar and Varma, 2016). The method presented by Bayler et al. (2000) is innovative since it allows multi-layered clouds in the cloud analysis, which is not the case for many later works. In the case that a low cloud exists in the model and the observed cloud top is considerably higher, the original cloud is left unchanged and an additional higher cloud layer is added. Besides GOES-derived CTP the method based on a successive corrections algorithm also uses an ECA product. The shortcoming of their algorithm is that it does not take into account the cloud type but only cloud presence. The principle of the method might be revived and improved by making use of multi-layered cloud products.

Integrating multi-layered cloud products to determine a cloud analysis is one potential strength of cloud property assimilation. One example of such a product derived from multiple geostationary satellites is the suite of cloud properties generated by NASA Langley's Satellite ClOud and Radiation Property retrieval System (NASA) (SatCORPS, Minnis et al. (2016)). This data set was formerly known as Global Geostationary Gridded Cloud (G3C) product (Minnis et al., 2008). Chen et al. (2015, 2016), whose method is discussed in section 2.4.2.7, are the only ones who made use of this product in a LAM so far. However, they did not make use of multi-layer information. A sophisticated use of multi-layer cloud properties could open new opportunities for cloud property assimilation and should be considered in future methods.

Multi-layered clouds are explicitly excluded in a cloud analysis method for WRF named Cloud Data Assimilation (CLDDA) (Mathiesen et al., 2013). The method that aims at improving solar irradiance forecasts focuses on coastal stratocumulus clouds in California which are expected to have a rather stable thickness. It makes use of GOES-derived CTT and determines the cloud-base height using an empirical calculation. WRF-CLDDA has been further tested by Yang and Kleissl (2016) who applied CLDDA in combination with a preprocessing scheme that uses additional NWP input. WRF-CLDDA significantly improves short-term solar irradiance forecasts in California in cases with a strong influence of stratocumulus clouds in both studies. Schipper and Mathiesen (2015) adapted the cloud analysis scheme to the Meteosat-based MPEF's (Meteorological Products Extraction Facility) Optimal Cloud Analysis (OCA) product. They attest its positive impact on solar power forecasts in a comparably long evaluation time of eight months. In summary, CLDDA is a simple and easily adaptable cloud analysis scheme which might be further improved for multi-layer clouds and different cloud types and

tested with cloud products of other satellites, in different geographical regions.

An innovative system that makes use of radiances from multiple polar-orbiting and geostationary satellites to detect multi-layer clouds and retrieve their vertical extent is the Multivariate Minimum Residual (MMR) scheme (Auligné, 2014a,b; Descombes et al., 2014; Xu et al., 2015). The scheme derives the cloud fraction for each vertical model level using observed and model-derived radiances. It has been successfully applied to the global model of ECMWF (the Integrated Forecasting System (IFS)) and to WRF. The good performance of the system can especially be achieved thanks to the intensive use of polar-orbiting satellite observations with many channels. A comparison with the other methods and studies discussed in this chapter which focus only on geostationary satellite observations, is therefore inappropriate here. Nevertheless, the ability of the system to derive a multi-layer cloud analysis is remarkable and the method will likely influence future developments in the field of cloud analysis determination, particularly concerning new geostationary satellites with more channels.

2.4.2.6 The use of multiple cloud products

Most recently developed cloud property assimilation methods use a relatively small selection of retrieved cloud properties, but not the majority of available properties at the same time to create an as complete cloud analysis as possible. The method of Lauwaet et al. (2011) for example is one of the rare methods that make use of cloud optical thickness, but no additional cloud properties. The focus on a specific choice of properties is due to the fact that the chosen ones have to be compatible with the model variables and the capabilities of the DA system. For example, Jones et al. (2013b) describe that assimilating both GOES cloud water path and cloud ice path is challenging for deep, multiphase clouds due to the detailed distinction of the cloud phase in the LAM and the binary distinction between liquid or ice of the satellite. Other factors like uncertainty treatment, quality control and computational efficiency also influence the choice of cloud properties to be used in the assimilation method (Errico et al., 2007a).

Besides, for certain regions of the earth, the cloud products of multiple geostationary satellites over the same region might be used. Over the Indian Ocean and India for example, three geostationary satellites (INSAT-3D, Meteosat-8 and Kalpana) could currently be used in order to derive a comprehensive cloud analysis.

2.4.2.7 Variational and EnKF methods

Many of the previously mentioned publications more or less forcefully inject or remove clouds in the LAM analysis for deterministic forecasts and thus constitute computationally fast alternatives to variational or EnKF methods. Besides these developments, a few authors focus on the development of observation operators for variational or EnKF DA systems that make use of retrieved cloud properties.

One example for cloud property assimilation with an EnKF system at the convective scale (2.8 km grid spacing) is the work of Schomburg et al. (2014) who present a new method to assimilate SEVIRI-derived cloud mask, cloud classification and CTH information. The actual variables that are assimilated to the COSMO ensemble are derived pseudo observations of CTH and relative humidity. Tested for single-observation experiments, the method leads to improved profiles of cloud-related variables. Non-assimilated variables (e.g. temperature and wind) are modified through cross-correlations of the background ensemble. Besides the ideas in the previous sub-sections to further improve the methodology, an extension of the method to assimilate more than cloud-top information, e.g. multi-layer cloud properties, might be done in the future. Moreover, the method might be put to the test for convective summertime cases and the impact of the assimilation on the wind field might be analysed.

Jones et al. (2013b) are the first to assimilate cloud water path (CWP) at convection-permitting resolution (3 km grid spacing). CWP is the column integrated amount of cloud water in the form of liquid or ice that is bound between a cloud base pressure (CBP) and a cloud top pressure (CTP). A forward operator for the assimilation of CWP with an EnKF (WRF-DART) is evaluated in this work. The forward operator integrates the model mixing ratios of water, ice, graupel, rain and snow following the definition of Otkin (2010) to convert the column values of CWP into vertical distributions of water. At the same time the study focuses on cloud property assimilation with a LAM using an EnKF.

The application of the new forward operator in a case with pronounced convection over the continental US shows an improved analysis of shortwave downward solar irradiance. Figure 2.5 illustrates the impact that this kind of cloud property assimilation can have on the analysis. The CWP difference plots of conventional observation assimilation (CONV) and conventional plus CWP assimilation (PATH) reveal the ability of the method to both remove and create clouds in the LAM and thus correct for cloud location and extent. While variational radiance DA without the use of an ensemble has difficulty to produce entirely new model clouds (figure 2.4, Seaman et al. (2010)), the assimilation of CWP with an EnKF proves to introduce new clouds effectively. Nevertheless, a thorough comparison of the two methods would require their application to the same weather situation. This would allow to examine the limits and differences between purely variational and purely ensemble-based DA as well as pure radiance and pure cloud property assimilation. After the successful proof of concept and a follow-up case study by Jones et al. (2015) that includes radar DA in addition to the CWP DA. An evaluation over a longer period and under various conditions is needed to strengthen the verification results for this method.

CWP has also been assimilated by Chen et al. (2015, 2016) who are the first to do this with a 3D-Var system in a LAM. Their forward operator for cloud ice water path and cloud liquid water path for WRFDA has been tested over a 10 day period with a model grid spacing of 12 km (Chen et al., 2015). Positive impacts

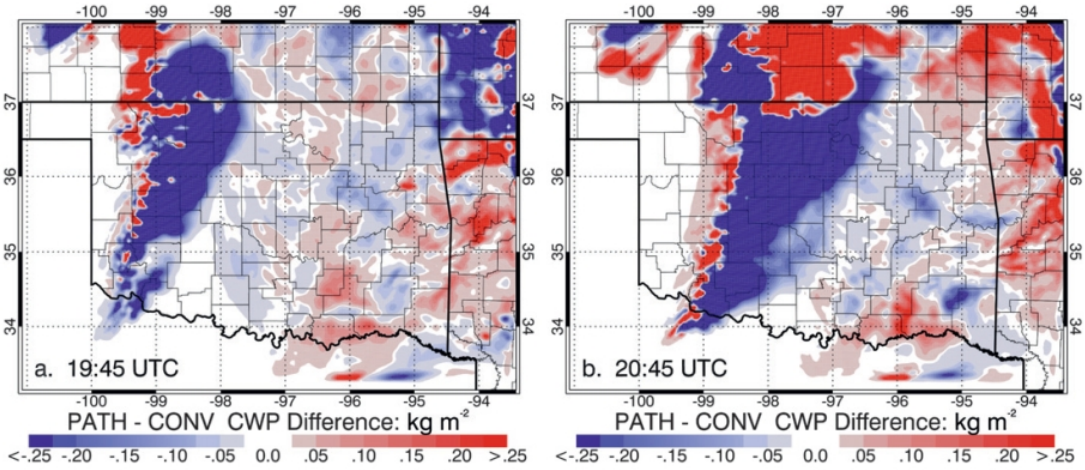

Figure 2.5 – Difference in WRF 40 member ensemble mean CWP over Oklahoma and neighbouring states after assimilation of conventional observations (CONV) and GOES CWP observations in addition to the same conventional observations (PATH) at 1945 UTC (a) and 2045 UTC (b) on 10 May 2010. Blue regions indicate where PATH generates lower values of CWP than CONV whereas red regions indicate that PATH generates higher CWP values. Original figure reprinted from Jones et al. (2013b). © American Meteorological Society.

on diverse variables, especially in the lower stratosphere are found. A subsequent study investigated the performance of the method in combination with different microphysics schemes with a 12 km / 4 km two-way nest setup (Chen et al., 2016). The authors stress that in order to further improve cloud property assimilation with a 3D-Var system, the background error covariance for hydrometeors should be anisotropic, inhomogeneous and flow-dependent. This could be achieved with a hybrid DA method using background information provided by an ensemble. The experiments of Jones et al. (2013b, 2015) and Chen et al. (2015, 2016) for CWP assimilation might be extended to the use of multi-layer cloud information. Besides, the authors list several ideas to further improve the forward operators. Future methods might take up these examples and try to make better use of multiple derived cloud properties and newly available cloud properties (for example from GOES-R, Himawari-8 and MTG) to more accurately map the observed cloud situation into the LAM.

An innovative work that performs rainfall retrieval assimilation with a 4D-Var system (WRFDA) is presented by Kumar and Varma (2016). They also appear to be the first to assimilate a geostationary satellite-based rainfall product (INSAT-3D Hydro-Estimator rainfall) with a LAM. Assimilating rainfall with 4D-Var is problematic since precipitation rate errors are not normally distributed. The advantage is that there is no need to develop a new sophisticated observation operator for the satellite product as modern 4D-Var systems are already able to assimilate

conventional rainfall observations. The method has been tested for a summer monsoon case study and proves to improve short-term rainfall forecasts. The authors suggest that an improved model background would lead to better results. One reason for this, among others, is that less observations would be rejected in quality control when the difference to the first guess is too large. An idea that has not been exploited so far is to make use of the high temporal availability of cloud property observations in 4D-Var over the duration of the assimilation window. The works of Kumar and Varma (2016) and Chen et al. (2015, 2016) can be considered fundamental for the achievement of this goal. Future studies can build upon this work and aim at making a more sophisticated use of modern cloud products in 4D-Var DA.

2.4.2.8 Concluding remarks

In summary, there is a huge variety of cloud property assimilation methods that all have their specific strengths and deficits. Two general strategies can be distinguished. The first one is "forced" cloud injection mostly via the modification of cloud-related variables in vertical columns. The second one relies on computationally much more expensive variational or ensemble-based methods and is technically closer to radiance assimilation. This variety, together with the fact that the method always has to be tailored to the applied model, makes it practically impossible to determine the most effective method solely by reviewing the literature. Comparisons of different models and methods under identical conditions would be necessary to measure the individual impact of the methods. This, in turn, would require standardised evaluation procedures for cloud property assimilation methods that do not exist today.

2.5 Discussion

After the critical overview of the particularities of radiance and cloud property assimilation methods in the previous sections, this section discusses comprehensive aspects of geostationary satellite data assimilation in LAMs for short-term cloudiness forecasting. Moreover, the differences between satellite DA in research and the operational application and future perspectives are discussed.

Bauer et al. (2011a) and Vukicevic et al. (2006) remark that NWP models produce spatial and statistical averages of clouds while the information content about clouds provided by satellite observations is of a different nature. This circumstance explains the complexity of determining four-dimensional cloud analyses and why many authors focus on moisture analyses rather than the adaptation of variables linked with hydrometeors. It is this issue on the side of the weather models, and the complete exploitation of available cloud observations on the side of remote sensing, which still offer much room for improvements.

Several studies in both fields of radiance and cloud property assimilation raise the crucial question of how long the assimilated information provided by satellite observations is influential in the model forecast. In the context of this thesis on GHI forecasts, this question corresponds to research question 3 in chapter 1 ("Until what forecast lead time is the impact of satellite data assimilation on GHI forecasts noticeable?"). The answer to this question illustrates the impact of satellite data assimilation, which can be considerably large. Several works (Bayler et al., 2000; Bauer et al., 2011b,a) hypothesize that the additional information by cloud-affected satellite data vanishes after the first few hours of simulation. Yucel et al. (2003) assume that this is because of potential discrepancies between the unchanged dynamic field and the updated cloud analysis. While a loss of cloud information within the first 24 hours is found in several publications (Lipton and Modica, 1999; Taylor et al., 2008; Singh et al., 2010; Chen et al., 2015, 2016), there are also multiple examples in which regional forecasts improve for lead times beyond 24 hours thanks to geostationary satellite data assimilation (Zapotocny et al., 2005; Zou et al., 2011; van der Veen, 2013). This indicates that the impact can potentially be large and that further improvement of the methods might lead to longer lasting impacts. Nevertheless, the predictability of clouds depends on their type. Due to their limited predictability, convective clouds cannot be expected to show long impact durations when assimilated. Hohenegger and Schär (2007) demonstrate that the high degree of nonlinearity in cloud-resolving models limits predictability at cloud-resolving scales.

Many studies evaluate the functionality of their new developments in case studies, which is probably due to limited computational capacities, particularly regarding ensemble-based methods. Apart from the satellite DA method, the configuration and tuning of the model also plays a big role regarding the impact duration, ensuring that the injected clouds do not directly disappear after the initialisation. For example, Chen et al. (2016) found that among several tested microphysics schemes the use of the WRF double moment 6-class (WDM6) scheme leads to the longest impact duration in their case. In general, more studies should evaluate the applied DA methods in connection with the model configuration in order to optimise the forecast impact duration. The LAM domain size certainly plays an important role regarding the impact duration, since the information given from the global to the limited-area model via the lateral boundary conditions highly influences and "washes out" the initial information in the regional domain at some point (Gustafsson et al., 2018). It may be supposed that this effect becomes smaller the larger the domain is, as some studies mentioned in the previous sections indicate. This is to be validated in detail by future studies.

Moreover, none of the identified peer-reviewed papers compare the impact duration of radiance and cloud property assimilation in LAMs. Both strategies are able to produce positive impacts but a definite decision regarding which one has the larger impact on short-term forecasts of clouds cannot be made at this time.

The majority of the studies focuses on the assimilation of few channels or cloud

properties in order to achieve a positive impact. Thus, the entirety of available channels and cloud properties is still far from being exploited. This is because for a respective NWP and DA system, diverse issues like bias correction, quality control or error estimation have to be thoroughly handled before extending the number of utilised observations.

Moreover, physical cloud property DA is linked to the errors induced by cloud property retrieval algorithms, additionally to the error of the observed radiances. Since the initial observations are radiances, the information content about cloud and precipitation physics is limited (Errico et al., 2007b) and sometimes biased, especially when optically thin clouds create a mixed signal of radiation from the background and the cloud (Polkinghorne and Vukicevic, 2011). Such problems can be overcome by using NWP output to correct the cloud information. Therefore, in the data assimilation scheme of the same model, the same background information is used twice, which might lead to suboptimal analyses (Migliorini et al., 2008). The use of NWP background information in retrieval algorithms is thus a major shortcoming of cloud retrieval assimilation.

According to the majority of studies in section 2.3, radiance assimilation especially improves upper-tropospheric moisture and cloud features in situations with "smooth" cloud systems like stratus clouds, but has less attested impact on convective clouds and their evolution. Cloud property assimilation methods allow to inject clouds more radically and thus have more potential to improve short-term forecasts in convective situations. So far, only a few cloud property assimilation studies consider ensembles. Important uncertainty information might be derived from the ensemble and further improve the methods. In this regard, the implementation of stochastic elements in parameterization schemes might provide enhanced information about the ensemble spread (Bengtsson et al., 2013). Furthermore, there is a lack of extensive 4D-Var studies of radiance assimilation with the widely-applied WRF model. These could be compared to the diverse ensemble-based radiance DA developments.

For these various reasons, the realisation of long-term comparison studies is desirable in order to fully evaluate the potential of the innovations and the forecast impact duration. Moreover, long-term studies of both radiance and cloud property assimilation methods with the same model would allow a more thorough assessment of the impact of the approaches with a limited influence of the model configuration and tuning. The complexity of cloud property assimilation methods is diverse (de Haan and van der Veen, 2014; Schomburg et al., 2014; White et al., 2018). Some methods are tailored for certain cloud types (Mathiesen et al., 2013) or cloud properties (Jones et al., 2013b; Kumar and Varma, 2016). Comparing the performance of different methods under similar conditions would reveal whether more complex or computationally expensive methods perform better than simpler methods. Nevertheless, the conduction of such studies requires a common and globally applicable verification framework to assess the impact of the different methods. Such a framework does not currently exist and every author group uses

different data for cloud analysis and forecast evaluation, like polar-orbiting satellite observations, reanalyses, radar, irradiance or other ground-based observations.

The evolution of clouds is far from being exhaustively considered in the process of determining a cloud analysis in both radiance and cloud property assimilation. Smoothing data assimilation methods (van Leeuwen, 2001) aim at improving the temporal consistency and have not yet been extensively applied to the diverse cloud analysis issues. The shortcoming is that they are computationally expensive and require four dimensional adjoint models (Vukicevic et al., 2006). Nevertheless, it is desirable for both radiance and cloud property assimilation to better account for observed cloud evolution in the assimilation process.

Differently than in research, operational activities require a definite choice of the applied data assimilation procedure. Furthermore, while the impact of different satellite data assimilation methods on cloudiness forecasts can be investigated in detail in a research context, the operational context requires decisions to be made. The choice of an operational assimilation method always depends on the chosen model and its available data assimilation capabilities. The method has to be customised for the applied NWP model and its state or moisture variables. It is rather the entirety of available observations of all types that is considered in an operational context as well as the improvement of scores of all forecasted variables in the entire three-dimensional model domain. By trying to assimilate a maximum of available observations, the borders between radiance assimilation and cloud property assimilation become blurred. A comparison of research and operational activities and achievements reveals that there is a transition going on in operational cloud analysis determination and short-term forecasting of cloud-related parameters: Clear-sky radiance assimilation using cloud mask/cloud type classifications and the assimilation of simple cloud information like cloud-top temperature can be considered the operational standard with LAMs (Gustafsson et al., 2018). This is now being updated by a more sophisticated assimilation of elaborated cloud products and all-sky radiances.

Several systems - especially operational ones - use multiple observations to make an exhaustive three-dimensional cloud analysis. Previously mentioned examples are the systems or models ARPS, LAPS, MMR and NAE. Two operational state-of-the-art systems that have not been mentioned yet are the Rapid Refresh (RAP) model and the AROME (Application de la Recherche à l'Opérationnel à Méso-Échelle) model.

For short-term forecasting with a forecast length of 18 hours NCEP operationally runs RAP for the US, which replaced the Rapid Update Cycle (RUC) model in 2012 (NOAA/NCEI, 2017). Rapid Refresh is an assimilation/modelling system, based on RUC, WRF and GSI (Benjamin et al., 2016b) that uses a hybrid 3D-Var/Ensemble data assimilation approach (Pan et al., 2018). GOES-derived cloud-top height temperature are incorporated as it had already been the case in the RUC system (Benjamin et al., 2004). Hu et al. (2007) and Weygandt et al. (2006) provide further information about the cloud analysis scheme of RUC/RAP.

Since August 2016 the assimilation system also integrates GOES radiances (Benjamin et al., 2016a).

In the AROME model, operated by Météo-France, SEVIRI clear-sky radiances are selected using a cloud type product and assimilated with a 3D-Var system (Guidard and Fourrié, 2010) in an hourly assimilation cycle (Brousseau et al., 2016). The model is highly resolved with a grid spacing of down to 1.3 km and the impact of using a higher resolution on convective events in conjunction with DA has been analysed by the latter authors.

Detailed evaluations of the impact of only geostationary satellite observations in such operational systems are usually not available and the systems are tailor-made for certain geographical regions and the respective observations.

2.6 Conclusions

This chapter presents a comprehensive review about the assimilation of atmospheric observations made by geostationary meteorological satellites in limited-area models with the goal of improving short-term forecasts of cloud-related parameters.

Two fundamentally different approaches can be distinguished: sensor-observed radiance or brightness temperature assimilation and retrieved cloud property assimilation. The question of which assimilation strategy is the most suitable one for a certain application depends on several factors: the available computational capacity, the requirements of the performed simulations in terms of forecasted variables and computational cost and the sophistication of the NWP model with its associated DA system. Generally, cloud property assimilation is rather targeting computationally spare and frequently updated forecasts of short-term cloud evolution, while radiance assimilation is usually applied in connection with computationally costly variational or ensemble-based DA systems which are designed to incorporate various sources of observations for short-term and long-term forecasts of not only cloud-related parameters. It is thus primarily a matter of lead time and application which technique should be focused on, while in the end both methods aim at finding optimal NWP initial conditions.

The literature review shows that in both fields, radiance and cloud property assimilation, numerous improvements have been made recently. All radiance assimilation studies have found a positive impact on analyses and/or forecasts of cloud-related parameters through assimilation of geostationary satellite radiances. Reduced errors are mainly found for moisture and temperature fields especially in the mid-to-upper troposphere and for cloud-related parameters (e.g. cloud mask or precipitation). Although clear-sky radiance assimilation in LAMs still can be improved, many studies directly aim at assimilating cloud-affected radiances to maximise the use of available observations. Nevertheless, even without considering cloud-affected radiances, clear-sky radiance assimilation has the potential to im-

prove short-term regional-scale forecasts of cloud-related parameters. Compared to variational DA methods, ensemble-based DA has the advantage of providing flow-dependent information about the model background error that may be especially useful for all-sky radiance assimilation. In peer-reviewed literature, this matter has not yet been exploited using hybrid DA methods in LAMs.

Cloud property assimilation methods also improve short-term cloud forecasts, while a quantitative comparison of their outcome is rather difficult due to the diversity of methods and retrievals and their evaluation in individual case studies. The complexity extends from rather simple methods that primarily modify model cloud-top properties like cloud-top temperature via methods that also try to take the dynamical fields into consideration up to computationally expensive variational/ensemble-based methods. The latter are the minority since a common objective of cloud property assimilation methods is the possibility to create as complete cloud analyses as possible without large computational efforts. Existing cloud property assimilation methods are often targeted for specific LAMs, geographical regions or synoptic conditions and often depend on additional observations than those provided by geostationary satellites. Little efforts have been made in order to design and evaluate cloud property assimilation methods for LAMs that are applicable anywhere in the world and that exploit geostationary retrievals without the necessity of involving further observation types. Moreover, vertical columns are considered in many methods rather than the three-dimensional evolution of cloud properties and the dynamical implications of modified cloud analyses are often neglected.

Many DA systems for LAMs, especially operational ones, are tailored for a certain geographical region and the assimilation of the specific observations that are available for that region. Such systems are not readily applicable to all locations or satellites. In order to evaluate the full potential of developed data assimilation methods using geostationary satellite observations and limited-area models, future developments should be tested with different limited-area models and satellites. With the target of providing more accurate cloudiness forecasts for demanding applications like solar power forecasting that require frequently updated short-term forecasts, cloud analysis methods should be evaluated on a long-term basis, for different geographical regions (e.g. mid-latitudes and the tropics), and for locations where other observations are sparse in order to make the best use of geostationary satellites.

The topic of radiance or cloud property assimilation comes along with diverse problems and challenges to be overcome, e.g. the choice of satellite channels or retrieved cloud properties and their optimal processing, the non-linearity of cloud processes, observation quality control, bias correction and subsampling, cloud classification and localisation, observation and background error estimation, computational efficiency, domain size, domain location and grid spacing optimisation.

Several publications that are referred to in this chapter tackle diverse issues of cloud DA by further developing the assimilation strategies and methods. Neverthe-

less, only some of the publications evaluate the methods at convection-permitting scales. The potential advantage of limited-area models of providing high-resolution forecasts of clouds in combination with geostationary satellite DA is thus unexploited so far.

The ability of a data assimilation system to assimilate cloudy observations is closely tied to the ability of the LAM to produce realistic clouds in the model background. Improvements of model parameterisation schemes, e.g. by introducing stochastic elements, are thus expected to positively influence DA performance and keep increments small. Likewise, improved radiative transfer models directly impact satellite DA performance and facilitates the assimilation of observations from new satellites.

Considering the diverse conclusions, the first objective of this thesis can be answered:

Objective 1 *The identification of a promising geostationary satellite data assimilation approach for regional-scale NWP regarding clouds and solar irradiance forecasts in the tropics.*

Several considerations in this chapter inform the methodology applied in this study. Firstly, the literature review shows that the use of ensembles has become increasingly favoured, demonstrated by the growing number of hybrid DA methods. Secondly, the WRF model is the most widely applied LAM regarding both radiance and cloud property assimilation in peer-reviewed literature. Thirdly, it is shown that although multi-layer cloud property products from geostationary satellites do exist, they have been largely neglected so far by cloud property DA methods. For these and the aforementioned reasons, among the existing cloud property assimilation approaches, the approach of Jones et al. (2013b) is chosen as it appears to be one of the most innovative and promising ones for short-term cloud cover forecasting. The forward operator for CWP is applied to the multi-phase retrievals provided by SatCORPS. The next chapter provides detailed information about this methodology.

Chapter 3

Data and methodology

Contents

Summary

This chapter deals with two major subjects. Firstly, the details of the chosen setup in terms of the NWP model and DA system, and secondly, an explanation of the performed experiments that are evaluated in the two following chapters. Based on the findings in the previous chapter, the approach that is chosen for the experiments in this thesis is multi-phase cloud water path (CWP) assimilation with an ensemble Kalman filter using the Weather Research and Forecasting (WRF) model. The lateral boundary conditions (LBCs) for the 40 member WRF analysis ensemble are obtained from the Global Ensemble Forecast System (GEFS) and one deterministic WRF member uses LBCs from the Global Forecast System (GFS) at a higher spatio-temporal resolution. The utilised data assimilation software is the Data Assimilation Research Testbed (DART) and its forward operator for cloud water path. The cloud water path retrievals are obtained in a gridded format and in three phases (ice, supercooled liquid, and liquid) from NASA Langley's SatCORPS cloud products. Two cycling experiments are performed. One control experiment without DA and one experiment with DA. The cycling interval is 6 hours and free forecasts, covering the next 40 hours, are launched every 24 hours from the 0000 UTC analyses from the cycling. Experiments with a one-way nested domain are also performed

to investigate the effect of different grid spacings. A number of operational numerical weather prediction models are considered for comparison with the performed WRF experiments. Moreover, the error metrics that are used for forecast evaluation, as well as independent observations (solar irradiance and radio soundings) are described in this chapter.

3.1 Introduction

The setup up of a LAM in combination with an ensemble DA cycling system requires a number of decisions that have to be made about the configuration. Some topics that require decision making are the choice of parameterisation schemes, the LAM domain size, the number and resolution of nested domains, the ensemble size, the origin of LBCs and ICs, the cycling interval, the DA approach (chapter 2), the origin and treatment of the assimilated observations and associated aspects such as the definition of observation errors and localisation. For many of these topics there is no predefined right or wrong choice. Ongoing research in atmospheric science continuously produces new findings regarding these specific aspects and facilitates decision making more and more. Besides the setup of the model and DA system, the experiment design needs to be well defined. This includes aspects such as the choice of the study period, the length of performed forecasts, and the origin and treatment of independent observations for validation.

Individual decisions have been made in the numerous studies that are cited in chapter 2, which leads to the variety of existing approaches and results. After the review of existing studies and the general choice of the DA approach in the previous chapter, this chapter explains the setup that is used in the performed experiments. The choices that are made for the model and DA configuration as well as the experiment design are explained in sections 3.2, 3.3, and 3.4. Explanations about the independent observations that are used for validation are given in section 3.5 for radiosoundings and in section 3.6 for GHI. The methods that are used for forecast evaluation are presented in section 3.7. An overview of the operational models that are considered for comparison with the performed WRF experiments is given in section 3.8.

3.2 Model and cycling configuration

The LAM that is used in this study is the WRF model in its Advanced Research WRF (ARW) version 3.9.1.1. WRF is mainly developed and maintained by NCAR, NOAA and NCEP. Moreover, a large international user community contributes to this open-source model.

In the performed experiments, a single WRF domain is applied over a part of

the southwestern Indian Ocean including Reunion Island and Mauritius in its centre (figure 3.1). A horizontal grid spacing of 12 km and 61 vertical levels stretching from the surface up to 50 hPa are used. The data assimilation experiments are not performed at convective-scale model resolution as preliminary test simulations for Reunion Island and studies of other regions (Lara-Fanego et al., 2012; Zhou et al., 2018) have shown that increasing the WRF grid spacing does not necessarily improve the performance of irradiance forecasts. A potential reason for this is that nonlinearity increases with increasing model grid spacing (Mass et al., 2002; Hohenegger and Schär, 2007). Moreover, DA with a two-way nested domain is considerably more complex. The reason for this is that the updated analyses of the nested domains must be physically consistent with those of the parent domains. However, additional experiments with a one-way nested domain have been performed as described in secion 3.4.

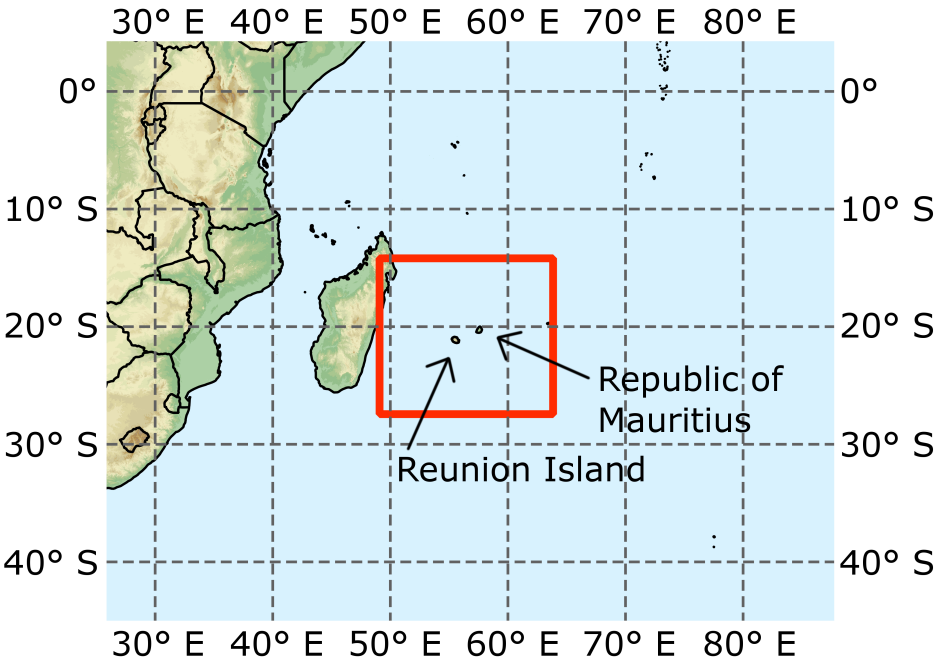

Figure 3.1 – Study region and WRF domain (red rectangle) in the southwestern part of the Indian Ocean.

The WRF ensemble that is run in the conducted experiments uses initial and boundary conditions from the Global Ensemble Forecast System (GEFS) and the Global Forecast System (GFS) (figure 3.2). The GEFS, which has a grid spacing of 0.5°, 27 vertical levels, and a temporal resolution of three hours, consists of 21 ensemble members and provides the WRF ensemble with LBCs and ICs. In preliminary experiments, WRF GHI forecast errors were lower when GFS LBCs were used compared to simulations with LBCs from the IFS model (not shown). Using IFS, WRF heavily underestimated the presence of clouds compared to simulations

using GFS. This indicates that the use of ECMWF LBCs together with the applied configuration of WRF requires a more thorough diagnostics before being pursued. Consequently, WRF is run with GFS and GEFS in this study, which is a standard setup in the WRF user community.

In terms of ensemble size, a compromise between computational cost and performance needs to be found. Several DA studies with LAMs use around 40 members (Pan et al., 2014; Dillon et al., 2016; Schraff et al., 2016; Zhang et al., 2018). In line with these studies, an ensemble consisting of 40 WRF members plus one deterministic member is applied in this study. It is distinguished between the "analysis ensemble" (members 1 to 40) that is used to derive the analysis in EnKF cycling, and the "deterministic member" (member 41). The 40 analysis ensemble members are obtained using GEFS and the deterministic member is obtained using the deterministic GFS forecasts. When using LBCs with a higher spatio-temporal resolution for a deterministic member, it is to be expected that this member is the most realistic one, since the other ensemble members should be equally likely. One possibility to obtain 40 analysis ensemble members is to use perturbed LBCs from GFS. However, in this approach the ensemble spread only depends on perturbations. Using original GEFS members leads to a supposedly more realistic ensemble spread that varies depending on the weather situation. The LBCs and ICs of members 1-20 of the WRF ensemble are generated from the original 20 GEFS members. In order to obtain 40 members using GEFS, the LBCs and ICs of members 1-20 are perturbed with the WRFDA system (Barker et al., 2012) using the standard NCEP background error covariance (Parrish and Derber, 1992) to generate WRF members 21-40. The GFS with a grid spacing of 0.25°, 32 vertical levels, and a temporal resolution of one hour is used for the LBCs and ICs of the deterministic (the 41st) WRF member. Initial conditions for all members are only generated from GEFS and GFS at the start of the DA cycling after which they are fed in from the previous cycling step (figure 3.2).

All WRF ensemble members use the same model configuration, this includes the Thompson microphysics scheme (Thompson et al., 2008), the Dudhia scheme for shortwave radiation (Dudhia, 1989), and the Kain-Fritsch scheme (Kain, 2004) for cumulus parameterisation. These schemes are among the most commonly used in WRF configurations according to a WRF user physics survey (UCAR, 2015) and this configuration also performed well for Reunion Island in preceding experiments (not shown).

Since the deterministic member (member 41) uses the LBCs with the highest spatio-temporal resolution, this member is chosen for free forecasts that are realised every 24 hours at 0000 UTC (0400 local time) using its updated analyses (ICs) from the DA cycling (blue arrow in figure 3.2). The hourly LBCs for the free forecasts are likewise provided by GFS and are generated for a maximum lead time of 40 hours. The term "free forecasts" is used to distinguish these forecasts from the six hour first guess forecasts that are "bound" by the cycling procedure.

The DA cycling interval is 6 hours, leading to 4 cycle steps per day, i.e. DA is

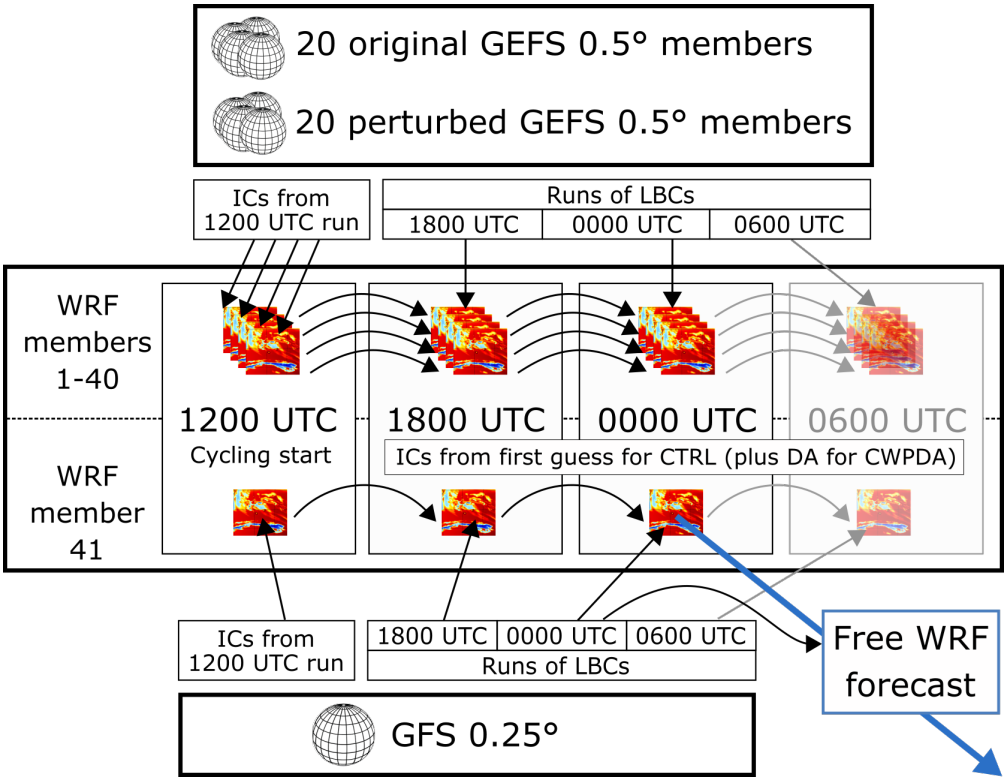

Figure 3.2 – Schematic illustration of the 41-member WRF cycling procedure using GEFS and GFS for initial and lateral boundary conditions. Analyses and first guess forecasts are produced every six hours, while free forecasts (as opposed to the "cycled" forecasts) are generated every 24 hours from the 0000 UTC analysis of the deterministic member.

performed at 0000, 0600, 1200 and 1800 UTC leading to new analyses (also referred to as "posteriors") at these times. These analyses are then used to perform first guess forecasts (also referred to as "priors") of the following 6 hours (figure 3.2). As satellite observations are available more frequently than every 6 hours, it is possible to reduce this interval to provide updated analyses for free forecasts (FF) at a higher update rate than 6 hours. However, assimilating the observations more frequently increases the technical complexity of the methodology considerably, which is why 6-hourly cycling is performed.

Figure 3.3 illustrates some operations that are undertaken at each DA step associated with the WRF ensemble to proceed from the first guess to a new analysis. The shown steps of inflation and re-centering are explained in the following. Different aspects concerning the EnKF step, the retrievals and localisation are explained in section 3.3.

The number of members of an ensemble is generally low compared to the number of degrees of freedom of the model. Thus, the ensemble must be prevented from being "over-confident" and collapsing to a single solution. A commonly used

method to address this issue and increase prior ensemble variance is covariance inflation (figure 3.3). DART comes with built-in spatially-varying state space adaptive covariance inflation (Anderson, 2007, 2009), which is applied at each cycling step.

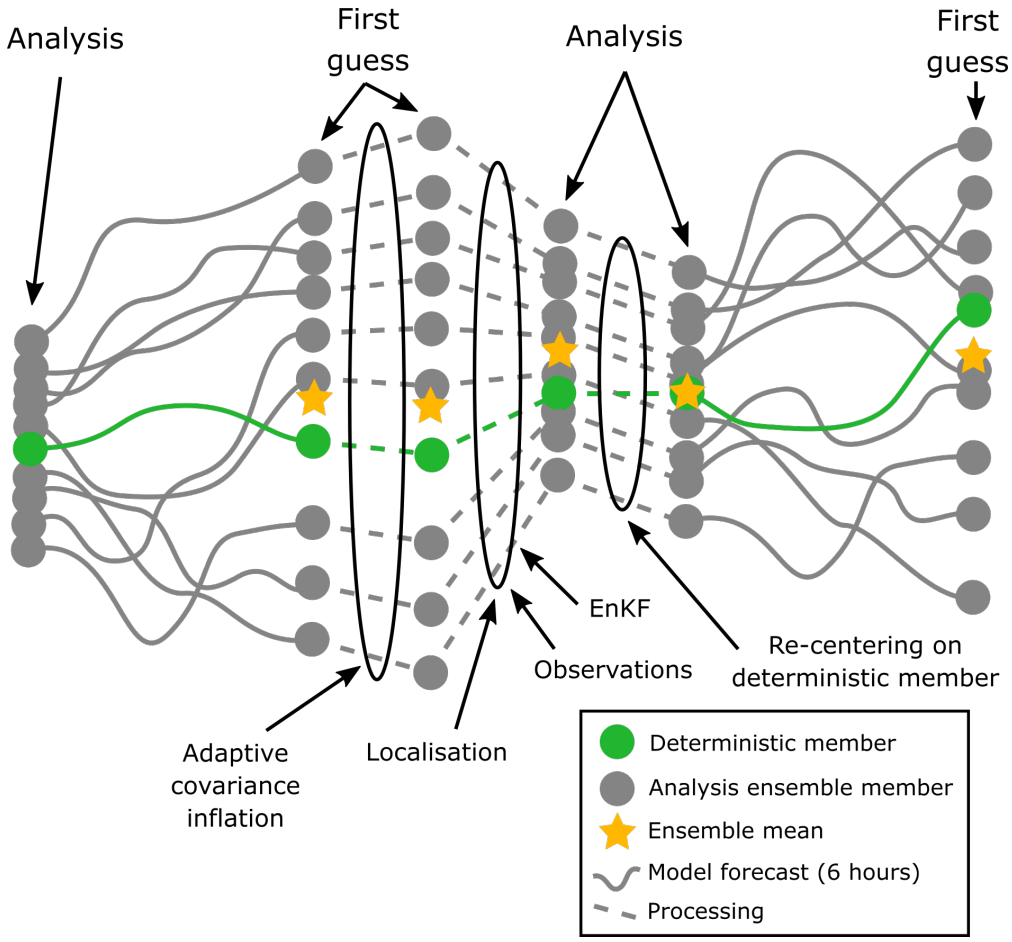

Figure 3.3 – Schematic illustration of WRF ensemble DA process steps at a given analysis time. The evolution of nine exemplary analysis ensemble members (grey) and the deterministic member (green) are shown. The six hour first guess forecasts are illustrated by the solid lines. Dashed lines represent different process steps at the analysis time, such as adaptive covariance inflation, the EnKF step, and the re-centering of the analysis ensemble on the deterministic member. An exemplary ensemble mean is represented by the orange stars to illustrate the re-centering process after which the deterministic member is the new ensemble mean.

After each EnKF step the analysis ensemble members (members 1 to 40) are re-centred on the deterministic member (member 41). This technique is also applied operationally at NCEP (Collard, 2017). The ensemble mean is subtracted from each member to obtain the deviation from the mean for each member. These perturbations are then individually added to the deterministic member to re-generate the analysis ensemble, which then has the deterministic member as its mean (fig-

ure 3.3). This way, the skill of the analysis ensemble is supposedly maximised and it is ensured that the analysis ensemble does not diverge too far from the deterministic member.

Two main cycling and free forecast experiments are performed: A cycling experiment with CWP DA (CWPDA) and a control cycling experiment without DA where all observations are only evaluated by DART but not assimilated (CTRL). The respective free forecast experiments that are run using the 0000 UTC analyses of the two cycling experiments are labelled CWPDA-FF and CTRL-FF. An overview of all WRF experiments and their denotations is given in section 3.4.

Meteosat-8 is in operation over the Indian Ocean since February 2017 and GHI forecast errors are much larger in austral summer (section 1.3). Therefore, all experiments of this study are performed for the austral summer of 2017 and 2018, more specifically between 9 December 2017 and 1 March 2018. Some periods are excluded in the simulations due to gaps in CWP data availability and cyclonic activity. Tropical cyclones produce extreme conditions in terms of clouds and are therefore omitted in the performed experiments. This includes the periods when the tropical cyclones named Ava (1 January 2018 to 9 January 2018) and Berguitta (13 January 2018 to 20 January 2018) were active in the WRF domain. Therefore, cycling is performed for several smaller periods, listed in table 3.1. The convective activity is generally pronounced during these periods and in each case at least two DA steps are performed before using a 0000 UTC analysis for the respective free forecasts periods listed in table 3.1.

3.3 CWP assimilation methodology

The DA cycling is performed using the DART and its Ensemble Adjustment Kalman Filter (Anderson, 2001) and the CWP forward operator developed by Jones et al. (2013b) is used to assimilate CWP observations. Jones et al. (2015) describe a few updates to the forward operator, which is close to the version used in this study.

In comparison to other cloud property assimilation methods that do not take into account multi-level cloud information, one strength of this forward operator is that it accounts for cases when the model and CWP observations contain clouds that are localised at different altitudes. The forward operator does this through adjustments to the modelled CWP. For example, if the model contains a low level cloud and the observations indicate high level cirrus, the integrated CWP value might be similar and the impact to the model analysis would be small if the cloud altitude was not considered. In this case, the forward operator constrains the model CWP to the level of the observed cloud, leading to a larger impact in the analysis and a cloud is introduced at the correct vertical location.

The SatCORPS cloud products are retrieved using algorithms originally developed to analyse MODIS aboard Terra and Aqua for the NASA Clouds and

Table 3.1 – Overview of the cycling experiment periods and the associated free forecast experiment and dates. Columns four and five only refer to the first day (the intraday) of the free forecasts. The last actually forecasted day is 2 March 2018 for which the free forecast was launched using the 0000 UTC analysis from 28 February 2018.

Cycling period	Cycling start (UTC)	Cycling end (UTC)	Dates of free forecast	Number of days forecasted
A	2017-12-09 1200	2017-12-12 0000	2017-12-10 to 2017-12-12	3
B	2017-12-19 0000	2017-12-27 1800	2017-12-20 to 2017-12-27	8
C	2018-01-08 1200	2018-01-13 0000	2018-01-09 to 2018-01-13	5
D	2018-01-20 1200	2018-01-31 1800	2018-01-21 to 2018-01-31	11
E	2018-02-11 1200	2018-02-13 0000	2018-02-12 to 2018-02-13	2
F	2018-02-14 0000	2018-03-01 0000	2018-02-15 to 2018-03-01	15

the Earth's Radiant Energy System (CERES) project (Minnis et al., 2011; Trepte et al., 2019). These algorithms have been adapted to other imagers aboard geostationary (Minnis et al., 2008) and other low Earth-orbit satellites (Minnis et al., 2016). Among other parameters, the SatCORPS data set include both a pixel and a gridded CWP product (figure 3.4).

The figure illustrates how the gridded data is derived using the pixel data. Depending on the cloud top phase, as determined from CTT, a given pixel is defined as either ice, supercooled liquid or liquid under the assumption that the cloud phase and particle size are vertically homogenous. The actual CWP is derived as a function of total optical depth and particle size retrievals. SatCORPS provides water path (WP) retrievals in three phases: liquid water path (LWP), supercooled water path (SWP) and ice water path (IWP). The supercooled phase is determined using a post retrieval classification. If the pixel phase is liquid and has a CTT below 273.15 K the pixel phase is defined as supercooled liquid. The retrievals of the different phases are assimilated as independent observations using the same forward operator which can be considered as multi-layer cloud property

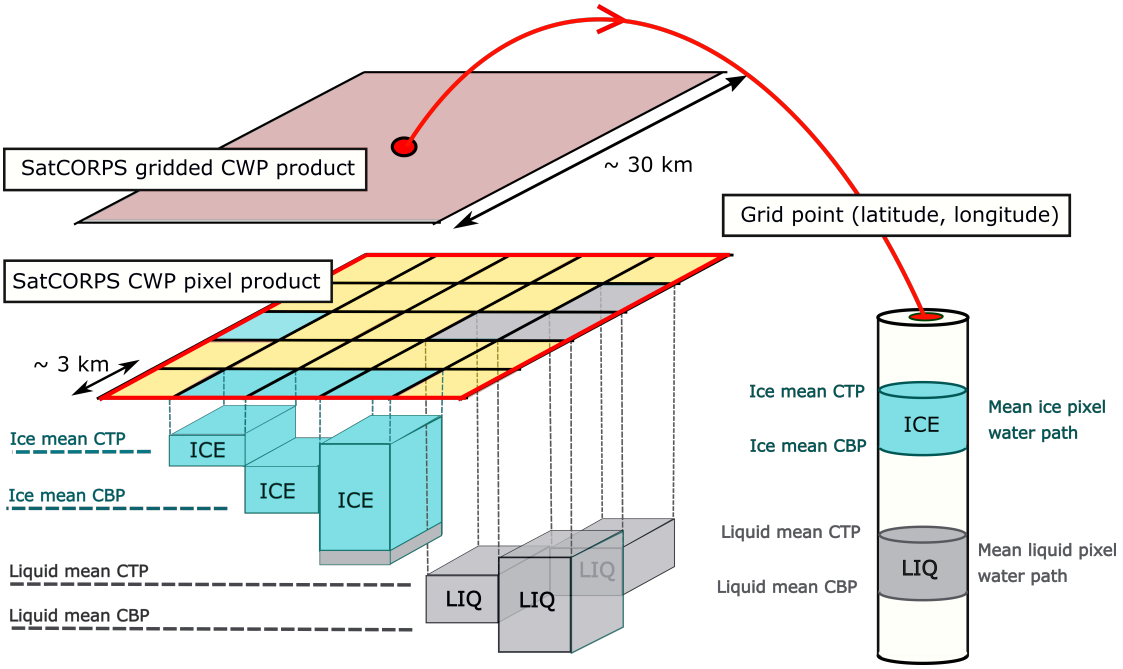

Figure 3.4 – Illustration of the difference between the SatCORPS pixel and gridded product in terms of WP, CBP, and CTP. Only the two phases ice and liquid are shown, since the supercooled phase is determined using a post retrieval classification.

assimilation.

The satellite data represent gridded means of 2-d horizontal fields. It is possible that pixels that are classified as ice pixels actually overlap liquid clouds and the retrieved IWP would include the liquid contribution (figure 3.4). In the case that the gridded mean IWP is less than the mean LWP, one reason could be that not all ice pixels are overlapping liquid clouds. There is no assumption regarding how cloud properties derived from adjacent pixels overlap in a gridbox.

The global gridded data have a grid spacing of 0.25° (approximately 28 km) latitudinally and 0.3125° (approximately 34 km) longitudinally and are independent of the respective satellite sensor resolution (i.e. the resolution of the pixel product). The data are available at hourly resolution in near real time. This is the first study to assimilate the gridded retrievals that are derived from the SEVIRI sensor aboard Meteosat-8. The satellite has a sub-satellite position of 41.5° East.

At night, the retrievals of cloud optical depth are not as accurate as during daytime due to the lack of visible data. Therefore, default values of cloud optical depth and particle size are used within the SatCORPS retrieval algorithm. The effect of this circumstance is visible in figure 3.5, leading to certain peaks in the frequency distribution at certain WP bins at night time. The figure also reveals that the high values of WP are observed more frequently in the ice phase than in the other phases. In fact, the gridded retrievals of LWP and SWP usually do not exceed 0.8 $\mathrm{kg\,m^{-2}}$ at day time and 0.3 $\mathrm{kg\,m^{-2}}$ at night time. In contrast,

IWP reaches values of up to 2.6 kg m^{-2} at day time and 1 kg m^{-2} at night time. Low WP values of less than 0.05 kg m^{-2} occur most frequently in the liquid phase. Taking into account the logarithmic axis for the frequency of occurrence, the figure reveals that low values generally occur much more frequently than high values.

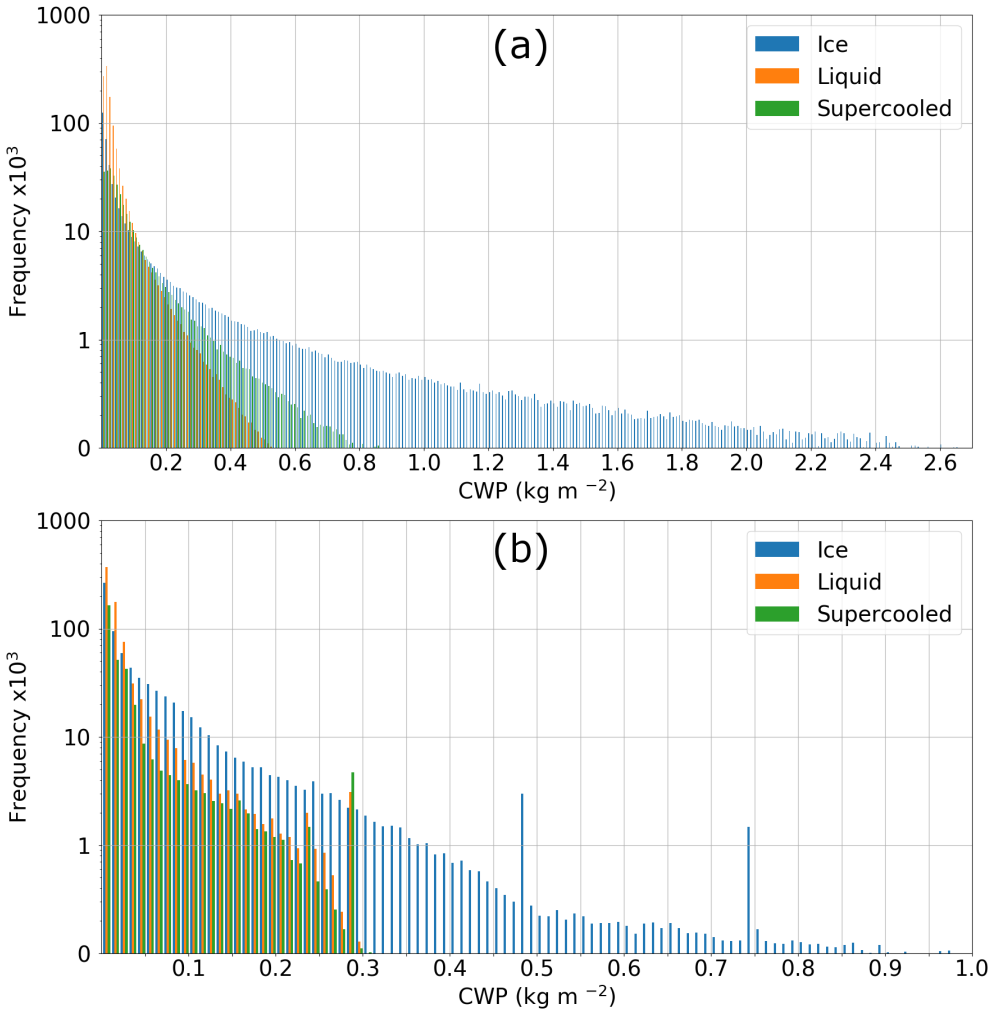

Figure 3.5 – Binned frequency distributions of SatCORPS Meteosat-8 gridded retrievals of IWP (blue), SWP (green) and LWP (orange) on a logarithmic scale at day time **(a)** and night time **(b)**. Note that the horizontal axis is different in (a) and (b). All retrievals inside the WRF domain (figure 3.1) during the study periods listed in table 3.1 are considered.

Each of the three-phased WP retrievals are bound between a CBP and a CTP that are also included in the SatCORPS product (figure 3.4). The forward operator requires information about the cloud effective pressure (CEP) for vertical localisation. Following (Jones et al., 2015) this is set to be the mean of CTP and CBP. The distributions of CBP, CTP and the calculated CEP for each of the three phases are shown in figure 3.6. The figure allows a visual inspection of the

assimilated data and to identify between which pressure levels the WP retrievals are bound most frequently, with the peaks of the CEP distributions being situated between those of CBP and CTP. CEP peaks at approximately 300 hPa for the ice, 550 hPa for the supercooled, and 850 hPa for the liquid phase. Moreover, according to the peaks of CBP and CTP, the IWP retrievals are typically bound between a broader range of pressure levels than the LWP and SWP retrievals.

As this is the first time that SatCORPS gridded Meteosat-8 retrievals are assimilated, a horizontal localisation radius has to be defined for these observations. The Gaspari-Cohn covariance cutoff method is used for horizontal localisation (Gaspari and Cohn, 1999). The half-width of the localization radius (also called cutoff) is set to 90 km, a value that performed well in sensitivity runs. Consequently, there is a factor 3 difference between observation grid spacing (approximately 30 km) and cutoff. This factor corresponds approximately to the factor 3.3 applied by Jones et al. (2015) who use a cutoff of 20 km for satellite observations at 4 km nominal resolution. Figure 3.7 illustrates the issue of localisation and the applied multi-layer cloud property assimilation methodology.

While in radiance assimilation the historical approach is to assimilate only clear sky observations, avoid cloud-affected observations and gradually move towards all-sky assimilation (Chapter 2), an opposite strategy is followed in the cloud property assimilation experiments presented in this work. No clear sky retrievals are assimilated in the experiments in this study. Test experiments showed that including clear sky retrievals in the assimilation led to a strong reduction in the amount of clouds in WRF forecasts with the current experimental setup. The reason for this might be that retrievals with the lowest values of CWP appear much more frequently in the gridded retrieval data than 'more cloudy' retrievals (note logarighmic scale in figure 3.5). Considering all clear sky observations in the EnKF might dry the model out and remove too many clouds from the analysis. This means that defining a minimum threshold for 'cloudy' WP retrievals allows the EnKF to predominantly assimilate observations over cloudy locations. A minimum threshold of 0.04 $\mathrm{kg\,m^{-2}}$ is applied to retrievals of all phases to address cases when WRF tends to underestimate cloud presence. This threshold is defined subjectively using figure 3.5.

The same retrieval errors as in Jones et al. (2013b, 2015) are applied (table 3.2). These were defined for the GOES derived pixel data of the SatCORPS product over the US for both IWP and LWP. There is yet to be a study assessing the errors of the gridded product for Meteosat-8 based retrievals. Therefore, these errors serve as a first estimate for this study. The true uncertainty in CWP varies with cloud conditions, solar and viewing geometry and other factors which need to be assessed more thoroughly. Moreover, the difference between day and night time retrievals (figure 3.5) should ideally be accounted for by the retrieval errors. Defining more region specific errors as well as independent errors for each phase may be an objective of future work.

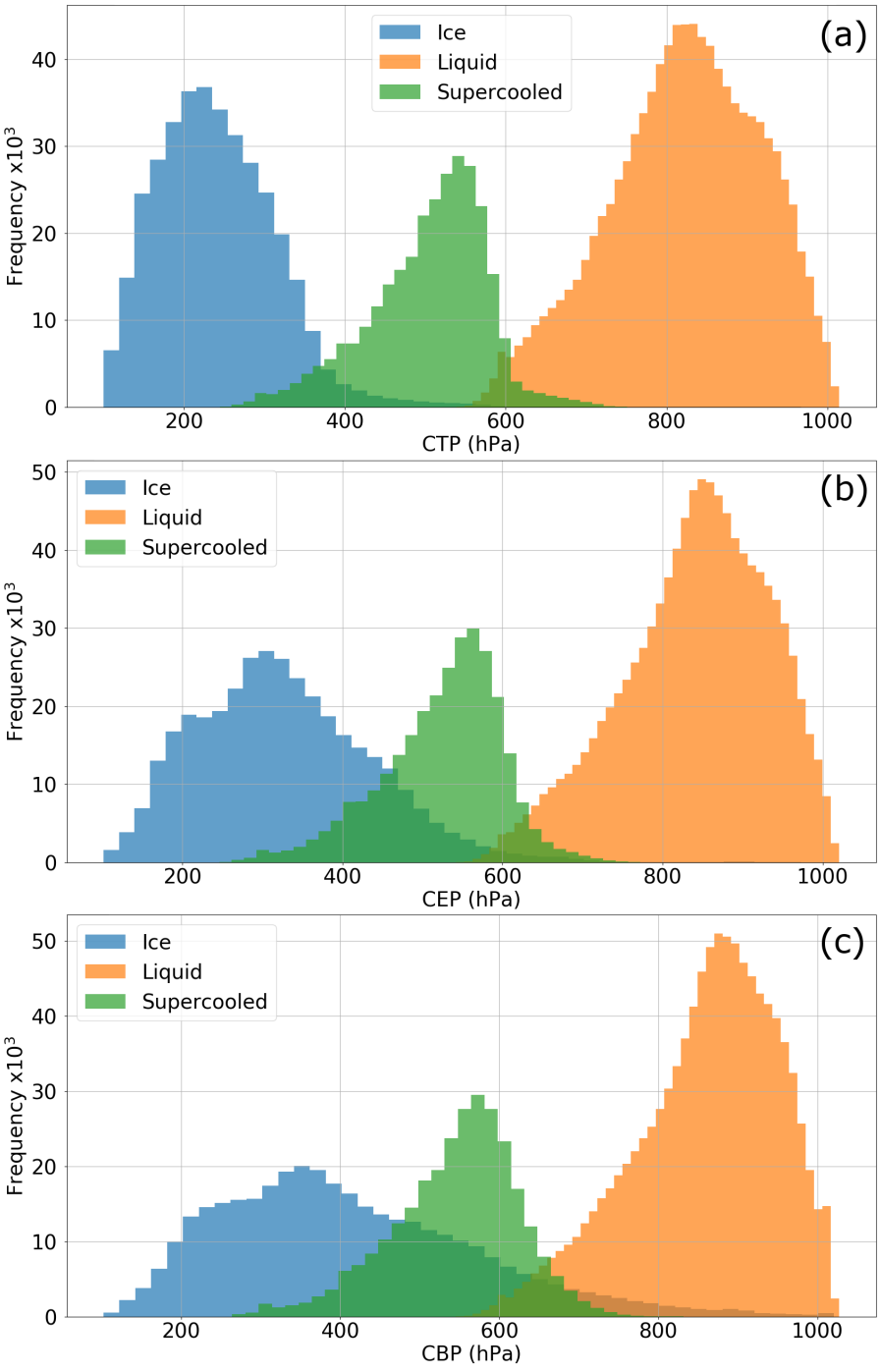

Figure 3.6 – Binned frequency distributions of SatCORPS Meteosat-8 gridded retrievals of CTP (a), CBP (c), and calculated CEP (b). The retrievals of the three phases ice (blue), liquid (orange), and supercooled (green) are shown. All retrievals inside the WRF domain (figure 3.1) during the study periods listed in table 3.1 are considered.

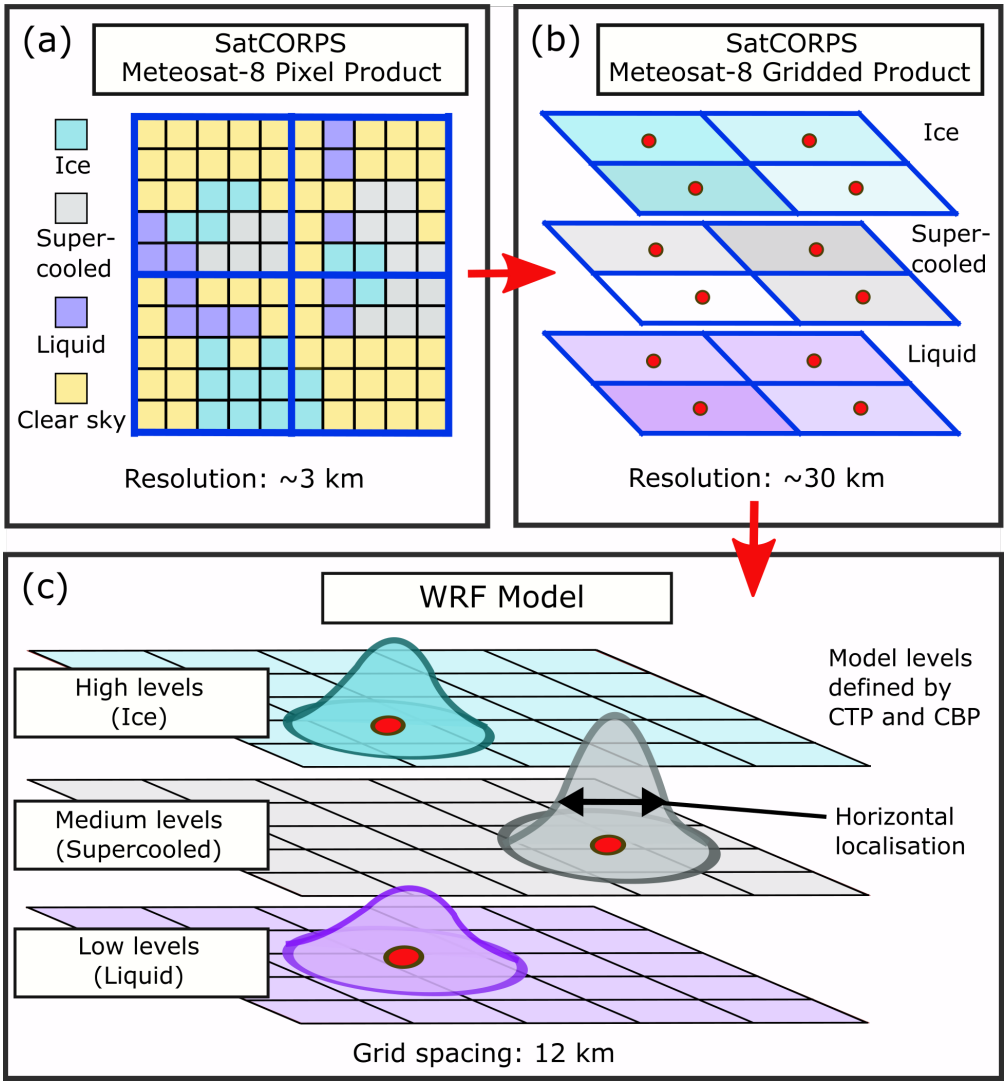

Figure 3.7 – Sketch of the SatCORPS pixel product (a) and gridded product (b) in terms of three-phased WP and localisation of the observations in WRF by DART (c).

Table 3.2 – Overview of the cycling experiment periods and the associated free forecast experiment and dates.

WP thresholds ($\mathrm{kg\,m^{-2}}$)	Assigned WP errors ($\mathrm{kg\,m^{-2}}$)
$0.040 < \mathrm{WP} < 0.050$	0.050
$0.200 < \mathrm{WP} < 0.075$	0.075
$0.500 < \mathrm{WP} < 0.100$	0.100
$1.000 < \mathrm{WP} < 0.125$	0.125
$2.500 < \mathrm{WP} < 0.150$	0.150

3.4 WRF experiment overview

In addition to the base WRF-DART experiment setup described in the two previous sections, two further experiments, one with a nested domain, and one with a classical dynamical downscaling setup, are also performed and evaluated in chapter 5. The goal of these additions is to evaluate the GHI forecast accuracy at different resolutions in connection with DA. The additional setup is explained in this section and an overview of all performed WRF experiments is given.

Additionally to the single domain setup (section 3.2), a second WRF domain with a horizontal grid spacing of 4 km is one-way nested into the domain with 12 km grid spacing (figure 3.8). This means that there is no feedback from the 4 km to the 12 km domain. The applied nesting ratio of 3:1 is the commonly used ratio that is also used by Jones et al. (2013a) and Jones et al. (2015). A two-way nesting with DA in both domains would significantly increase the complexity of the DA methodology since the analyses of the two domains must be physically consistent. Moreover, a grid spacing of 4 km implies a convection permitting resolution, while 12 km grid spacing is not convection permitting. For these reasons, DA is performed only for the 12 km domain as described in section 3.2. The configuration of the nested domain in terms parameterisation is identical to that of the coarser domain. The nested domain has the same amount of vertical levels, i.e. 61.

In case of the experiments with the dynamical downscaling setup (DWNSC), the WRF Preprocessing System (WPS) is used to obtain the ICs for the WRF domain from the 0000 UTC GFS run. This means that a so-called "cold start" is performed for every forecasted day.

The complete list of performed WRF experiments and their denotation is as follows:

CTRL:
Control cycling experiment without data assimilation (see section 3.2).

CWPDA:
CWP data assimilation cycling experiment (see sections 3.2 and 3.3).

CTRL-FF:
Free forecast control experiment with forecasts that are initiated every 24 hours at 0000 UTC using ICs from CTRL (figure 3.2). These forecasts are obtained only from the domain with 12 km grid spacing (see section 3.2).

CTRL-FF-NEST:
Free forecasts obtained from the one-way nested domain with 4 km grid spacing within CTRL-FF (see above in this section).

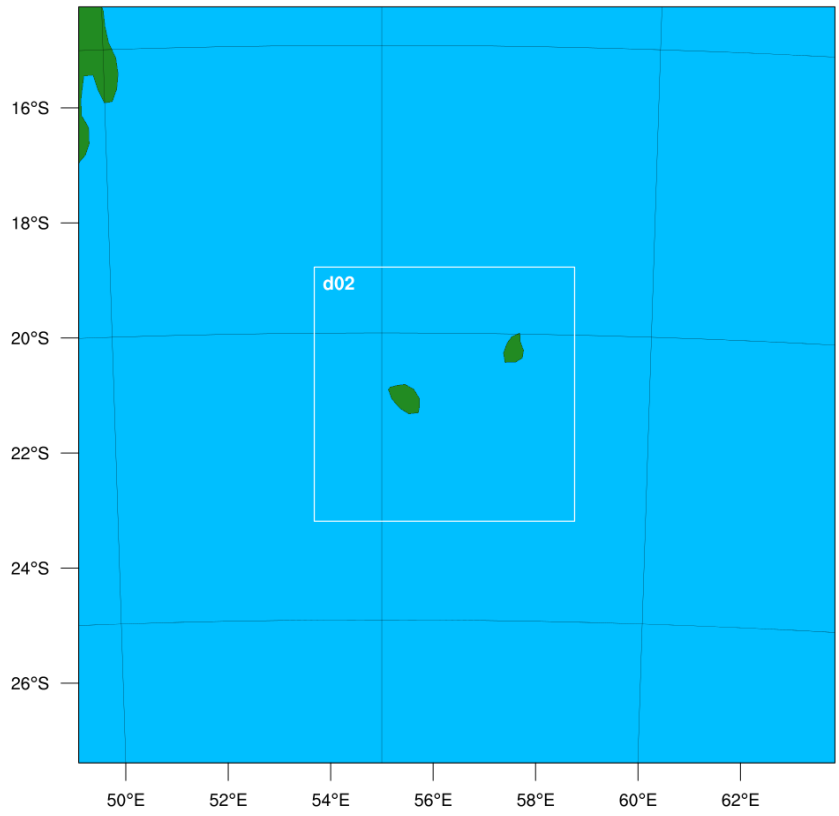

Figure 3.8 – WRF domain setup including one domain with a 12 km grid spacing, and one nested domain with 4 km grid spacing.

CWPDA-FF:
Free forecast CWPDA experiment with forecasts that are initiated every 24 hours at 0000 UTC using ICs from CWPDA (figure 3.2). These forecasts are obtained only from the domain with 12 km grid spacing (see section 3.2).

CWPDA-FF-NEST:
Free forecasts obtained from the one-way nested domain with 4 km grid spacing within CWPDA-FF (see above in this section).

DWNSC:
Classical downscaling setup using ICs directly from GFS (cold start) and not from the cycling experiments. The WRF configuration is identical to that used in the cycling experiments. DWNSC refers to the coarser WRF domain with 12 km grid spacing.

DWNSC-NEST:
Two-way nested domain with 4 km grid spacing, nested into the 12 km domain denoted by just "DWNSC".

3.5 DA evaluation using radiosoundings

Independent observations are used to evaluate the DA method in addition to the assimilated observations. The WRF domain in this study contains one radiosonde station at Gillot-Aeroport (figure 3.9) where radiosondes are launched daily at 1200 UTC. These soundings provide valuable independent in-situ observations that are used for observation space diagnostics. The soundings are available via NCEP's Global Data Assimilation System (GDAS) data set and are evaluated within DART.

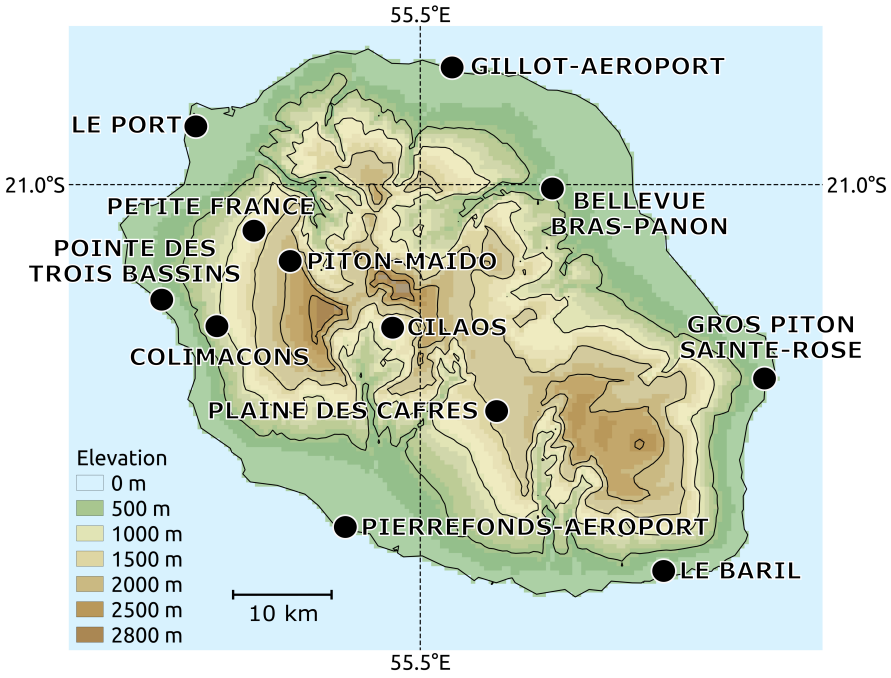

Figure 3.9 – Topography of Reunion Island (21° S, 55.5° E) and the locations of the 12 Météo-France pyranometers used for the evaluation of the WRF solar irradiance forecasts.

3.6 Solar irradiance forecast verification

The evaluation of GHI forecasts is performed using pyranometer observations provided by Météo-France from 12 locations spread across Reunion Island (figure 3.9) at various altitudes between 5 m (Pointe des Trois-Bassins) and 2149 m (Piton-Maido). These sites are selected on the basis of three criteria. Firstly, only sites with a good quality in terms of nearby obstacles are chosen. Secondly, only sites with high quality pyranometers are selected. And thirdly, a homogeneous spatial distribution of the sites is aimed for, i.e. the all regions of the island and multiple altitudes are taken into account. The raw GHI observations have a temporal resolution of 6 minutes and a linear interpolation to 15 minutes is performed to match

the WRF output. The applied quality control measures for GHI observations consist of a visual verification and the sub-hourly data quality control procedures proposed by Espinar et al. (2012) that detect extrema, rare observations and maximum steps for two following measures. The quality-checked time series of GHI observations are shown in appendix A.

It is common to perform spatial averaging of WRF solar irradiance output around the site of interest rather than using only the GHI forecasted for the closest grid box (Lara-Fanego et al., 2012; Verbois et al., 2018; Zhou et al., 2018). This reduces the variability of the forecasted GHI and thus typically reduces forecast errors in terms of the standard metrics, root mean squared error (RMSE) and mean absolute error (MAE). For each GHI forecast at a given location and lead time, inverse distance weighting (IDW) (Shepard, 1968) is applied according to the formula:

$$\widehat{GHI(b_c)} = \frac{\sum_{i=1}^{n} GHI(b_i) d_i^{-1}}{\sum_{i=1}^{n} d_i^{-1}} \tag{3.1}$$

where d_i is the distance between the grid box containing the observation site, b_c, and another grid box, b_i. IDW also addresses the double penalty issue (section 2.2.2), to some extent, by improving the comparability of GHI forecasts at different model grid resoltions. The IDW approach implies that a maximum from the observation site needs to be defined, at which the weight reaches zero. In preliminary test experiments (not shown) with the DWNSC-NEST configuration, the best results are obtained when b_i is considered within a 75 km radius for the large WRF domain with 12 km grid spacing. For the nested domain with 4 km grid spacing, the IDW radius is set to 25 km. Besides IDW, no further post-processing is applied to the WRF solar irradiance forecasts.

Aerosol optical thickness in the study region rarely exceeds 0.2 (Stöckli, 2018) leading to a stable clear sky irradiance on Reunion Island as compared to other regions of the world where aerosol optical thickness is highly variable. In fact, the southern Indian Ocean is one of the world's most pristine regions in terms of aerosol distribution (Mallet et al., 2018). Moreover, the influence of volcanic aerosols on solar irradiance can be neglected as there were no volcanic eruptions on Reunion Island during the overall study period. It is therefore assumed that fluctuations between forecasted and observed GHI caused by aerosols are negligible compared to the influence of clouds.

3.7 Evaluation methods

Various error metrics are considered to evaluate the accuracy of NWP model output as compared to CWP retrievals, radiosoundings and GHI observations. For n predictions, y, of the observation (y can be either a prior or posterior) and observations, o, these metrics are defined as follows. The absolute RMSE is defined

as:

$$RMSE = \sqrt{\frac{1}{n}\sum_{i=1}^{n}(y_i - o_i)^2} \tag{3.2}$$

For some solar irradiance forecast analyses, the clear sky model of the European Solar Radiation Atlas (ESRA) (Rigollier et al., 2000) is used to calculate the normalised RMSE:

$$nRMSE = \sqrt{\frac{1}{n}\sum_{i=1}^{n}\left(\frac{y_i - o_i}{c_i}\right)^2} * 100 \tag{3.3}$$

with c_i being the clear-sky GHI.
The MAE is defined as:

$$MAE = \frac{1}{n}\sum_{i=1}^{n}|y_i - o_i| \tag{3.4}$$

MAE becomes the mean bias error (MBE or simply bias) if the absolute of $y_i - o_i$ is not taken in equation 3.4.
The correlation (or Pearson correlation coefficient) is defined as:

$$corr_{y,o} = \frac{cov(y,o)}{\sigma_y \sigma_o} \tag{3.5}$$

with cov being the covariance and σ being the standard deviation.
The total spread (TSPRD) is defined as the pooled spread of the ensemble and observation errors:

$$TSPRD = \sqrt{\frac{\sigma_y + \sigma_o}{2}} \tag{3.6}$$

with σ_o being the standard deviation of the observation error and σ_y being the spread of the 41-member ensemble which is defined as:

$$\sigma_Y = \sqrt{\frac{1}{41}\sum_{m=1}^{41}(Y_m - \overline{Y})^2} \tag{3.7}$$

where $\overline{Y}$ is the ensemble mean.

After the presentation of the error metrics that are used for evaluation in this thesis, it should be noted that the assessment of new error metrics for solar irradiance forecasts is an active field of research. The goal is to better account for the variability of solar irradiance (Marquez and Coimbra, 2012; Lohmann, 2018) and so-called "ramp events" where solar irradiance increases or decreases rapidly (Vallance et al., 2017; Abuella and Chowdhury, 2018). Nevertheless, such new metrics are usually targeted for irradiance forecasts of the next minutes up to a

few hours ahead. Since the forecast horizon of interest is between 5 and 40 hours in this thesis, no other than the metrics listed above are used. Especially the use of RMSE and MAE is common in research and in the solar industry for these forecast horizons.

3.8 GHI forecasts from operational models

For different reasons, GHI forecasts from several operational NWP models are examined in chapter 5. As found in chapter 1, there is a lack of studies that evaluate the performance of NWP models in tropical environments. The analyses performed here do not only allow to quantify the impact of satellite DA on GHI forecasts on Reunion Island, but also to quantify the spread of GHI forecast errors from operational NWP models at this tropical island. Comparing the results from the different WRF experiments with operational NWP output reveals the current limits of GHI forecast accuracy. At the same time, such a comparison allows to assess the potential that satellite DA holds for improving tropical GHI forecasts. Moreover, the comparison addresses the first research question raised in chapter 1 ("Do LAMs forecast ground-level solar irradiance more accurately than GCMs on Reunion Island?"). This section gives an overview about the models that are used for comparison with the conducted WRF experiments, and how the irradiance forecasts at a resolution of 15 minutes are obtained.

Table 3.3 lists the operational models that are considered, all of which have a native temporal output resolution of 1 hour. For each model, only the 0000 UTC runs are considered to match the performed WRF experiments. Four GCMs, namely GFS, IFS, ICON (ICOsahedral Nonhydrostatic model), and the LAM AROME, are considered. All GCMs have their own individial data assimilation system and assimilate the different types of atmospheric observations in different ways. The AROME model that Météo-France operates for the SWIO region currently does not use data assimilation. The model uses ICs and LBCs from the IFS model and also ARPEGE for ICs of surface parameters (Météo-France, 2017). Consequently, the WRF experiment that is methodologically the closest to the operational AROME setup is DWNSC-NEST. While AROME performs a dynamical downscaling of IFS forecasts at a convection resolving resolution, WRF performs dynamical downscaling of GFS forecasts in DWNSC-NEST using a nested domain at convection resolving resolution.

To allow a comparison of the output of these models with the WRF output at 15-minute resolution, an interpolation via the clear-sky index is performed to obtain artificial 15-minute output for each model. The clear-sky index k_c is a nondimensional value that isolates the variability of GHI to only that caused by clouds:

$$k_c(t) = \frac{GHI(t)}{GHI_{clear}(t)} \tag{3.8}$$

Table 3.3 – List of NWP models used for comparison with WRF. All models have a native temporal output resolution of one hour. Only the 0000 UTC runs are considered.

Model name	Institution	Type	Grid spacing	IDW radius
GFS	NCEP	GCM	0.25° (≈ 28 km)	160 km
IFS	ECMWF	GCM	0.1° (≈ 11 km)	closest grid box
ICON	DWD	GCM	0.125° (≈ 13 km)	40 km
ARPEGE	Météo-France	GCM	0.5° (≈ 55 km)	160 km
AROME	Météo-France	LAM	0.025° (≈ 2.5 km)	17 km

where $GHI_{clear}(t)$ is the GHI at a given time t under clear-sky conditions, provided by a clear-sky model. k_c is equal to 1 during clear-sky conditions and lower than 1 during cloudy conditions. A k_c larger than one can occur due to the "cloud enhancement effect". This means that a given observed GHI is higher than the clear-sky GHI caused by scattering of solar irradiance by clouds near the observation site, while at the same time the clouds do not obscur the sun.

The average hourly clear-sky index for each model is obtained by:

$$\overline{k_c(1h)} = \frac{\overline{GHI_{model}(1h)}}{\overline{GHI_{clear}(1h)}} \tag{3.9}$$

using the hourly averages of GHI as forecasted by the NWP model $\overline{GHI_{model}(1h)}$ and clear-sky GHI from the clear-sky model $\overline{GHI_{clear}(1h)}$.

Finally, the synthetic GHI forecasts with 15-minute average values are obtained by:

$$\overline{GHI_{model}(15min)} \approx \overline{k_c(1h)} \times \overline{GHI_{clear}(15min)} \tag{3.10}$$

The comparison of cloud and solar irradiance forecasts from different NWP models is not straightforward because of the double penalty problem (section 2.2.2). Addressing this problem, IDW is not only performed in the WRF experiments, but also applied to the output of the operational models listed in this section. The spatial averaging that is performed by IDW is supposed to increase the comparability of the GHI forecasts from the various models that have different output resolutions. An individual IDW radius is defined for each model. One possible approach to define these radii would be to chose the same radius for each model in terms of absolute distance from the site of interest. However, the GHI forecast error of each individual model would not be optimal in this case. This is because averaging over many grid boxes would be applied for the models with the highest resolution, while much less spatial averaging of information would be applied to model output at a much coarser resolution. Therefore, the applied radii are chosen with regard to RMSE and MAE, with the goal of keeping these errors at a minimum. The applied radii for each model were defined in preliminary sensitivity experiments (not shown) with respect to the combined study period (table 3.1).

Table 3.3 lists the IDW radii that are applied for each model. The only model for which the forecasts of the closest grid box perform best during the study period is the IFS model. Thus, IDW is not applied for IFS.

3.9 Conclusion

After the review of existing approaches for satellite DA and the identification of a particularly promising approach in chapter 2, this chapter specifies the configuration of the model, the DA system, and the processing of observations in detail. A number of choices are made and explained that allow to perform experiments. The design of these experiments is explained in this chapter and their evaluation is subject of the chapters 4 and 5. Therefore, this chapter is a crucial link between the findings in chapter 2 and the achievement of the objectives of the thesis.

Chapter 4

The impact of DA cycling

Contents

Summary

This chapter is split into two parts. The first part focuses on an evaluation of the cloud analyses in the southwestern Indian Ocean that are obtained using the applied DA methodology. It is demonstrated that the multi-phase retrieval assimilation approach works and improves the WRF analyses in terms of clouds. Specifically, a comparison with independent radiosonde observations reveals that the mean bias errors of specific humidity and temperature are lower throughout the troposphere in the experiment with DA. The assimilated ice water path retrievals have the largest contribution compared to the supercooled and liquid phase retrievals. An average reduction in RMSE of approximately 0.2 $\mathrm{kg\,m^{-2}}$ *between first guess and analysis is achieved for ice water path. The impact of the assimilated liquid phase retrievals might be increased in the future by defining more accurate observation errors for this phase. The second part of this chapter establishes the link between cloud analysis improvement due to DA and forecasts of solar irradiance. The case of a convective cloud band in the model domain is chosen to demonstrate how the corrected cloud location impacts GHI forecasts for Reunion Island. On the considered day, especially the retrievals from the ice phase influence the location of high clouds in the WRF initial conditions. In the DA-based WRF simulation and in reality, these clouds persist throughout the day over Reunion Island. Since this is not the case in the control experiment, the result is a distinct improvement of solar irradiance forecasts on that day.*

4.1 Introduction

The results that are presented in this chapter are split into two parts. Firstly, an evaluation of the DA cycling is presented to evaluate the implementation of the CWP DA methodology and the improvement of cloud analyses (section 4.2). The purpose of this section is to achieve the second objective of this thesis:

Objective 2 *The improvement of cloud analyses in the southwestern Indian Ocean using limited-area NWP and geostationary satellite DA.*

Secondly, the link between the improved cloud analyses and free forecasts of GHI is investigated in a case study (section 4.3). It is verified whether DA positively influences the free forecasts before a more thorough quantification of this impact in chapter 5.

4.2 Cycling evaluation

As a first step, the RMSE for WP at different altitudes during all cycling periods listed in table 3.1 is calculated and shown in figure 4.1 in which the impact of the three-phased CWP assimilation can be seen. For each phase and altitude, the majority of the available observations (green circles) are assimilated (green asterisks), which indicates that the DART quality check only excludes a reasonable amount of observations and that the defined WP errors (table 3.2) are realistic. Depending on the mean CEP of the different phases, the maximum number of WP observations, approximately 20000 per phase, are localised around certain pressure level bins. These bins are 400 hPa for IWP, 500 hPa for SWP and 850 hPa for LWP. These pressure level bins approximately correspond to the ones found in section 3.3 (figure 3.6 (b)). This is a first indication that the assimilation is working correctly.

The difference between the first guesses (solid lines) and the analyses (dashed lines) is a measure of the impact of the respective phase on the analysis and it can be seen that IWP has the greatest impact and LWP has the lowest impact. This is to be expected since IWP usually exhibits the largest absolute values of WP (figure 3.5). As described in section 3.3, the IWP retrievals may include a contribution of the liquid phase below the ice clouds. This circumstance partly explains why most high absolute WP values occur in the ICE phase and why this phase has most impact. The difference in high absolute WP values between the phases also explains the large difference in RMSE between the different phases. At 400 hPa, RMSE is highest for IWP with averages of 0.43 $\mathrm{kg\,m^{-2}}$ and 0.13 $\mathrm{kg\,m^{-2}}$ in the first guesses and analyses respectively. In comparison, the RMSE for LWP at 850 hPa is reduced from 0.09 $\mathrm{kg\,m^{-2}}$ in the first guesses to 0.08 $\mathrm{kg\,m^{-2}}$ in the analyses.

The evolution of RMSE, MBE and TSPRD for the ensemble mean first guess and analysis is shown in figure 4.2. Cycling period C (table 3.1) is chosen as

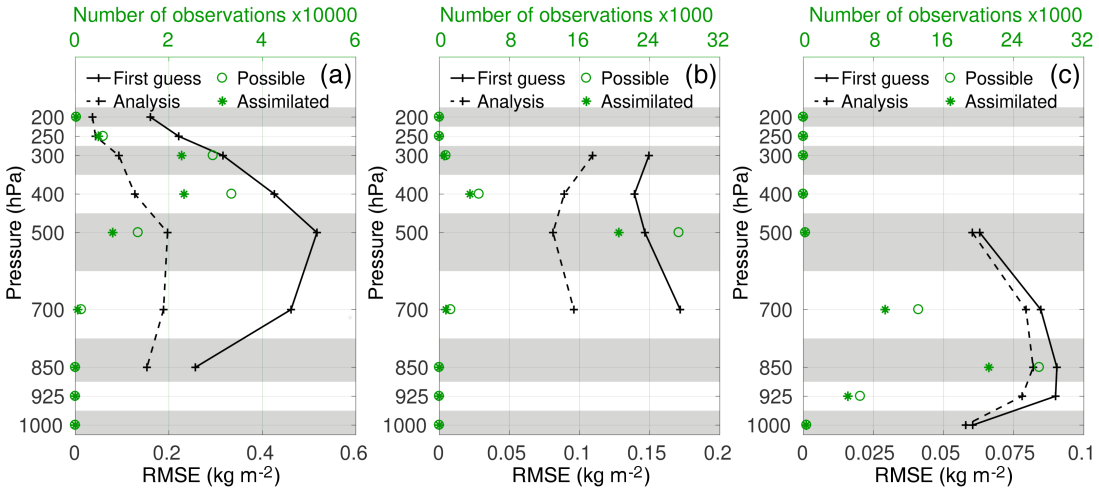

Figure 4.1 – Vertical profiles of the RMSE per bins of CEP for the three phases IWP **(a)**, SWP **(b)** and LWP **(c)** for ensemble mean first guess (solid lines) and analysis (dashed lines) as a mean over all periods listed in table 3.1. The number of possible (circles) and assimilated (asterisks) observations is shown in green.

an example and the pressure levels identified above are chosen for the respective phase.

The classical sawtooth pattern caused by the differences between first guess and analysis is most clearly visible for IWP. This indicates that the retrievals of this phase have the most impact in the filter. While a reduction of RMSE between first guess and analysis is visible at most assimilation times for SWP, this is not the case for LWP. In fact, the smallest impact is achieved for LWP, which is in line with figure 4.1.

TSPRD and RMSE are roughly in phase for IWP, the values generally increase to around 0.3 $\mathrm{kg\,m^{-2}}$ for IWP in the 6 hour first guess forecasts. Relatively high RMSE values of more than 0.6 $\mathrm{kg\,m^{-2}}$ are reached twice for IWP during this period, but these are linked to exceptionally large biases in both cases. In the analyses RMSE and TSPRD are mostly around 0.1 $\mathrm{kg\,m^{-2}}$.

RMSE and TSPRD are less in phase for SWP, which is in line with the expected lower impact of this phase. For LWP, TSPRD never assumes values lower than 0.05 $\mathrm{kg\,m^{-2}}$ which is the defined observation error for the lowest WP observations (table 3.2). This underlines the importance of determining phase-dependent errors that should ideally be less than 0.05 $\mathrm{kg\,m^{-2}}$ for low LWP retrievals. As can be seen in figure 4.2, a clear difference between first guess and analysis becomes visible only at times where TSPRD is larger than 0.05 $\mathrm{kg\,m^{-2}}$. Thus, the relatively large observation error for the smallest observations is likely the reason for the comparably small impact of LWP.

A potential error related improvement could be achieved by considering the errors of CBP and CTP. In order to do so, it must be quantified somehow in

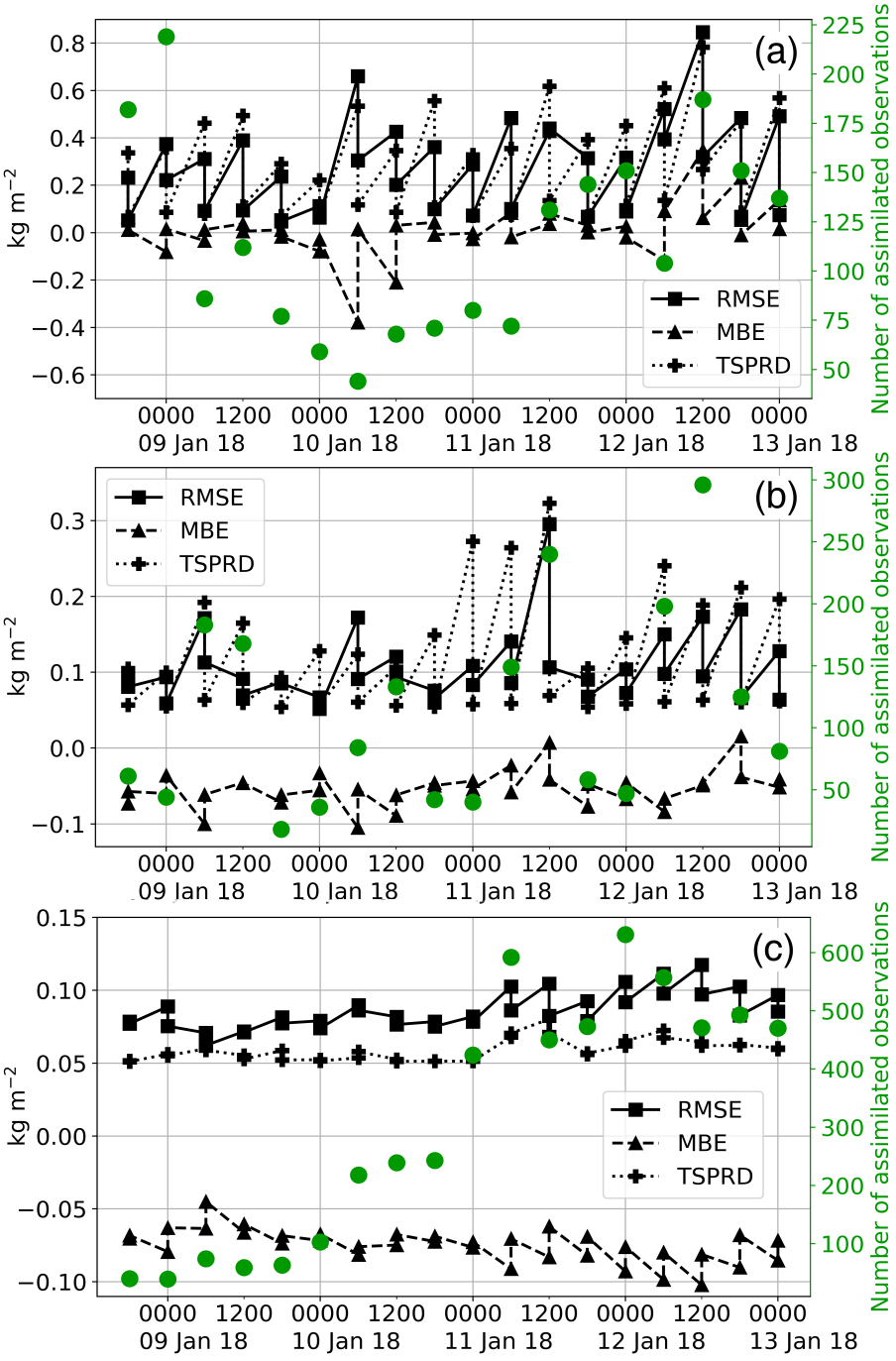

Figure 4.2 – Temporal evolution of ensemble mean first guess and analysis for the three phases IWP at 400 hPa **(a)**, SWP at 500 hPa **(b)** and LWP at 850 hPa **(c)** for cycling period C (table 3.1). The RMSE (rectangles and solid lines), MBE (triangles and dashed lines) and TSPRD (pluses and dotted lines) are shown. The saw tooth pattern observed is a common feature of such plots in DA. The number of assimilated observations per assimilation time is represented by the green dots.

how far the errors of CTP and CBP affect the error of the final WP derived from the model. In line with an improved definition of LWP retrieval errors, the lower threshold of 0.04 $\mathrm{kg\,m^{-2}}$, below which WP retrievals are not considered, may be optimised in sensitivity experiments.

The number of assimilated observations may be very different than the number of available observations due to quality control within DART, as can be seen in figure 4.1. The example of SWP in figure 4.2 shows that the number of assimilated observations is not necessarily correlated with an improvement in terms of RMSE. For example, on the 12th of January the number of assimilated observations fluctuates between 80 and 300 but the RMSE remains relatively stable. For all three phases, the number of assimilated observations per assimilation time varies heavily from zero to a few hundred observations depending on the time of day.

The MBE for IWP fluctuates around zero with a positive correction in each analysis. For SWP and LWP there is a continuously negative MBE, mostly between -0.1 $\mathrm{kg\,m^{-2}}$ and -0.05 $\mathrm{kg\,m^{-2}}$. This indicates that WRF underestimates clouds in the middle and lower troposphere. DA corrects for MBE for all three phases but is far from achieving MBEs close to zero for SWP and LWP.

Figures 4.1 and 4.2 show evaluations of DA experiments as compared to the assimilated observations and therefore demonstrate the ability of the DA cycling to constrain the WRF simulations. Although this can be used to assess the performance of the assimilation itself, this cannot act as an exhaustive validation as no independent observations are used.

Consequently, an evaluation of the MBE for temperature and specific humidity using independent radiosonde measurements is shown in figure 4.3. All 43 radiosoundings at Gillot-Aeroport during the complete study period (table 3.1) are considered. The total number of evaluated observations per pressure bin are shown in green and reach up to 80 at around 400 hPa. The lack of radiosonde stations in the model domain and the fact that only one station in the centre of the domain is considered is compensated, to some extent, by the duration of the study period that includes various cloud and weather situations.

The ensemble mean first guess (solid lines) and analysis (dashed line) are shown for both experiments CTRL (orange line) and CWPDA (black lines) with first guess and analysis being the same for CTRL as no DA is performed. For both experiments an overall negative MBE for specific humidity and a positive MBE for temperature are visible throughout the troposphere. The fact that the MBE for specific humidity is largest in the lower troposphere, with more than 1 $\mathrm{g\,kg^{-1}}$, confirms that WRF tends to underestimate low clouds. At the same time, the difference between the two experiments for specific humidity is the largest in the lower troposphere around 850 hPa. This shows that the assimilation corrects for the lack of humidity in the analyses to some extent and thus has the effect of a bias correction.

Although figure 4.1 and figure 4.2 indicate the largest impact of the DA is in the higher troposphere from IWP observations, the effect on bias regarding radiosonde

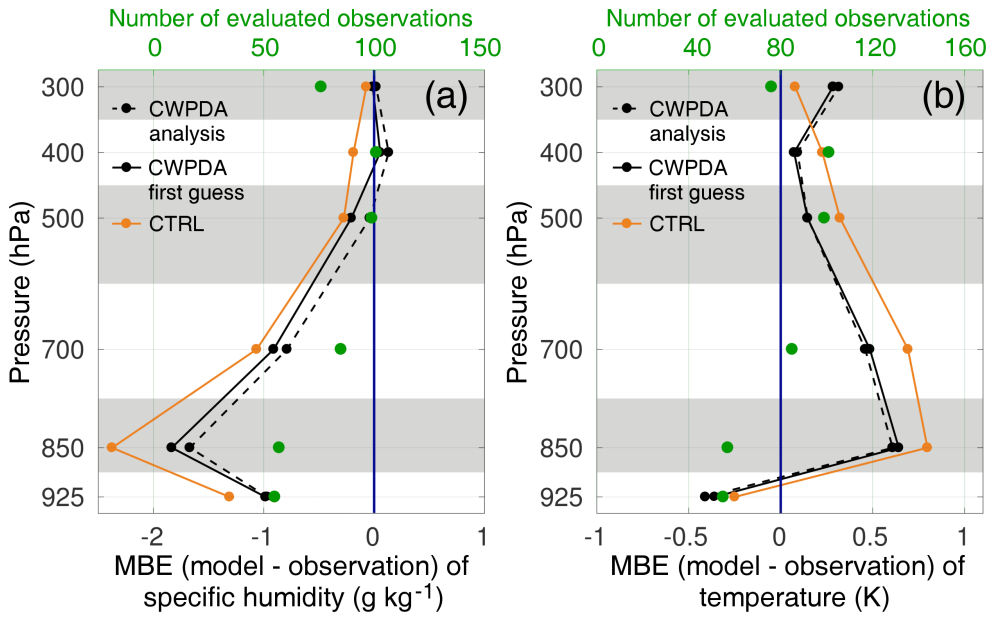

Figure 4.3 – Vertical profiles of the MBE per bins of pressure for specific humidity **(a)** and temperature **(b)**, for the two experiments CWPDA (black) and CTRL (orange), with respect to independent radiosonde observations. The solid lines show the ensemble mean first guesses. The dashed line shows the analyses of CWPDA. A dashed line does not exist for CTRL since prior and posterior are identical. The number of evaluated observations per pressure bin is shown in green. All cycling periods listed in table 3.1 including 43 radiosoundings at 1200 UTC at Gillot-Aeroport are considered.

specific humidity is smaller at these altitudes than in the low troposphere. This may be explained by the fact that absolute values of specific humidity are generally largest in the low troposphere. Moreover, the evaluated radio soundings are valid only for the centre of the domain while figure 4.1 and figure 4.2 include information about the whole model domain. Furthermore, local thermal circulations likely cause more low clouds at this coastal location than in the rest of the domain which lacks other land masses.

The difference between CWPDA prior and posterior is more distinct for specific humidity than for temperature, leading to an improvement of humidity bias in the analyses compared to the first guesses. As the objective here is to improve cloud prediction, the improvement in humidity, a field strongly related to clouds, is more significant than an improvement in temperature. It is however favourable that the CWP DA does not have a negative impact on the temperature profile.

Regarding the DA configuration, a number of parameters such as the covariance localisation radius are known to largely impact the DA outcome (Otkin, 2012a; Ying et al., 2018). Concerning the gridded multi-phase SatCORPS retrievals used in this study, the sensitivity of the assimilation to the localisation radius might be assessed in detail in future work. This is especially true for DA experiments at

convective scale resolutions that have yet to be performed.

Moreover, the ensemble spread could be modulated in various ways by adjusting the WRF ensemble generation method. For example, multiple sets of physics options could be applied in the ensemble members, an optimal compromise between ensemble size and spread could be determined, the method for WRF ensemble member generation from the 21-member GEFS ensemble ICs and LBCs might be optimised, and different settings for adaptive inflation could be tested.

In summary, the operational correctness of the DA methodology is confirmed. The largest impact is found for the ice phase retrievals, and the lowest impact for the liquid phase retrievals. Independent radiosoundings indicate a humidity bias reduction between first guesses and analyses. Any improvement of the utilised cloud products is expected to positively influence the DA outcome. Future cloud products are aiming to better account for vertical heterogeneity and thus produce multi-phase CWP estimates that are closer to reality and more similar to what NWP models produce regarding deep overlapping cloud systems. Moreover, a precise definition of phase-dependent errors for the SatCORPS Meteosat-8 products does not yet exist. Once this information is obtained, the performance of the applied system using these observation errors can be assessed.

4.3 A case study

Having demonstrated the correct implementation of the DA methodology, which shows a generally positive impact on the cloud analyses, this section focuses on a case study of one particular day. The influence of the applied DA approach on the cloud analysis and the subsequent free forecast with respect to solar irradiance is analysed.

On 12 January 2018 the large scale flow in the study region was governed by an anticyclone south of Madagascar and two depressions located at the northern boundary of the WRF domain as indicated in synoptic surface analyses (figure 4.4). The first depression was located approximately 700 km north of Reunion Island, the second one approximately 1500 km north-east of Reunion Island (figure 4.4 (a)). This situation led to a north-westerly flow throughout the model domain and the creation of a convergence zone extending diagonally across the model domain from the north-west to the south-east. This convergence zone is indicated in figure 4.4 (b) off the east coast of Madacascar.

Figure 4.5 shows a VIS image taken by Terra/MODIS at 0630 UTC. The band of deep convective clouds that is associated with the convergence zone reaches from the north-east of Madagascar to Reunion Island. Such large convective cloud systems associated with low pressure systems north of Reunion Island typically produce the lowest GHI values during austral summer (Badosa et al., 2015). Hence, the day considered here is one of the days with the lowest observed day-time GHI values throughout the combined study period listed in table 3.1 and therefore most

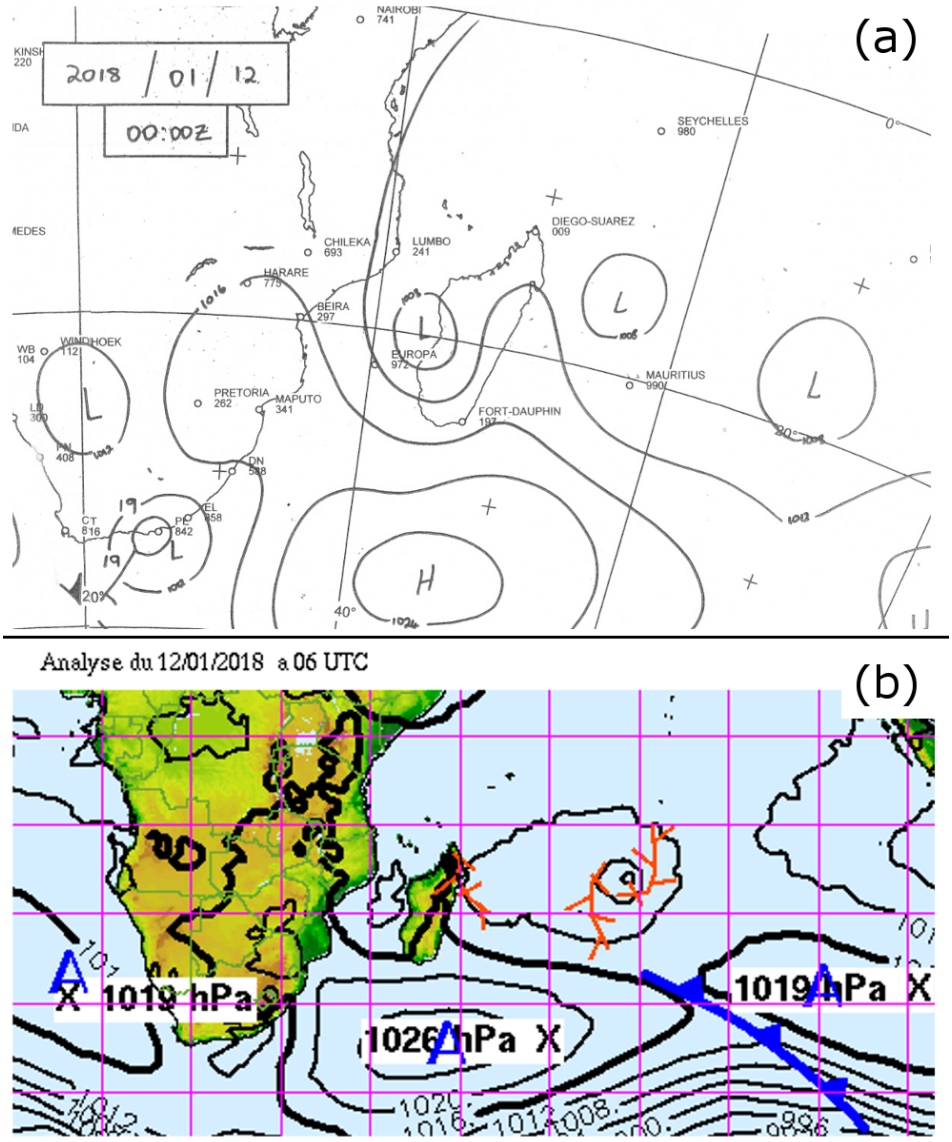

Figure 4.4 – Synoptic surface analyses for 12 January 2018 published for 0000 UTC by the South African Weather Service (a) and for 0600 UTC by Météo-France.

distinctly shows the impact of the DA on the GHI forecast.

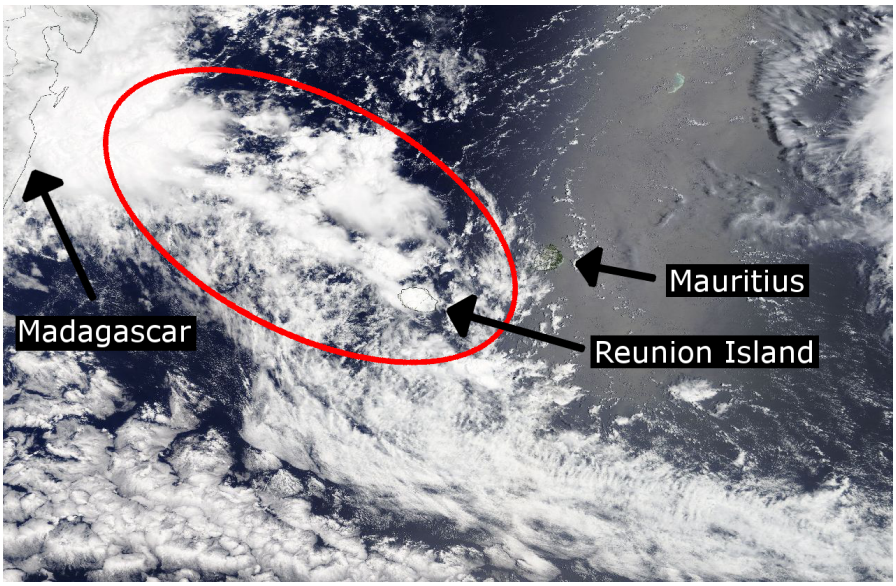

Figure 4.5 – Terra/MODIS VIS image of the study area taken 12 January 2018 at 0630 UTC. The red ellipse indicates the location of a band of deep convective clouds reaching from the north-east of Madagascar to Reunion Island in the centre of the image. Source: gibs.earthdata.nasa.gov.

The SatCORPS WP gridded retrievals at 0000 UTC, the time of the free forecast analysis, are shown in the left part of figure 4.6. The clouds induced by the convergence zone are visible especially in the ice and liquid phase (a, e), with WP values exceeding 0.3 $\mathrm{kg\,m^{-2}}$ in some areas. The highest values in the vicinity of Reunion Island can be observed in the ice phase indicating high clouds. These ice clouds persist during the day (not shown) and contribute largely to the observed low solar irradiance on Reunion Island throughout the day. High values of WP are also present for the supercooled phase in the vicinity of Reunion Island, but the total amount of retrievals is much lower than that of the ice and liquid phase.

The right part of figure 4.6 shows observation space diagnostics of the WP difference, in each phase, between the two experiments (CWPDA minus CTRL) in terms of the posterior ensemble mean WP. More cloud water is present in all phases over the convergence zone in CWPDA when compared with the CTRL experiment. A visual comparison shows that the locations of additional WP in CWPDA correspond well with the locations of the highest values in the retrieval maps. In the ice phase, distinct gradients between areas of increased and decreased WP are visible that indicate corrections to the cloud location resulting from the DA. Maximum and minimum values are -0.9 and 1.9 $\mathrm{kg\,m^{-2}}$ for IWP (b), -0.2 and 0.19 $\mathrm{kg\,m^{-2}}$ for SWP (d) and -0.06 and 0.19 $\mathrm{kg\,m^{-2}}$ for LWP (f).

The effect of these corrections on the free forecast experiment in terms of cloud fraction is shown in figure 4.7. The ice clouds induced by the convergence

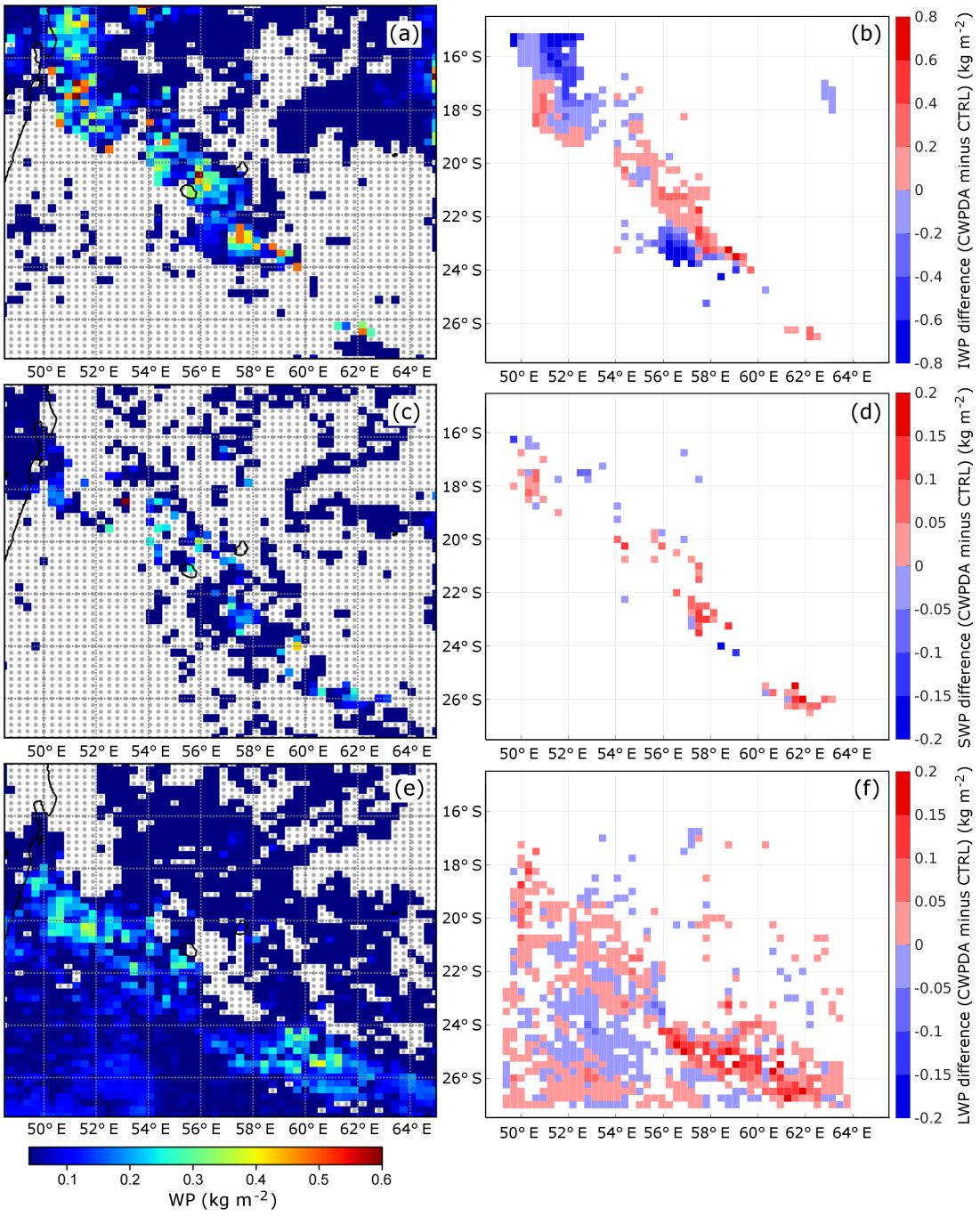

Figure 4.6 – Maps of SatCORPS Meteosat-8 gridded CWP retrievals for the three phases IWP **(a)**, SWP **(c)** and LWP **(e)**. Missing observations are shown in grey. The right side shows the difference of the posterior ensemble mean between the two cycling experiments (CWPDA minus CTRL) for the three phases, i.e. IWP_{diff} **(b)**, SWP_{diff} **(d)** and LWP_{diff} **(f)**. Red indicates that CWPDA generates higher WP values than CTRL and blue indicates that CWPDA generates lower values than CTRL. Only locations where the retrievals were successfully assimilated in CWPDA are shown in the right plots. All plots show 12 January 2018, 0000 UTC.

zone are visible in both CTRL-FF and CWPDA-FF and in both cases, clouds are located above Reunion Island 15 minutes after the analysis time ((a) and (b)). A north-eastward relocation of the clouds around Reunion Island can be seen for CWPDA-FF. As the clouds move eastward over the course of the day, this has the effect of causing high clouds to persist over Reunion Island in CWPDA-FF ((d) and (f)). At the same time, high clouds are further west in CTRL-FF ((c) and (e)) leaving the model levels around 300 hPa cloud-free above Reunion at 0800 UTC (corresponding to noon local time). In CWPDA-FF, clouds are still present at 300 hPa over Reunion Island at 0800 UTC leading to a reduction of GHI as shown in the following.

While figure 4.7 only shows the cloud fraction at 300 hPa, the vertical distribution of cloud fraction is shown in figure 4.8. The figure shows cross section plots of cloud fraction along 21.1° S and over Reunion Island. Cloud fraction is higher at around 300 to 400 hPa in CWPDA-FF than in CTRL-FF at the beginning of the forecast (a, b). At a lead time of 8 hours (c, d) it is still the high clouds that contribute most to the total cloud cover over Reunion. Nevertheless, the horizontal and vertical extent of the high level band of clouds is less distinct in CWPDA-FF than in CTRL-FF at that time. Still, CWPDA-FF performs better in terms of GHI forecasts for this day, since there are almost no clouds present in the vertical column above Reunion Island in CTRL-FF at 0800 UTC.

A large variability of GHI is observed during the day for all pyranometer sites as well as between the different sites (figure 4.9). GHI values are overall low and mostly below 400 $\mathrm{W\,m^{-2}}$ at all sites, this is mainly caused by the deep convective clouds during that day as can deduced from figure 4.5.

In terms of GHI, a distinct difference is visible between CTRL-FF and CWPDA-FF as a consequence of the DA and the fact that high clouds persist over Reunion Island in CWPDA-FF. Although the forecasted GHI is largely reduced in CWPDA-FF, the values around noon are still too high compared to the observations for most sites. One potential reason for this might be the influence of the applied IDW post-processing in this given case. Higher values of GHI in the vicinity of Reunion Island due to the lack of clouds are included in the GHI forecasts for the 12 sites to some extent. Further improvements might be found by analysing the interplay between DA, post-processing and the configuration of WRF in terms the choice of parameterisation schemes. In this thesis, the focus is set on the influence of DA only which is clearly visible in this example. The effect of different grid spacings is evaluated in chapter 5.

This comparison between forecasts and observations of GHI also illustrates the difficulty of forecasting ramp events. The chosen grid spacing of 12 km and IDW post-processing results in a smoothing of ramps in the WRF forecasts. This is why the widely used metrics RMSE and MAE are suitable for a quantification of the DA impact. If one wants to study the impact of DA on ramp forecasts specifically, experiments at convection resolving resolutions, a focus on parameterisation schemes, and specific ramp metrics and post-processing methods are required.

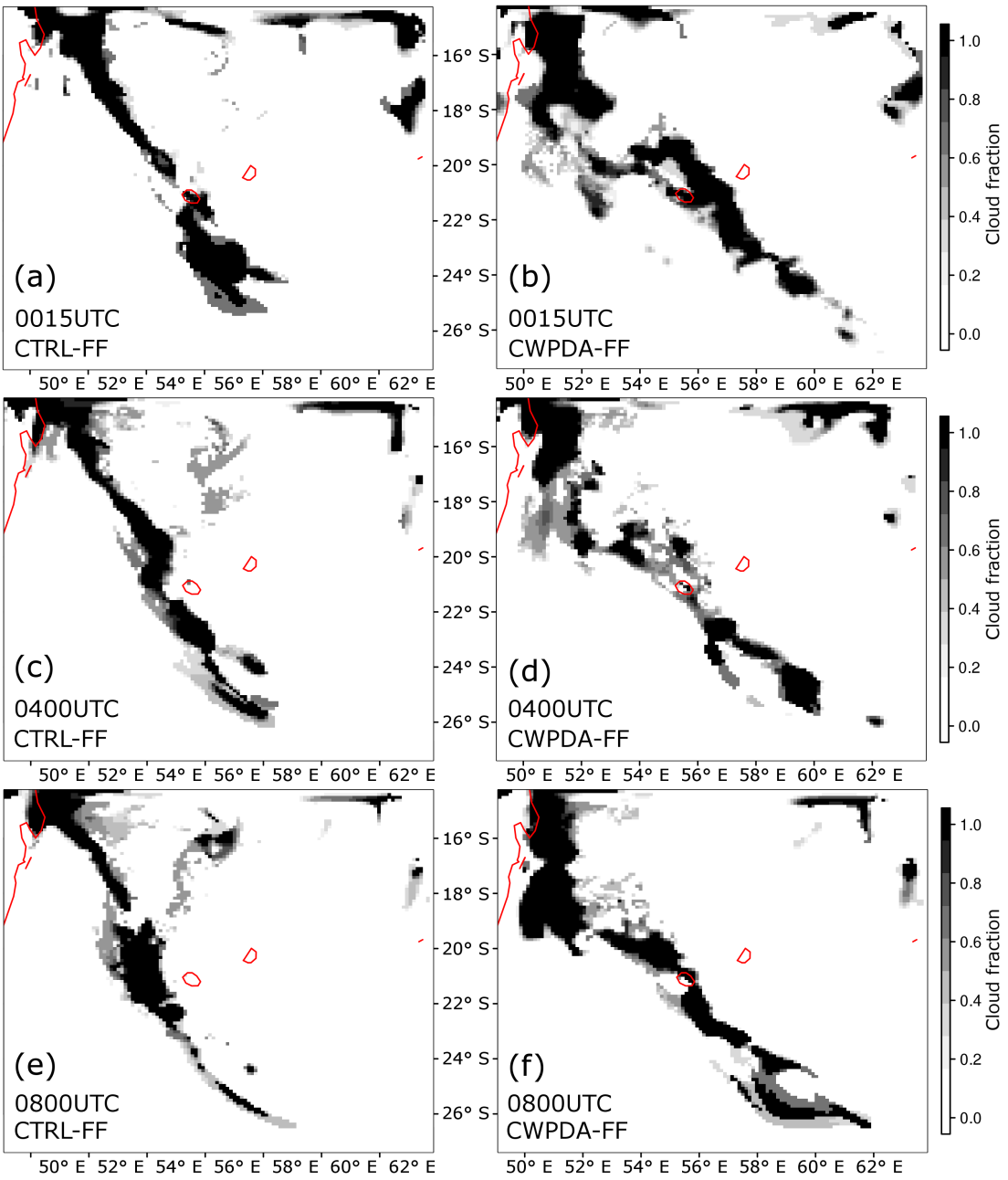

Figure 4.7 – WRF forecasts of cloud fraction at 300 hPa from the CTRL-FF **(a, c, e)** and CWPDA-FF **(b, d, f)** experiments on 12 January 2018 at 0015 UTC **(a, b)**, 0400 UTC **(c, d)** and 0800 UTC **(e, f)**. The initial conditions originate from the experiments CTRL and CWPDA respectively. Coastal lines are shown in red.

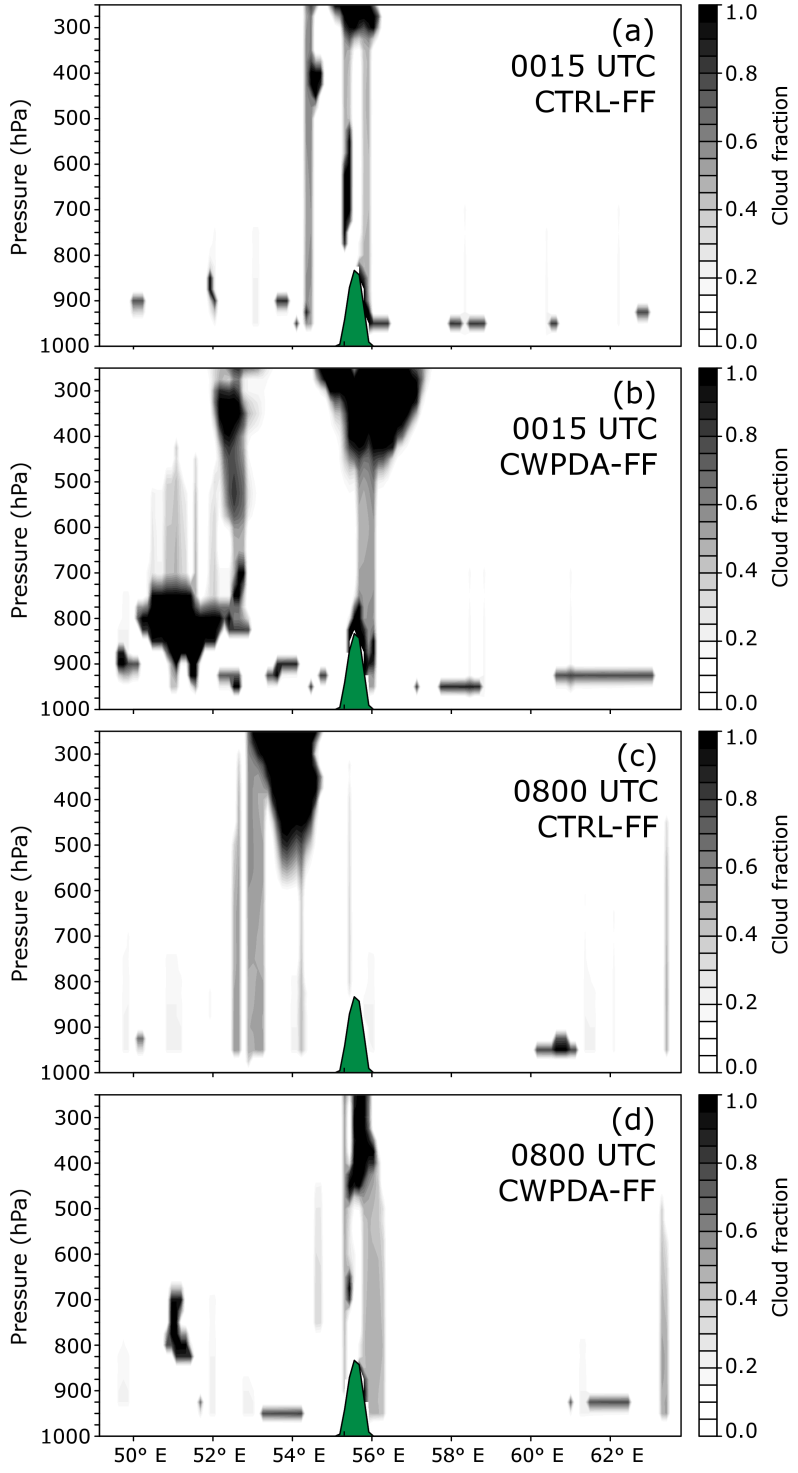

Figure 4.8 – Latitudinal cross sections along 21.1° S of WRF cloud fraction from the CTRL-FF **(a, c)** and CWPDA-FF **(b, d)** experiments on 12 January 2018 at 0015 UTC **(a, b)** and 0800 UTC **(c, d)**. The representation of Reunion Island within WRF is shown in green.

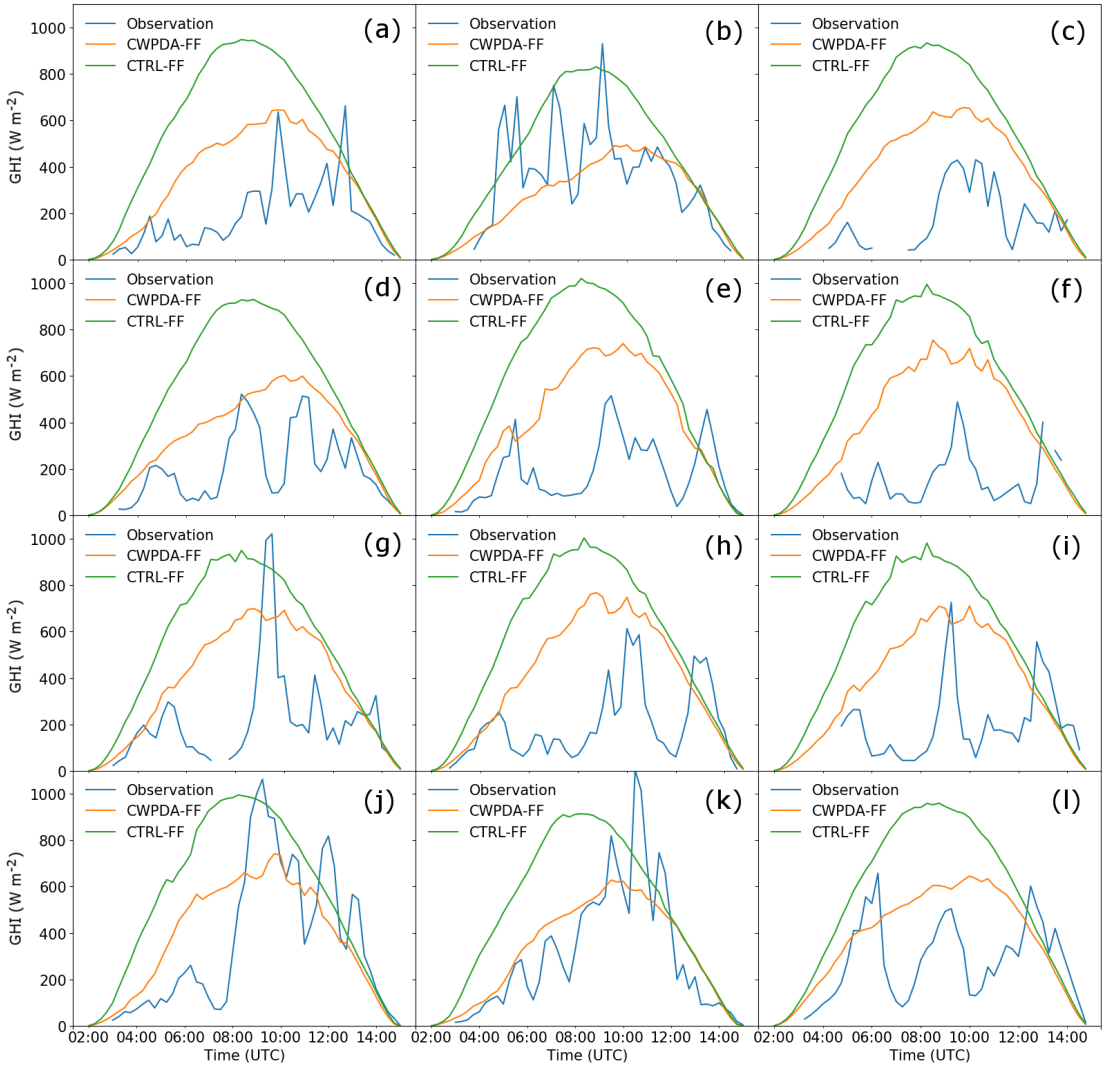

Figure 4.9 – GHI on Reunion Island on 12 January 2018 as observed (blue), and forecasted by CWPDA-FF (orange) and CTRL-FF (green) with IDW post-processing for the sites Plaine des Cafres **(a)**, Gros Piron Sainte-Rose **(b)**, Cilaos **(c)**, Bellevue Bras-Panon **(d)**, Le Port **(e)**, Colimacons **(f)**, Piton-Maido **(g)**, Pointe des Trois-Bassins **(h)**, Petite-France **(i)**, Pierrefonds-Aéroport **(j)**, Le Baril **(k)**, Gillot-Aéroport **(l)**.

4.4 Conclusion

Previous studies have shown that the assimilation of geostationary CWP retrievals with WRF-DART leads to improved short-term GHI forecasts in mid-latitudes (Jones et al., 2013b, 2015). However, the performance under tropical conditions has been unknown so far. It is demonstrated in this chapter that the applied DA methodology improves the WRF analyses in terms of clouds in the SWIO. Moreover, the link between the improved cloud analyses and their impact on forecasts of GHI is examined.

The assimilated retrievals of IWP, SWP and LWP have most impact at pressure levels of 400 hPa, 500 hPa and 850 hPa respectively. The largest contribution comes from the IWP retrievals with an average reduction in RMSE of approximately 0.2 $\mathrm{kg\,m^{-2}}$ between first guess and analysis. LWP has the lowest impact which can partly be explained by the large observation errors for small observations. It is hypothesised that a more sophisticated definition and handling of WP retrieval errors would further improve the analyses.

The evaluation using 43 independent radiosoundings shows a reduced bias in specific humidity for the experiment with CWP DA, especially in the mid-troposphere. A further reduction of bias between the first guesses and analyses supports the case that the applied DA method leads to more realistic WRF humidity profiles and consequently improves the 'cloud analyses'.

The case study shows that the correction of cloud location in the analysis has a distinct impact on free forecasts of GHI on Reunion Island. In the studied case, the increased amount of high level clouds leads to a marked reduction of GHI on Reunion Island. This corresponds better to the observed values at all sites on the considered day. The long-term quantification of this impact is addressed in the following chapter.

Chapter 5

Irradiance forecast evaluation

Contents

Summary

After the demonstration of cloud analysis improvement due to cloud water path assimilation in the previous chapter, this chapter focuses on a detailed analysis of solar irradiance forecasts. All performed experiments are evaluated for a total of 44 days in austral summer 2017/2018 using GHI observations of 12 pyranometers on Reunion Island. These evaluations performed in this chapter allow to pursue the objectives and answer the research questions that are raised in chapter 1. Therefore, various aspects are examined in the different sections of this chapter. Firstly, the reduction of GHI forecast errors at all sites as a consequence of CWP DA is quantified for the coarse domain experiments. Secondly, the duration of the impact of DA is examined. A clear improvement of intraday forecasts, and a less pronounced improvement of day-ahead forecasts is found. Next, the difference between a one-way nested domain using initial conditions from cycling, and two-way nesting in a pure dynamical downscaling setup, are evaluated. A clear benefit from nesting, at least for the first forecasted day, can be observed. Lastly, the GHI forecast errors that are obtained with the different WRF experiments are put in relation to the GHI forecast error range of operational NWP models. In summary, using LAMs as well as satellite DA is clearly beneficial for short-term solar irradiance forecasting on Reunion Island.

5.1 Introduction

It is found in the previous chapter that cloud-property DA has a considerable impact on analyses of cloud-related parameters such as CWP, specific humidity and forecasts of solar irradiance in the SWIO. Nevertheless, as in many other proofs of concept for DA methods, only one weather situation has been analysed so far in terms of solar irradiance. Evaluations over a period of more than a few days are rare in peer-reviewed literature (see chapter 2). Therefore, an evaluation of the free forecasts for a total of 44 days (table 3.1) is performed in this chapter in order to quantify the impact of DA on GHI forecasts more meaningfully. Consequently, this chapter addresses the third objective of this thesis:

Objective 3 *The quantification of the impact of the applied DA approach on short-term (5 to 40 hours) solar irradiance forecasts on Reunion Island.*

The analysis of the free forecasts is split into different parts to address particular aspects in a structured manner. Firstly, the forecasts of CTRL-FF and CWPDA-FF at 12 km grid spacing are evaluated for the first forecasted day in section 5.2. As the forecasts are initiated at 0000 UTC, the first forecasted day is also referred to as "intraday". Secondly, the second forecasted day, the "day ahead" is analysed in section 5.3. This differentiation allows to identify up to which lead time the impact of DA is noticeable in the free forecasts. Next, the GHI forecasts of the one-way nested domain (CTRL-FF-NEST and CWPDA-FF-NEST) are evaluated in section 5.4. This permits to analyse the effects of nesting and different resolutions, keeping in mind that DA is only performed for the coarser domain. Following this analysis, a comparison between the dynamical downscaling experiments (DWNSC and DWNSC-NEST) and the cyclic free forecast experiments is performed in section 5.5. After these evaluations of forecasts with and without DA, as well as with and without nesting, section 5.6 puts the WRF forecast errors in relation to those of the operational models that are listed in section 3.8. This allows to assess the benefit of using LAMs rather than GCMs for GHI forecasting, and to estimate the potential of satellite DA independently of the applied LAM.

In the analysis of the GHI forecast errors it is important to distinguish between four "dimensions": the error metric, the site, the forecast lead time, and the experiment. The goal of this chapter is to analyse the different WRF experiments in terms of the different metrics. Therefore, to keep the analysis comprehensible, a choice has to be made between the sites and the forecast lead times. That means that at least one dimension needs to be reduced for a comprehensible and compact evaluation. Consequently, either one value per site as an average over all lead times, or one value per lead time as an average over all sites is considered. Therefore, most of the figures in this chapter represent either a mean over all forecast lead times of a given day (intraday or day-ahead), or a mean over all sites per lead time. The tables in this chapter contain averages over both the sites and

the forecast lead times (either intraday or day ahead). For some of the sites, more GHI observations are available than for other sites (see appendix A). Therefore, if the GHI observations are not available for all 12 sites at a given moment, none of the sites are considered in the evaluation at that moment. If this was not done, the calculated WRF forecast errors for the different sites would not be strictly comparable since different weather situations would be compared. This would be less of a problem if the sites were spatially distributed on a surface larger than Reunion Island, e.g. the extent of the WRF domain. In that case, the large scale weather situation would not be identical for the different sites.

5.2 Coarse domain forecasts

Figure 5.1 shows the site-specific performance of intraday GHI forecasts from CTRL-FF and CWPDA-FF in terms of RMSE, MAE, MBE and correlation. One value per site and metric is computed as an average over all lead times of the first forecasted day.

Before investigating the difference between the two experiments, the spread between the sites for all metrics can be explained by the location of the sites and the local meteorological conditions. The six sites with the best performance in terms of RMSE (between 230 and 280 $\mathrm{W\,m^{-2}}$) and MAE (between 180 and 220 $\mathrm{W\,m^{-2}}$) are Gillot-Aeroport, Pierrefonds-Aeroport, Pointe des Trois-Bassins, Piton Sainte-Rose, Le Port and Le Baril. All of these sites are located on the coast line of Reunion (figure 3.9), where the influence of clouds that are induced by orographic uplift and thermal circulations caused by the mountains is lowest.

The two sites with the highest forecast errors in terms of RMSE, MAE and correlation are Colimacons and Petite-France. These sites are both located in the west of Reunion Island at 800 m and 1200 m respectively. These sites are typically in the lee of the trade winds at altitudes where thermally driven convective clouds often form. This leads to lower GHI values (Badosa et al., 2013) and produces the most complex solar irradiance conditions (Bessafi et al., 2018) compared to the other sites. This circumstance also explains the high positive MBE for these two sites.

An improvement of GHI forecasts between CTRL-FF and CWPDA-FF is visible for almost all sites in terms of RMSE, MAE and correlation. On average across all sites, RMSE improves by 11 $\mathrm{W\,m^{-2}}$ (4 %), MAE by 6 $\mathrm{W\,m^{-2}}$ (3 %) and correlation by 0.03. The only exception to this is the site at Le Port where the RMSE is degraded by 1 $\mathrm{W\,m^{-2}}$ and MAE by 2 $\mathrm{W\,m^{-2}}$. In terms of RMSE and MAE, there is less improvement at sites for which GHI is predicted most accurately (Gillot-Aeroport and Pierrefonds-Aeroport). This may be explained in the same way as the large improvement at the sites with the least accuracy: As found in the previous chapter, DA leads to both a better representation of cloud location, and generally increased lower tropospheric moisture. Both of these ef-

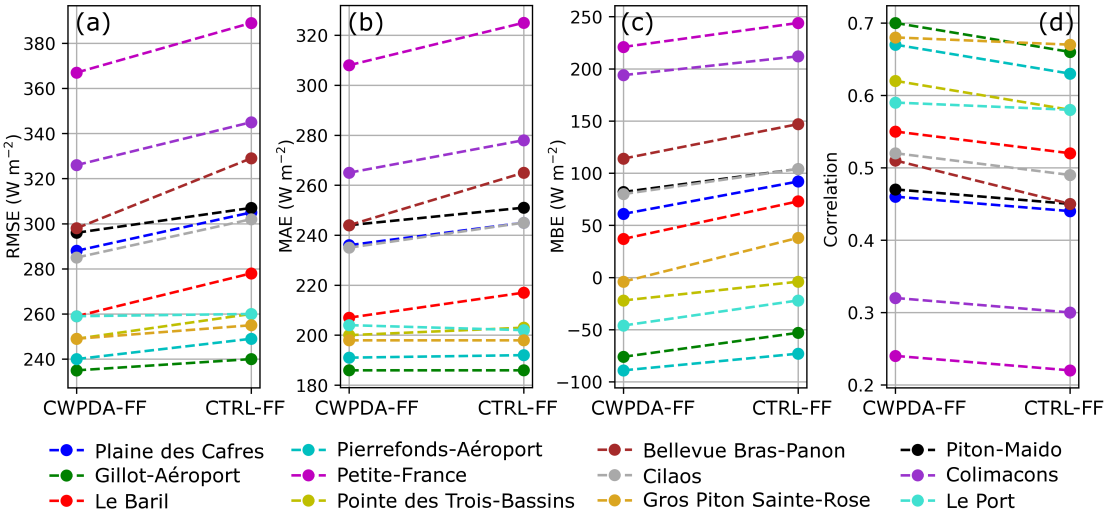

Figure 5.1 – WRF intraday irradiance forecast performance at each site in terms of RMSE **(a)**, MAE **(b)**, MBE **(c)** and correlation **(d)**. The difference between the experiments CTRL-FF and CWPDA-FF is shown for each metric. The values represent averages over the entire first forecasted day and IDW is applied to the GHI forecasts. Detailed information about the study period and the post processing is given in chapter 3.

fects have an impact on the sites with the least accuracy. Being located far from mountain slopes, thermally induced convective clouds are rarer at Gillot-Aeroport and Pierrefonds-Aeroport. The effect of low level clouds at the mountain slopes is thus of less consequence here, compared to improved large-scale cloud system locations.

A positive bias can be seen for most sites, which confirms that WRF tends to overestimate GHI on Reunion Island during austral summer time with pronounced convective activity. There is a shift to lower values of MBE between CTRL-FF and CWPDA-FF with approximately the same amplitude for all sites. This illustrates that CWPDA-FF generally simulates more clouds than CTRL-FF. It also means that for sites with a negative MBE, typically the ones that are not located in the mountains, there is a degradation towards more negative values of MBE. The general tendency in terms of MBE is that it is negative for sites at the coast line and positive for sites located in the mountains (figure 5.1 (c)). In other words, WRF tends to overestimate clouds at the coast line and underestimate clouds in the mountains. This shows that the spatial distribution of the chosen sites must be kept in mind, especially when evaluating averages of MBE over all sites.

Another visualisation of the forecast error than the one in figure 5.1 is necessary to evaluate the DA impact depending on the forecast lead time. The mean RMSE over all sites for each forecast lead time is shown in figure 5.2. Since the overall picture is very similar for MAE, as can be deduced from figure 5.1, only RMSE is shown in figure 5.2.

As explained in section 5.1, it is taken into account that GHI observations are

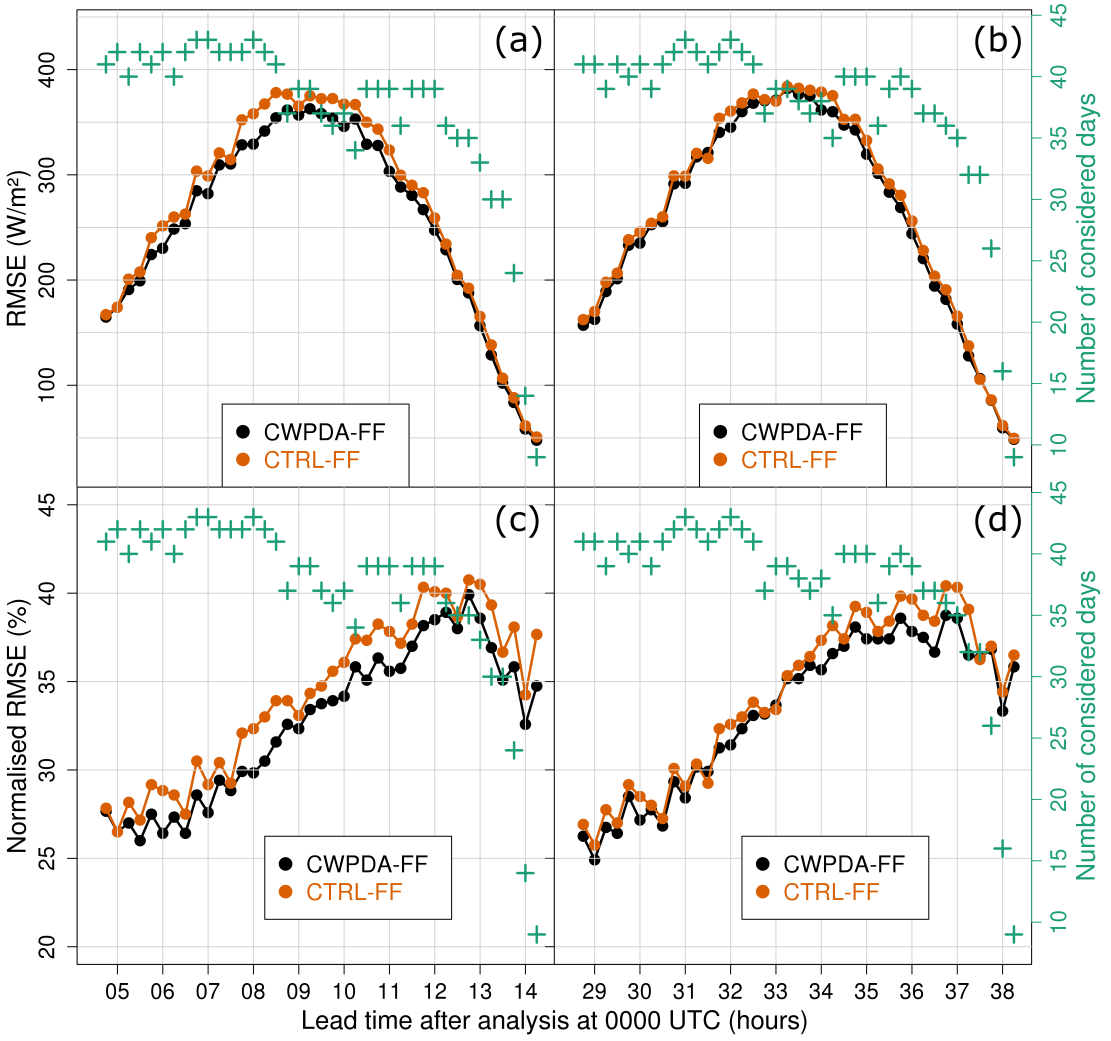

Figure 5.2 – Absolute **(a, b)** and clear-sky normalised **(c, d)** RMSE of the WRF solar irradiance forecasts per lead time as a mean over the 12 considered sites on Reunion Island for all 44 free forecast dates listed in table 3.1. The respective values for the two experiments CTRL-FF (orange) and CWPDA-FF (black) are shown for the first forecasted day **(a, c)** and the second forecasted day **(b, d)**. The number of considered days per lead time (green crosses) varies since a given lead time of a given day is considered only when observations are available for all 12 sites. Local time is UTC-4.

not always available for all 12 sites for a given lead time and day. Consequently, the number of considered days per lead time shown in the figure is the number of days for which observations are available for all 12 sites. These are the days that have been considered in the calculation of RMSE for a given lead time. The first lead time is no earlier than 5 hours (0500 UTC or 9 am local time) since the observations in the morning did not pass the quality control for several stations, which is often due to shadowing at low solar zenith angles, mainly caused by the mountains (see appendix A). As the number of considered days decreases rapidly

at the end of the day, the displayed values for lead times above 13 hours, or 37 hours respectively, are less significant.

Both the absolute (a, b) and the clear-sky normalised RMSE (c, d) are shown in figure 5.2. The representation of absolute RMSE does not correct for the diurnal cycle of GHI, which leads to the characteristic curve. It does however allow the quantification of the absolute difference in RMSE between CTRL-FF and CWPDA-FF. This difference reaches up to 60 $\mathrm{W\,m^{-2}}$ at 0800 UTC (noon local time) for the first forecasted day. The free forecasts that are initialised from CWPDA have a lower RMSE than CTRL-FF throughout the entire first forecasted day. The difference between intraday and day ahead is subject of the next section.

The normalisation with the clear-sky irradiance removes the diurnal cycle. As can be expected, the normalised RMSE increases with increasing lead time for both experiments. The fluctuation of the lines in the normalised lead-time dependent RMSE representation decreases with an increasing number of considered days. This is especially visible at the end of the day (e.g. lead times 13 and 14 hours), where the number of considered days decreases distinctly. For the other lead times, the fluctuation is at an acceptable level, which means that the number of 44 studied days may be considered as sufficient to draw reliable conclusions. The maximum intraday absolute difference of 60 $\mathrm{W\,m^{-2}}$ between CTRL-FF and CWPDA-FF translates to approximately 2 % of normalised RMSE (figure 5.2 (c)).

Table 5.1 shows one value per experiment, forecasted day, and error metric as a mean over the complete study period and the 12 considered sites. Thus, for the intraday and the coarse domain forecasts (CTRL-FF and CWPDA-FF), the values for each respective metric correspond to the mean values of what is shown in figure 5.1. This allows a quantification of the error reduction between CTRL-FF and CWPDA-FF. For the intraday, the application of CWP DA leads to a reduction of 8 $\mathrm{W\,m^{-2}}$ in RMSE, 5 $\mathrm{W\,m^{-2}}$ in MAE, and 25 $\mathrm{W\,m^{-2}}$ in MBE. Correlation improves marginally from 0.51 to 0.52.

5.3 Intraday and day-ahead impact

While (a) and (c) in figure 5.2 show the intraday RMSE, the day ahead is shown on the right side (b, d). The lead times of 8 hours and 32 hours correspond to noon local time. A slight difference is visible between the intraday and the day ahead regarding the number of considered days. This is due to the fact that the considered period is different by two days. For the intraday, the first and last considered dates are 10 December 2017 and 1 March 2018, respectively (table 3.1). For the day ahead, these dates are 11 December 2017 and 2 March 2018.

In general, NWP forecast errors increase with increasing forecast lead time. A comparison of (c) and (d) in figure 5.2 however does not show a clearly visible increase of nRMSE for CTRL-FF between the first and the second forecasted day. In both cases, there is a nRMSE of 25-30% in the morning and 35-40% in the

Table 5.1 – WRF GHI forecast accuracy in terms of RMSE, MAE, MBE, and correlation as a mean over the 12 considered sites and the considered period. The results for the experiments CTRL-FF and CWPDA-FF are shown. It is distinguished between the first forecasted day and the second forecasted day.

Forecasted day	Error metric	CTRL-FF	CWPDA-FF
Day 1	RMSE	293 $\mathrm{W\,m^{-2}}$	285 $\mathrm{W\,m^{-2}}$
	MAE	234 $\mathrm{W\,m^{-2}}$	229 $\mathrm{W\,m^{-2}}$
	MBE	69 $\mathrm{W\,m^{-2}}$	44 $\mathrm{W\,m^{-2}}$
	Corr	0.51	0.52
Day 2	RMSE	293 $\mathrm{W\,m^{-2}}$	288 $\mathrm{W\,m^{-2}}$
	MAE	231 $\mathrm{W\,m^{-2}}$	228 $\mathrm{W\,m^{-2}}$
	MBE	82 $\mathrm{W\,m^{-2}}$	71 $\mathrm{W\,m^{-2}}$
	Corr	0.52	0.53

afternoon. The reason why the error is lower in the morning than in the afternoon is that there are generally more clouds in the afternoon than in the morning on Reunion Island (see appendix A). Recalling several aspects may help to understand why the error does not increase between the first and second forecasted day. Firstly, the figure shows averages over the 12 observation sites. The individual error curves are different from site to site. And secondly, GHI is often strongly fluctuating and IDW post-processing smoothes the WRF forecasts of GHI (figure 4.9). Not applying IDW and chosing the closest grid box for the WRF GHI forecasts would have several repercussions on figure 5.2. The double penalty problem would be more pronounced, leading to more noise, a lower correlation, a much stronger fluctuation of nRMSE, and generally higher nRMSE values. In other words, the reason why the forecast error does not distinctly increase for the second forecasted day is the combination of RMSE as a metric, IDW as post-processing method, and the variability of GHI. Nevertheless, this approach is appropriate for examining the difference between the performed experiments as shown in the following.

With increasing lead time, the predictability of clouds decreases and the influence of the LBCs is expected to become larger than that of the ICs. This means that the differences between CTRL-FF and CWPDA-FF are expected to be larger for shorter lead times than for larger ones, indicating most DA impact occurs close to the analysis time. According to figure 5.2 (a, c), the difference between CTRL-FF and CWPDA-FF does not change remarkably in the first 14 hours of free forecast. The only exception are the first 2 lead times (0445 UTC and 0500 UTC), for which the RMSE is randomly almost identical for both experiments.

For the day ahead, the difference between CTRL-FF and CWPDA-FF is notably smaller than for the intraday (figure 5.2 (b, d)). The lead time at which this difference becomes remarkably smaller cannot be clearly identified. It obviously lies somewhere between the lead times 14 hours and 29 hours. This finding that

the main impact of DA is visible during the first 24 hours of forecast is in line with the findings from other studies (see section 2.5).

Nevertheless, for almost all day-ahead lead times, the RMSE of CWPDA-FF is still smaller than that of CTRL-FF. Thus, the impact of DA is still visible for the second forecasted day, but it is less distinct than for the first day. The values in table 5.1 confirm this finding. For the day ahead, the application of CWP DA reduces RMSE by 5 $\mathrm{W\,m^{-2}}$, MAE by 3 $\mathrm{W\,m^{-2}}$, and MBE by 11 $\mathrm{W\,m^{-2}}$, when comparing CTRL-FF with CWPDA-FF. Again, the improvement of correlation is marginal, from 0.52 to 0.53. A random result is that the obtained RMSE for the first and second forecasted day is identical for CTRL-FF. The growing bias however confirms that the forecast accuracy generally decreases between the first and the second day.

These findings, together with those from the previous section, indicate that the DA of CWP retrievals generally adds more clouds to WRF, reduces the overestimation of GHI, and therefore acts like a sophisticated bias correction. On average, the additional clouds do not vanish within the first 14 hours of forecast, leading to notably improved intraday GHI forecasts. This improvement is still visible for the second forecasted day, but it is visibly reduced compared to the intraday improvement. Following the findings in section 5.2, it may be argued that the larger intraday impact is a result of both corrected cloud locations and the generally increased amount of clouds in WRF. The influence of the corrected cloud locations decreases for the day ahead as the clouds that WRF simulates for the second day are naturally less and less congruent with the intraday clouds. It can therefore be assumed that the positive impact that is visible for the second forecasted day is mainly a result of the generally increased cloud amount due to CWP DA. This leads to a GHI forecast error reduction especially for the sites that are located in the mountains in the lee of the tradewinds.

5.4 One-way nested domain forecasts

The previous two sections focus on the GHI forecast errors for the large WRF domain with 12 km grid spacing, the domain for which DA is applied. This section examines the influence of grid spacing and nesting by evaluating the experiments with a one-way nested domain with a grid spacing of 4 km, i.e. CTRL-FF-NEST and CWPDA-FF-NEST. These are also referred to as "the cyclic FF-NEST experiments" in the following.

Table 5.2 lists the results for these two experiments in the same manner as table 5.1, with one value per metric, forecasted day, and experiment. For the first forecasted day, CWPDA-FF-NEST performs better than CTRL-FF-NEST in terms of all metrics. There is a difference of 8 $\mathrm{W\,m^{-2}}$ in RMSE and 3 $\mathrm{W\,m^{-2}}$ in MAE. This indicates that the positive intraday impact from DA on the cloud and irradiance forecasts is transferred, to some extent, to the nested domain. In

comparison with table 5.1, between the coarse and the nested domain, there is also a clear intraday error reduction in terms of all metrics except for correlation. For example, RMSE is lower by 8 $W\,m^{-2}$, and MAE by 13 $W\,m^{-2}$ for CWPDA-FF-NEST compared to CWPDA-FF. These numbers confirm that increasing the spatial resolution allows to reduce the intraday GHI forecast error. Nevertheless, further experiments need to be conducted to determine the optimal grid spacing and nesting approach. For an operational application this involves finding a balance between forecast accuracy, WRF runtime, and computational cost.

Table 5.2 – Same as table 5.1 but for the experiments CTRL-FF-NEST and CWPDA-FF-NEST.

Forecasted day	Error metric	CTRL-FF-NEST	CWPDA-FF-NEST
Day 1	RMSE	285 $W\,m^{-2}$	277 $W\,m^{-2}$
	MAE	219 $W\,m^{-2}$	216 $W\,m^{-2}$
	MBE	35 $W\,m^{-2}$	7 $W\,m^{-2}$
	Corr	0.51	0.52
Day 2	RMSE	281 $W\,m^{-2}$	286 $W\,m^{-2}$
	MAE	213 $W\,m^{-2}$	218 $W\,m^{-2}$
	MBE	43 $W\,m^{-2}$	39 $W\,m^{-2}$
	Corr	0.55	0.52

For both the first and the second forecasted day, MBE is lower for CWPDA-FF-NEST than for CTRL-FF-NEST (table 5.2). This indicates a generally increased amount of clouds in the nested domain due to DA, up to the second day of forecast. Moreover, MBE is distinctly lower in both NEST experiments (table 5.2) compared to the coarser domain (table 5.1). This can mainly be explained by the different IDW radii that are used for the 12 km and the 4 km domain (section 3.6). Since the chosen IDW radius for the nested domain is smaller, there is less influence of grid boxes that are located over the ocean in the GHI forecasts. Consequently, the weighted contribution of generally "more cloudy" grid boxes located over the mountains of Reunion Island is larger.

Tables 5.1 and 5.2 reveal that the differences between the experiments in terms of correlation are little. Consequently, among the considered metrics, correlation itself is the least meaningful for experiment comparison. It is however worth considering correlation for the identification of suitable IDW radii (figure 5.3). For small IDW radii or when chosing the nearest grid box for the GHI forecasts, the double penalty problem strongly affects the GHI forecasts. This leads to a strong scattering when comparing forecasts with observations for several days and to a rather low correlation (IDW radius 36 km in figure 5.3). Smoothing the GHI forecasts using IDW reduces this scattering and consequently increases the correlation (IDW radius 75 km in figure 5.3). Further increasing the IDW radius increases the weight of grid boxes that are far from the observation site. This

leads to a reduction of correlation (IDW radius 115 km in figure 5.3). Consequently, considering correlation for different IDW radii allows to identify the radii that lead to suitable results. These radii depending on correlation help to find compromises in terms of the other considered metrics that may be better for different IDW radii. Given the fact that the correlation is the least expressive metric for experiment forecast error comparison, the focus is set on the other metrics in the following.

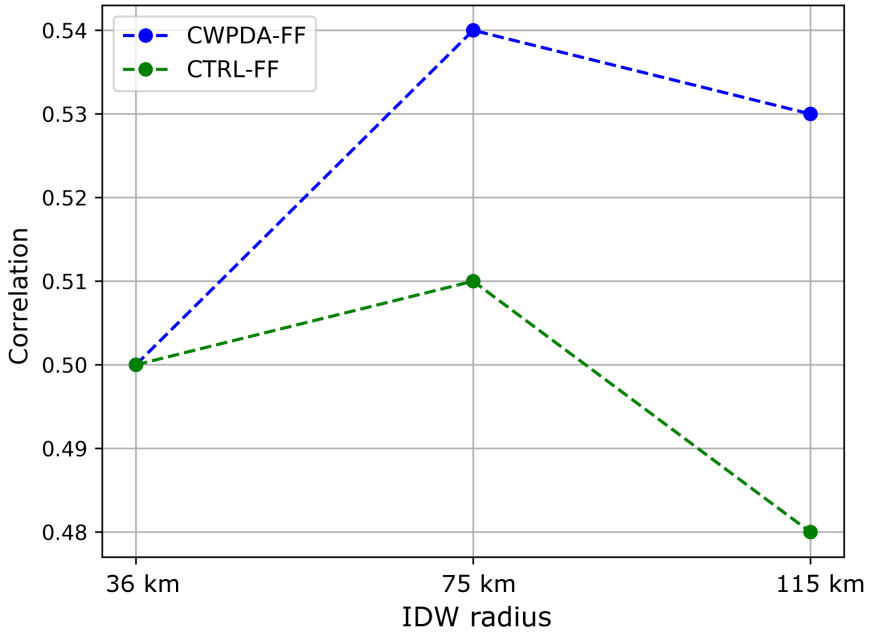

Figure 5.3 – Correlation of the WRF intraday GHI forecasts for the experiments CTRL-FF and CWPDA-FF as a mean over the 12 considered sites. The results for the three different IDW radii 36 km, 75 km and 115 km are shown.

Compared to the coarser domain (table 5.1), there is a considerable difference between the intraday and day-ahead forecast errors in terms of the FF-NEST experiments (table 5.2). For CTRL-FF-NEST, the RMSE and MAE actually decrease from day one to day two. The opposite is the case for CWPDA-FF-NEST. Moreover, while CWPDA-FF-NEST performs better than CTRL-FF-NEST for the intraday, it performs worse for the day ahead in terms of RMSE and MAE. The table itself does not allow to determine why the day-ahead RMSE and MAE are lower for CWPDA-FF-NEST than for CTRL-FF-NEST. A more detailed analysis is required to answer this question. Therefore, a site-specific visualisation is given in figure 5.4. The figure shows intraday (a, c) and day-ahead (c, d) MAE (a, b) and RMSE (c, d) for the four cyclic free forecast experiments. The results for CTRL-FF and CWPDA-FF shown in (a) and (c) correspond to the content of figure 5.1 (a) and (b) respectively.

As found in the analysis of figure 5.1 for the intraday, the overall picture of MAE is similar to RMSE. This is also valid for the day-ahead and for the nested

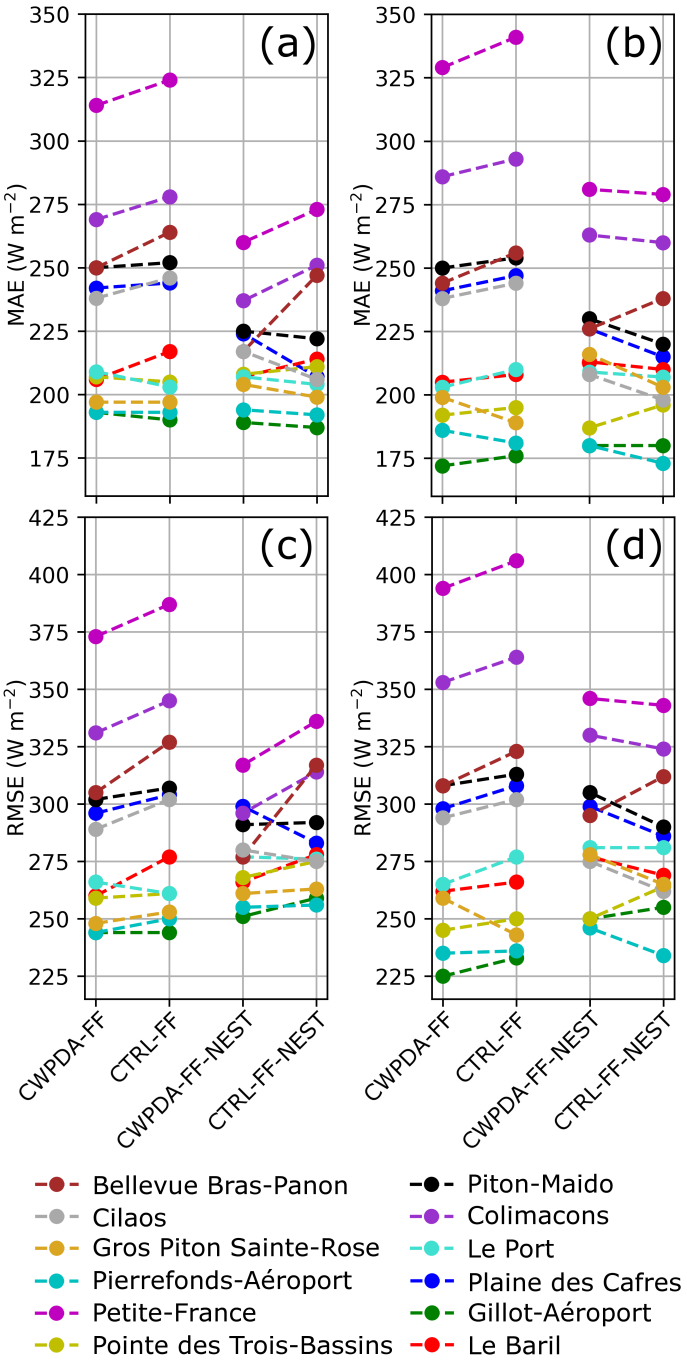

Figure 5.4 – WRF intraday irradiance forecast performance at each site in terms of MAE **(a, b)** and RMSE **(c, d)**. The presentation format of this figure is similar to the one of figure 5.1. The difference between the experiments CTRL-FF, CWPDA-FF, CTRL-FF-NEST, and CWPDA-FF-NEST is shown for each metric. The values represent averages over the entire first forecasted day **(a, c)** and second forecasted day **(b, d)**. Detailed information about the study period and the post processing is given in chapter 3.

domain (figure 5.4). The figure confirms the finding from table 5.2 that CWPDA-FF-NEST generally performs better for the first forecasted day than for the second forecasted day, especially in terms of RMSE. However, no clear site-dependent conclusion can be drawn for the intraday MAE from this figure. Two examples are the sites Piton-Maido and Petite-France, both sites are close to each other and in the mountains in the lee of the trade winds. The intraday MAE for CWPDA-FF-NEST is higher than for CTRL-FF-NEST at Piton-Maido, while the opposite is the case for Petite-France. Such mixed results are a first indicator that the higher resolution of the nested domain includes more noise and randomness in terms of clouds and GHI than the coarser domain.

It is also visible in figure 5.4 that for the day ahead, the errors of CWPDA-FF-NEST are indeed slightly worse than CTRL-FF-NEST for most sites. Nevertheless, this is the case for sites at the coast line as well as sites in the mountains. Eventually, the figure still does not allow to identify why the day-ahead errors for CWPDA-FF-NEST are higher than for CTRL-FF-NEST. It does however indicate that a more specific analysis is necessary to fully understand the day-ahead results for the nested domain.

Consequently, a leadtime-dependent visualisation of nRMSE is given in figure 5.5. The figure shows nRMSE per lead time and allows a comparison between the coarse domain and the nested domain, revealing considerable differences. Notably, the nRMSE of the nested domain output (grey and blue lines in (a) and (b)) is generally lower than that of the coarse domain (black and orange lines in (a) and (b)) in the afternoon, and slightly higher in the morning. This is the case for both forecasted days.

To understand this phenomenon, the results are broken down to site level. Figure 5.5 (c) and (d) show the leadtime-dependent nRMSE for the two sites Gillot-Aeroport and Petite-France, respectively. Petite-France is chosen to represent the mountain sites in the lee of the trade winds in the west of Reunion Island. These are typically the sites where very local clouds often appear in the late morning, just before noon (see appendix A). The nRMSE for the coarse domain (black and orange) increases at that time of the day at Petite-France (figure 5.5 (d)). The nRMSE of the nested domain (grey and blue) remains at approximately the same level as in the morning. This illustrates the effect of the higher resolution of the nested domain, which represents local clouds better to some extent.

However, nRMSE is higher in the morning for the cyclic FF-NEST experiments compared to the coarse domain experiments at Petite-France. The reason for this is that there are generally more clouds in the vicinity of Petite-France in the nested domain compared to the coarse domain. In the afternoon, this leads to reduced errors as explained before. In the clear-sky mornings, however, it leads to larger forecast errors.

For Gillot-Aeroport (figure 5.5 (c)), a site that is located at the north coast of Reunion Island, the difference in nRMSE between the two domains is much smaller than at Petite-France. Moreover, it is not possible to determine clear

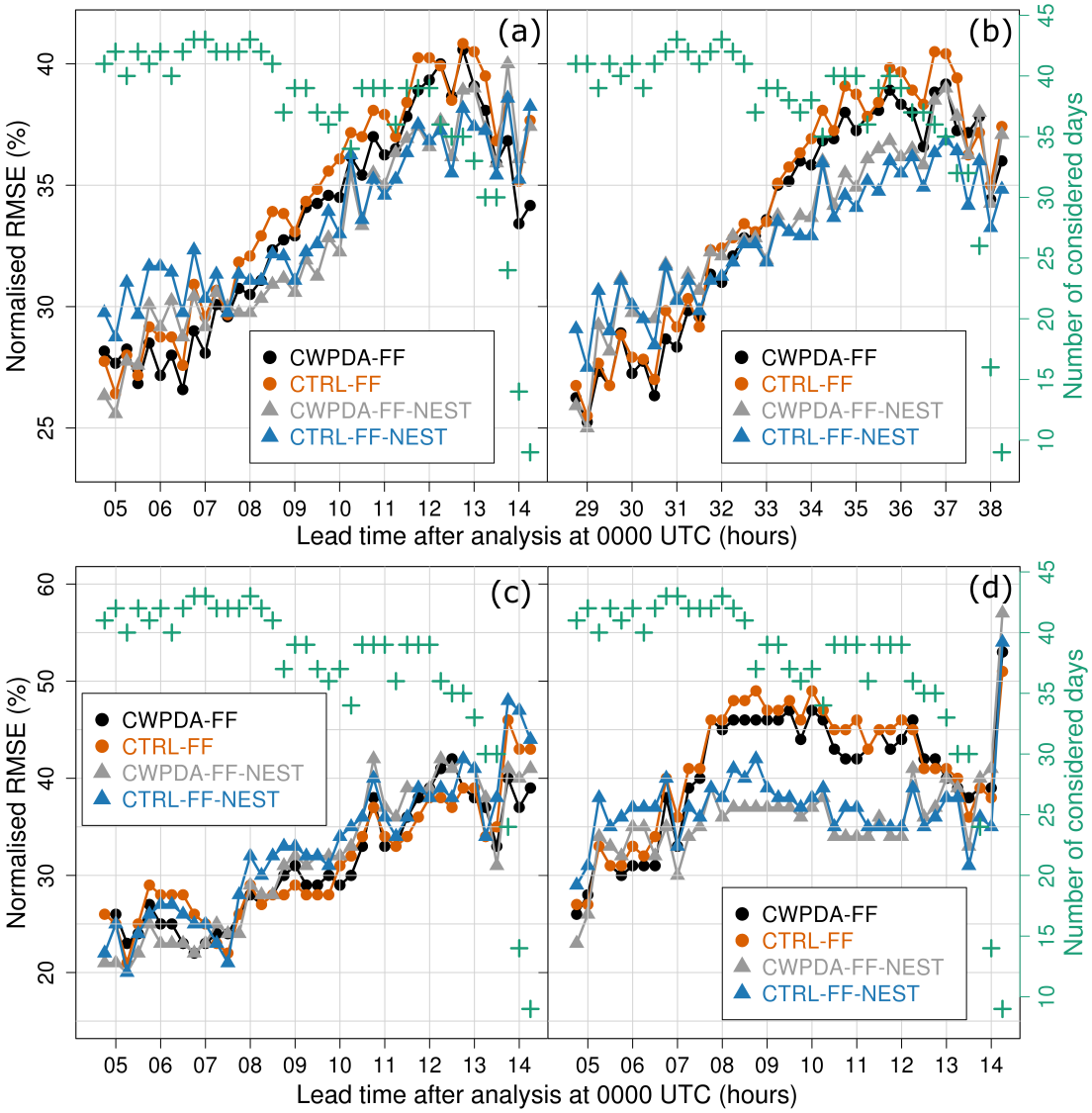

Figure 5.5 – The presentation format of this figure is similar to the one of figure 5.2 (c) and (d). The normalised RMSE per lead time as a mean over the 12 considered sites is shown for the first forecasted day **(a)** and the second forecasted day **(b)**. For the first forecasted day, the sites Gillot-Aeroport **(c)** and Petite-France **(d)** are chosen as examples. The respective values for the experiments CTRL-FF (orange), CWPDA-FF (black), CTRL-FF-NEST (blue), and CWPDA-FF-NEST (grey) are shown. Note that only (b) shows the second forecasted day, while (a), (c), and (d) show the first forecasted day.

patterns of the difference in nRMSE between the nested domain experiments for coastal sites like this one. None of the NEST experiments performs notably better than the other one. It is however visible, that for most of the afternoon the nRMSE of the NEST experiments (grey and blue) is slightly higher than that of

the respective coarse domain experiment (black and orange). Still, the absolute nRMSE difference between these two domains is distinctly larger at the sites in the mountains. Consequently, the contribution of sites that are close to Petite-France (Pointe des Trois-Bassins, Colimacons, Petite-France, Piton Maido, and Cilaos) to the all-site mean in figure 5.5 (a) and (b) is more pronounced than that of the coastal sites. This result is likely to also be obtained when DA is applied directly to a 4 km domain.

On average over all sites, a distinct difference between CWPDA-FF-NEST (grey) and CTRL-FF-NEST (blue), and consequently a positive influence of DA, is visible until a forecast lead time of approximately 10 hours (figure 5.5 (a)). More specifically, the difference between CTRL-FF-NEST and CWPDA-FF-NEST is largest at a lead time of 5 hours and becomes continuously smaller with increasing lead time. From approximately 10 hours onwards and for the entire second forecasted day (except for the first two lead times at 29 hours), CTRL-FF-NEST and CWPDA-FF-NEST have a similar nRMSE. A comparison of (c) and (d) indicates that especially the sites in the mountains around Petite-France contribute to this outcome.

In summary, the one-way nested domain in the context of DA allows to reduce forecast errors, especially around noon of the first forecasted day, and especially for the sites in the mountains in the lee of the tradewinds. For the other sites, and especially the coastal sites, no clear benefit due to the one-way nested domain is visible.

5.5 Dynamical downscaling versus DA cycling

Up to this point, only the cyclic experiments (CTRL-FF, CWPDA-FF, CTRL-FF-NEST, and CWPDA-FF-NEST) have been analysed. The fundamental difference in the dynamical downscaling experiments (DWNSC and DWNSC-NEST) is that no DA and no cycling is performed. In this section, the free forecasts from the cyclic experiments with one-way nested domains (CTRL-FF-NEST and CWPDA-FF-NEST) are compared to the two-way nested domain forecasts in DWNSC-NEST. Moreover, the impact of nested LAM domains at a higher resolution on GHI forecasts on Reunion Island is assessed to answer research question 2 in chapter 1 ("What impact do high-resolution nested LAM domains have on GHI forecasts on Reunion Island?"). In general, it is to be expected that the lowest forecast errors are obtained from the experiments with a nested domain, meaning CTRL-FF-NEST, CWPDA-FF-NEST, or DWNSC-NEST. Due to the higher horizontal resolution, the nested domain should allow to forecast local cloud processes and breeze effects more accurately. This is independent of the question whether one-way or two-way nesting is applied.

Evaluating the difference between the free forecasts from cycling (CTRL-FF and CWPDA-FF) and from DWNSC is not straightforward. The problem with this

comparison is that these are two very different experiment setups. It is important to note that all of the free forecast experiments use the same LBCs, i.e. hourly input from the 0000 UTC GFS run. The difference between the experiments lies in the origin of the ICs and the nesting configuration. The ICs in DWNSC are directly obtained from the 0000 UTC GFS analysis. In CTRL-FF, the ICs originate from the cyclic 6 hour first guess forecasts. This is also the case for CWPDA-FF with the addition of WP retrieval assimilation. Moreover, DWNSC benefits from the nested domain (DWNSC-NEST) via the two-way nesting, while no information is fed back from the nested domain to the coarse domain in CTRL-FF and CWPDA-FF.

Table 5.3 shows intraday and day-ahead RMSE and MAE for the DWNSC experiments and the cyclic experiments with DA. As expected, the errors of the NEST experiments are generally lower than those of the coarser domain. The only exception is the RMSE of the DWNSC experiments, which is marginally higher for DWNSC-NEST compared to DWNSC for the day ahead. MAE however is distinctly lower for DWNSC-NEST for both forecasted days.

Table 5.3 – WRF GHI forecast accuracy in terms of RMSE and MAE as a mean over the 12 considered sites. The results for the experiments CWPDA-FF, CWPDA-FF-NEST, DWNSC, and DWNSC-NEST are shown. It is distinguished between the first forecasted day and the second forecasted day. Detailed information about the study period and the post processing is given in chapter 3.

Forecasted day	Error metric	CWPDA-FF	CWPDA-FF-NEST	DWNSC	DWNSC-NEST
Day 1	RMSE ($W\,m^{-2}$)	285	277	265	254
	MAE ($W\,m^{-2}$)	229	216	220	196
Day 2	RMSE ($W\,m^{-2}$)	288	286	280	281
	MAE ($W\,m^{-2}$)	228	218	226	214

For both domains, DWNSC performs better than the cyclic experiments in terms of both metrics. Considering the fundamental difference between the experiment setups, this outcome does not mean that DA does not improve the GHI forecasts. It is demonstrated in the previous chapters that DA does improve the forecasts, by comparing CTRL-FF with CWPDA-FF. Only these cyclic experiments are directly comparable, because of the explanation given above about the ICs. The comparison between DWNSC and CWPDA-FF does however show that the ICs of DWNSC are more presumably more accurate than those of CWPDA-FF. The latter rely heavily on 6 hour first guess forecasts, while DWNSC uses downscaled ICs from the 0000 UTC GFS. Consequently, reducing the DA cycling interval in CWPDA, for example to 1 hour instead of 6, would reduce the length of the first guess forecasts, further improve the ICs of CWPDA-FF, and supposedly further reduce the RMSE and MAE of CWPDA-FF. It may be hypothesised, that in that case the errors of CWPDA-FF would be lower than those of DWNSC. This hypothesis is to be validated with future experiments.

Increasing the cycling frequency is not straightforward. As mentioned in chapter 3, this heavily increases the complexity of the whole WRF-DART cycling framework. Especially the handling of LBCs and retrieval data would have to be fundamentally revised and a lot more data would have to be stored and processed for the cycling procedure.

Figure 5.6 illustrates the intraday and day-ahead MAE for all free forecast experiments and the other considered NWP models. In view of the number of experiments and models that are compared in the figure, this Box-Whisker-Plot is a more lucid representation of the content that is presented in figures 5.1 (b) and 5.4 (a, b). As found in the previous sections, the overall picture between RMSE and MAE is similar. Since this is also valid for the operational NWP models, this figure shows only MAE for the sake of clarity. There are occasional gaps in the operational model forecast data availability due to technical issues. Consequently, not all operational model forecasts are available for all considered times of the study period. In figure 5.6, only those times are considered for which the forecasts of all models are available. Therefore, in terms of the WRF experiments, the values shown in the figure do not exactly correspond to the previously evaluated values. The comparison of the WRF experiments with the operational NWP models is carried out in the next section. In some cases, the sites with the highest MAE are represented as outliers (circles) in figure 5.6, while in other cases these sites are represented as whisker borders. The reason for this is that the whiskers are defined as the first (or third) percentile minus (or plus) 1.5 times the interquartile range. Depending on the MAE distribution among the sites, the sites with the lowest MAE do not lie within this whisker range and are considered as outliers.

For the first forecasted day (figure 5.6 (a)), the overall lower errors of CWPDA-FF and CWPDA-FF-NEST compared to the respective coarse domain experiments are visible. These are indicated by the upper whisker border or outliers, the generally lower boxes, and lower mean (red dots) at least for the 12 km domain. The distinctly lower MAE of the nested domain forecasts is likewise visible for all WRF experiments. The figure reveals that in terms of the sites with the lowest MAE (Pierrefonds-Aéroport or Gillot-Aéroport according to the previous sections), represented by the lower whisker borders, all WRF experiments except for DWNSC-NEST have an intraday MAE of approximately 200 $\mathrm{W\,m^{-2}}$.

Indeed, DWNSC-NEST is the WRF experiment with by far the lowest intraday and day-ahead MAE considering the mean and the lower whisker border. This means that DWNSC-NEST performs considerably better for the coastal sites than for the sites in the mountains, where its performance is even worse than that of CTRL-FF-NEST and CWPDA-FF-NEST. This may be explained by the overall amount of clouds in CWPDA-FF-NEST and DWNSC-NEST. The site-mean MBE of DWNSC-NEST is 68 $\mathrm{W\,m^{-2}}$ and that of CWPDA-FF-NEST is 7 $\mathrm{W\,m^{-2}}$ for the dates considered in figure 5.6. That indicates that on average, DWNSC-NEST contains less clouds than CWPDA-FF-NEST. Compared to CWPDA-FF-NEST, this leads to low forecast errors of DWNSC-NEST at sites where clouds are rare

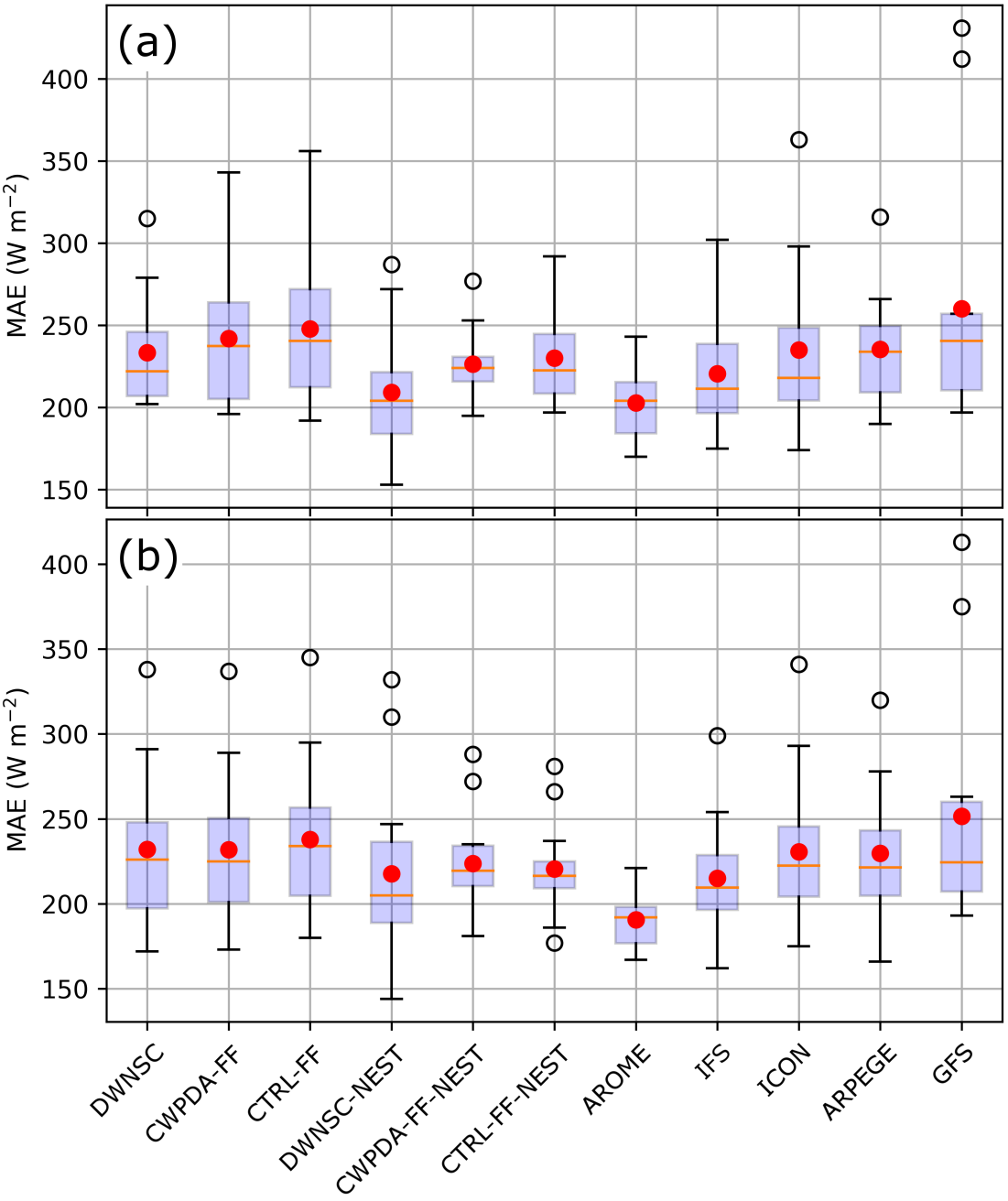

Figure 5.6 – Box-Whisker-Plot showing the interquartile range (boxes), minimum and maximum (whisker borders), and outlying values (empty circles) of the MAE for the different WRF experiments and operational NWP models at the 12 pyranometer sites. The interquartile range (IQR) extends from the 25th percentile (Q1) to the 75th percentile (Q3). The minimum is defined as Q1−1.5×IQR and the maximum as Q3+1.5×IQR. The mean is represented by the red dots and the median is indicated by the red lines. The presentation format of this figure is another way of presenting the data that is shown in figure 5.4 (a) in terms of the respective WRF experiments.

(the coastal sites) and high errors at sites where clouds are frequent (the sites in the mountains). The upper whisker border and the outlier site of CWPDA-FF-NEST in figure 5.6 (a) are lower than that of DWNSC-NEST. This illustrates the positive impact of DA for the sites in the mountains. For these sites, CWPDA-FF-NEST is the WRF experiment with the best intraday performance.

For the second forecasted day (figure 5.6 (b)), the impact of DA vanishes in the nested domain (difference between CTRL-FF-NEST and CWPDA-FF-NEST), as seen in the previous section. As discussed before, the overall distribution of MAE is still shifted towards lower values for CWPDA-FF compared to CTRL-FF.

Comparing DWNSC and CWPDA-FF allows to examine the difference between one-way and two-way nesting to some extent. To completely examine this difference, DWNSC would also have to be performed with a one-way nested domain. There is no distinct day-ahead difference between DWNSC and CWPDA-FF in the figure, and table 5.3 confirms that the average MAE merely differs by 2 $\mathrm{W\,m^{-2}}$. In fact, the differences in the distribution of MAE between DWNSC, CTRL-FF and CWPDA-FF are visibly lower for the second forecasted day than for the first one. As discussed before, this illustrates that with advancing lead time the influence of DA on the GHI forecast decreases. Against the background of one-/two-way nesting, this outcome also shows that two-way nesting does not necessarily improve the coarse domain forecasts for the second forecasted day. This validates that for increasing lead time, the impact of the LBCs governs the accuracy of the coarse domain forecasts.

There is however a distinct difference between DWNSC-NEST and the cyclic NEST experiments for the second forecasted day (figure 5.6 (b)). For the sites with the highest day-ahead MAE, the difference between DWNSC-NEST and the two cyclic FF-NEST experiments is more pronounced than for the intraday. Since the MAE of CTRL-FF-NEST and CWPDA-FF-NEST is similar at these sites, this difference cannot be explained by the influence of DA. As this is the second forecasted day, the impact of the ICs is not crucial. The remaining elements that can explain the difference are the nesting type and the extent of the nested domain. Apparently, for the second forecasted day, the two-way nesting has the effect that the MAE at the sites in the mountains in the west of Reunion Island is higher than in the one-way nesting experiments. At the same time, at the coastal sites, the two-way nesting leads to lower MAEs than all other WRF experiments. This indicates that on average, the interaction of the nested domain with the coarse domain reduces the amount of clouds in the nested domain. The lower cloud amount reduces the MAE at the coastal sites where clear sky is frequent. At the same time, it increases the MAE at the sites in the mountains where thermally induced convective clouds are frequent. It is possible that the extent of the nested domain is too small, leading to a large influence of the LBCs of the nested domain, that are provided by the coarse domain. For the second forecasted day, the strong influence of the LBCs may hinder the nested domain to properly develop convection for example. A more detailed investigation with different parameterisation

schemes, different domain sizes, and different grid spacings is necessary to identify the reasons for this behaviour.

5.6 Comparison with operational models

This section puts the GHI forecast errors of the WRF experiments in relation to the forecast errors of several operational NWP models, operated by different national weather services, as described in section 3.8. The goal of this section is explicitely not to identify "the best" model. This is because when evaluating the obtained forecast errors, different factors need to be taken into consideration. Two major factors are the duration of the selected study period and the performed post-processing. Both of these factors largely impact the result of GHI forecast error analyses. Moreover, one NWP model may perform better than another for a given day and weather situation. Identifying the model with the lowest average forecast error does not mean that this model performs best every day and at every site. However, what the comparison does allow, is to assess the impact of using LAMs compared to GCMs, i.e. research question 1 raised in chapter 1 ("Do LAMs forecast ground-level solar irradiance more accurately than GCMs on Reunion Island?"). Furthermore, the difference between WRF forecasts that do or do not benefit from DA can be put in relation to the forecast error range of the operational models.

Table 5.4 lists the forecast errors of the different models in terms of RMSE, MAE, and MBE. For the sake of clarity, among the performed WRF experiments only DWNSC-NEST is represented in the table. The reason for chosing only this experiment in the table is that the errors of the cyclic free forecast experiments are less comparable to those of the operational models, for the same reasons as given in the previous section. Moreover, DWNSC-NEST leads to the lowest average forecast errors among all WRF experiments.

Table 5.4 – GHI forecast errors in terms of RMSE, MAE and MBE as a mean over the 12 considered sites and the considered period. The results for the experiment DWNSC-NEST and the operational NWP models AROME, IFS, ICON, ARPEGE, and GFS are shown. It is distinguished between the first forecasted day and the second forecasted day. Detailed information about the study period and the applied post processing is given in chapter 3.

Forecasted day	Error metric	DWNSC-NEST	AROME	IFS	ICON	ARPEGE	GFS
Day 1	RMSE ($W\,m^{-2}$)	266	267	273	297	281	316
	MAE ($W\,m^{-2}$)	209	203	221	235	235	260
	MBE ($W\,m^{-2}$)	74	-58	45	59	54	99
Day 2	RMSE ($W\,m^{-2}$)	283	246	268	288	281	308
	MAE ($W\,m^{-2}$)	218	191	215	231	230	252
	MBE ($W\,m^{-2}$)	120	-19	55	55	82	73

In terms of the GCMs (IFS, ICON, ARPEGE, GFS), the MAE interquartile range lies between approximately 200 and 250 $\mathrm{W\,m^{-2}}$ for both forecasted days (figure 5.6 (a, b)). According to table 5.4, IFS is the GCM with the lowest GHI forecast errors in terms of RMSE, MAE and MBE for both forecasted days. GFS has the highest average intraday and day-ahead forecast errors in terms of RMSE and MAE (table 5.4). This is not least because of the two outlier sites with the highest obtained MAE of all considered models (figure 5.6). Compared to the other GCMs, the mean RMSE and MAE of ICON and ARPEGE are rather similar, except for intraday RMSE which is distinctly lower for ARPEGE (table 5.2). All GCMs have a positive intraday and day-ahead MBE between 45 and 99 $\mathrm{W\,m^{-2}}$. This indicates once more that NWP models underpredict the presence of clouds and overpredict GHI, not only in mid-latitudes but also at a tropical island such as Reunion. Nevertheless, it has to be kept in mind that the applied IDW post-processing favors a positive bias, especially for the GCMs for which the largest IDW radii are applied.

Concerning research question 1, figure 5.6 shows that there is a clear interest in considering LAMs for GHI forecasting on Reunion Island. In terms of the mean and the interquartile range, AROME performs distinctly better than its driving models IFS and ARPEGE, and WRF (DWNSC-NEST) performs distinctly better than its parent GCM, i.e. GFS. It is worth mentioning that AROME is the only NWP model with a negative MBE in table 5.4. The application of other IDW radii for AROME lead to similar negative MBEs.

While the intraday interquartile range of DWNSC-NEST and AROME is similar in figure 5.6, a large difference can be seen for the second forecasted day. The interquartile range of DWNSC-NEST is shifted towards higher MAE values and closer to that of the parent domain for the second day. This phenomenon is discussed at the end of the previous section and probably linked to the nesting configuration. The fact that the forecast errors of AROME are not worse for the second forecasted day demonstrates that low day-ahead forecast errors may in fact be obtained with a LAM. This reinforces the hypothesis that the day-ahead errors of DWNSC-NEST could be lower using another nesting configuration. More specifically, this result strenthens the hypothesis that increasing the extent of the nested WRF domain may considerably reduce the WRF day-ahead forecast errors.

As discussed in the previous sections, the positive impact of DA on GHI forecasts is visible in the difference between CTRL-FF and CWPDA-FF, as well as CTRL-FF-NEST and CWPDA-FF-NEST (figure 5.6). Moreover, as found in this section, it is beneficial to use LAMs compared to GCMs. The combination of these two findings allows an assessment of the potential of DA for solar irradiance forecasts on Reunion Island. It may be hypothesised that lowest obtained WRF GHI forecast errors (the ones from DWNSC-NEST) can be further reduced. To achieve this goal, following different traces should lead to lower errors of CWPDA-FF-NEST. These traces include increasing the cycling interval, defining more accurate WP retrieval errors, and further investigating the issues encountered in terms of

nesting.

5.7 Discussion and conclusion

After the evaluation of GHI forecast errors in this chapter, the research questions that are raised in chapter 1 with respect to the tropical conditions on Reunion Island can be answered.

Research question 1 *Do LAMs forecast ground-level solar irradiance more accurately than GCMs on Reunion Island?*

Answer: Section 5.6 shows that the errors of short-term (up to 40 hours) GHI forecasts of the two considered LAMs are considerably lower than those of their parent GCMs. It is to be expected that this result is also valid for a longer evaluation period of for example one year. The benefit of using highly resolved LAMs for GHI forecasting on Reunion Island is thus demonstrated.

Research question 2 *What impact do high-resolution nested LAM domains have on GHI forecasts on Reunion Island?*

Answer: From the results in sections 5.5 and 5.6 it can be concluded that high resolution nested domains are especially useful for intraday forecasting. It is found in section 5.4 that the GHI forecasts of the one-way nested WRF domain at 4 km grid spacing are more accurate for the first forecasted day than those of the coarser domain with 12 km grid spacing.

Research question 3 *Until what forecast lead time is the impact of satellite data assimilation on GHI forecasts noticeable?*

Answer: There is a distinct positive impact of DA on the WRF GHI forecasts of the first forecasted day, meaning up to lead times of between 14 and 29 hours (section 5.3). The positive impact is passed on to the one-way nested domain. Nesting allows to further reduce the GHI forecast errors. For the second forecasted day, a GHI forecast error reduction due to DA can still be observed for the coarse domain, but it is lower than the impact on the intraday forecasts. The current nesting setup leads to mixed results for the nested domains for the second day forecasts.

The tables in this chapter indicate one error value per experiment for the whole study period, which only gives an indication. In the case of the coarse domains this is often sufficient to make a first conclusion. Additionally, the evaluations per forecast lead time give more insight. For the nested domain, a clear positive impact of DA is visible for the first day. However, the results are very different depending on the site when increasing the model resolution, especially for the

second forecasted day. Eventually, the evaluation becomes more and more difficult with increasing model resolution.

It should be kept in mind that the results in section 5.4 concern one-way nested domains. The DWNSC-NEST results show that the outcome of two-way nesting is considerably different. Moreover, it is to be expected that lowering the cycling interval, e.g. to one hour, would lower the error of CWPDA-FF(-NEST). Following the goal of lowering GHI forecast errors, it should be validated with future experiments whether: 1) an increased cycling frequency reduces the GHI forecast errors substantially, 2) directly performing DA at a sufficiently large domain with 4 km grid spacing is more beneficial than a nesting approach, and 3) an optimised nesting configuration can be found in terms of domain size, grid spacing and parameterisation schemes.

All NWP model forecasts that are considered in this chapter are initialised from 0000 UTC analyses. Since DA is especially beneficial for intraday forecasting, a higher cycling frequency may also allow to generate free forecasts more frequently than every 6 hours. From an operational point of view, this is another potential benefit of using LAMs compared to GCMs. Nevertheless, a compromise needs to be found between computational cost and overall forecast errors.

The WRF ensemble that is applied in the cycling experiments may also be applied to the free forecasts. This would also increase the cost of computation, but it would allow to produce ensemble-based probabilistic solar irradiance forecasts. Moreover, improving the accuracy of the free forecast ensemble as a result of such experiments would certainly have positive effects on the analysis ensemble. This would allow to improve the analyses determined by the EnKF, and in turn further reduce the deterministic GHI forecast errors.

The DA approach that is followed in the experiments in this thesis is cloud property assimilation. It is demonstrated that, to some extent, this approach allows to correct for the location of existing clouds in the analyses. This means that the clouds need to be present at the time of the analysis. It may therefore be hypothesised that this approach has less impact in certain situations prior to convective initiation. Radiance assimilation might produce more realistic analyses in situations where convective clouds are not present at the time of the analysis but do form in the first hours of the forecast. Ideally, a comparison of both methods with the same model, which is missing so far (chapter 2), should be performed. This would allow to examine this hypothesis and examine the advantages and disadvantages of both methods.

Chapter 6

Conclusion and outlook

Summary

This chapter concludes the thesis' findings in terms of the three objectives established in chapter 1. One of the most promising satellite DA approaches to improve short-term GHI forecasts in the southwestern Indian Ocean is identified and evaluated in this thesis. The evaluation of the performed experiments reveals that the application of this method allows to improve cloud analyses. Eventually, the improved analyses have a measurable positive impact on short-term GHI forecasts on Reunion Island. Future experiments with the applied system should focus on more realistic retrieval errors, further experiments at convection resolving resolution, and the exploitation of the applied WRF ensemble. Satellites of the newest generation bring new opportunities to further improve satellite data assimilation. Long-term evaluations and intercomparison studies of different approaches should be performed to stretch the boundaries of what is possible.

Diverse stakeholders of the photovoltaic power value chain require more accurate forecasts of global horizontal irradiance in order to optimally exploit the solar power potential and guarantee grid stability. In the long term, more accurate solar irradiance forecasts shall permit to raise the current legal injection limits for renewable energies. This especially accounts for non-interconnected areas with a high potential for PV, such as the French overseas territory of Reunion Island, located in the southwestern part of the Indian Ocean. Pronounced tropical convection often causes a high variability and limited predictability of GHI on Reunion Island, especially in austral summer. In contrast to global circulation models, limited-area NWP models allow to resolve cloud and radiation processes in the order of kilometres and minutes. One important factor that impacts the GHI forecast error of NWP models is the accuracy of their initial conditions.

Geostationary meteorological satellites provide valuable observations that can be used in data assimilation for cloud analysis determination. This implies more accurate initial conditions and consequently more accurate solar irradiance forecasts. The goal of this thesis was the application of geostationary satellite data assimilation with a limited-area numerical weather prediction model to improve the accuracy of solar irradiance forecasts in a tropical environment. Three major

objectives are followed in this thesis as defined in chapter 1. The conclusions that are obtained in terms of each objective are summarised in this chapter and for each objective an individual outlook is given.

Objective 1 *The identification of a promising geostationary satellite data assimilation approach for regional-scale NWP regarding clouds and solar irradiance forecasts in the tropics.*

Conclusion

A comprehensive review of state-of-the-art research and operational studies is given in chapter 2. The focus is set on the assimilation of geostationary meteorological satellite observations in limited-area models with the goal of improving forecasts of cloud-related parameters. It is differentiated between two fundamentally different approaches - radiance and cloud property retrieval assimilation.

Various approaches are reviewed with respect to the large variety of existing LAMs, DA methods, satellite sensors and channels, and retrieval products. To overcome the numerous methodological challenges, cloud analysis methods for regional models have become more sophisticated in recent years. Since the optical and thermal sensors on geostationary meteorological satellites do not capture information inside clouds, the data assimilation techniques have to be adopted for different cloudiness conditions. A common goal among of the different approaches is the exploitation of a maximum of available observations from geostationary satellites.

The state of the art review reveals that so far there has not been any research focus on satellite DA with regional models in a tropical environment. The diversity of existing approaches and a lack of intercomparison studies makes it impossible to identify "the best" approach. Eventually, in the context of this thesis, the literature review allows to chose a promising approach to be applied to solar irradiance forecasting on Reunion Island. Specifically, it is the assimilation of physical cloud properties, more precisely cloud water path retrievals with an ensemble Kalman filter in a LAM. The applied LAM is the Weather Research and Forecasting (WRF) model and the chosen DA environment is the Data Assimilation Research Testbed (DART) with its forward operator for cloud water path.

Outlook

As more geostationary satellites of the third generation become operational, the resolution of such observations increases and global gridded cloud products may be of higher resolution in the future. This would open new possibilities for multi-layer cloud information to be assimilated in a similar manner as in this thesis. New generations of geostationary satellites like Himawari-8, MTG and GOES-R bring more advanced sensors with more channels and higher temporal and spatial resolution. This imposes new challenges and brings more opportunities for data assimilation methods and NWP. It is desirable that this leads to an increased

exchange between researcher communities and weather service providers in order to use the newly available observations as efficiently as possible with the diverse LAMs that exist.

The future lies in combined approaches that make the best possible use of available observations, radiance and cloud property assimilation methods and hybrid data assimilation techniques. The optimal use of cloud-free and cloud-affected radiance assimilation as well as available derived cloud properties will lead to more accurate cloud analyses and short-term cloudiness forecasts.

Most currently existing methods described in peer-reviewed literature are not evaluated over periods longer than a few days. This thesis fills this gap of missing long term studies to some extent, but comparisons of the various existing satellite DA approaches still need to be performed. While many methods are being developed and evaluated separately, there is currently a lack of intercomparison studies of different approaches under the same conditions. For example, the strengths and weaknesses of radiance and retrieval assimilation could be examined in a comparison of both methods under the same conditions.

Objective 2 *The improvement of cloud analyses in the southwestern Indian Ocean using limited-area NWP and geostationary satellite DA.*

Conclusion

Following the approach that is chosen as a result of the state of the art review, gridded Meteosat-8 retrievals of liquid, supercooled liquid and ice water path from NASA Langley's SatCORPS cloud products are assimilated using WRF-DART at 12 km grid spacing in a 6-hourly cycling procedure. Control experiments without DA are performed for both the cycling and free forecasts, enabling an evaluation of the impact of the applied DA methodology.

It is demonstrated that the assimilated retrievals of IWP, SWP and LWP have most impact at pressure levels around 400 hPa, 500 hPa and 850 hPa respectively. The largest contribution is achieved with the IWP retrievals with an average reduction in RMSE of approximately 0.2 $\mathrm{kg\,m^{-2}}$ between first guess and analysis. Among the three considered phases, the liquid phase retrievals have the lowest impact.

An evaluation of the obtained cloud analyses using independent radiosoundings shows a reduced bias in specific humidity, especially in the mid-troposphere, for the experiment with CWP DA compared to the control experiment without DA. A reduction of this bias between the first guesses and analyses supports the hypothesis that the applied DA method leads to more realistic WRF humidity profiles and consequently improves the 'cloud analyses'.

Outlook

It is demonstrated in this thesis that the assimilation of NASA SatCORPS' gridded

multi-phase cloud water path from Meteosat-8 allows to improve WRF cloud analyses in the SWIO. Nevertheless, there is a potential to further improve the applied approach. This concerns especially the CWP retrieval error definition. The results obtained in this thesis indicate that experiments with retrieval assimilation at convection-resolving resolution in the SWIO, and using a shorter cycling interval, hold promise for a further improvement of cloud analysis accuracy and reduction of GHI forecast errors. As the utilised gridded cloud products are available globally, the method offers a portable and globally applicable approach. Consequently, the approach should be evaluated for other regions of the Earth.

Besides solar power forecasting, better cloud analyses and cloudiness forecasts may also be helpful for research, defence and societal applications. Research-wise, continuous efforts are being made to improve the representation of clouds in global and regional NWP models used for weather forecasting and climate projections. Forecasts of clouds and precipitation also greatly influence land surface or hydrological models. Numerous defence applications require accurate information about sky conditions on the operation terrain, especially the presence of a cloud free line of sight. Remote monitoring systems using optical and thermal vision, optical communication between ground and airplane or satellite and optronic aiming sight are not operational in cloudy conditions. Finally, cloud cover presence must also be forecasted for societal applications. Better forecasts of cloud systems allow weather services to adequately warn the population in case of severe weather and tropical cyclones. Air traffic and road management needs accurate information about cloud base height, fog, icing and precipitation. In the health sector, cloud information is increasingly used to assess air pollution and ultraviolet exposure. A wide range of economic sectors are also influenced by cloud forecasts. For example, some leisure activities, such as sailing, paragliding, or photography are strongly dependent on cloud cover. Consequently, the tourism sector increasingly benefits of the added economic value of improved cloud analyses and forecasts.

Objective 3 *The quantification of the impact of the applied DA approach on short-term (5 to 40 hours) solar irradiance forecasts on Reunion Island.*

Conclusion

It has been shown in previous studies that the assimilation of geostationary CWP retrievals with WRF-DART leads to improved short-term GHI forecasts. However, this improvement has never been quantified for study periods of more than a few days and under tropical conditions. In this thesis, the successful assimilation of multi-phase geostationary CWP retrievals with a 41-member WRF ensemble over the SWIO is demonstrated for a total of 44 days in austral summer and the impact on short-term GHI forecasts for Reunion Island is quantified.

A clear positive impact of the applied DA methodology on short-term solar irradiance forecasts is demonstrated in this thesis. The case study in chapter 4

demonstrates that the location of clouds in the analysis has a considerable influence on the subsequent forecast of solar irradiance. The comparison between inverse-distance weighted WRF GHI forecasts and ground-based observations at 12 sites on Reunion Island allows a quantification of the DA impact.

The refinement of the forecast initial conditions using CWP DA positively impacts intraday GHI forecasts. On average over the 12 considered sites, the evaluation of GHI forecasts from the experiments without and with DA shows a reduction of 11 $\mathrm{W\,m^{-2}}$ (4 %) for RMSE and 6 $\mathrm{W\,m^{-2}}$ (3 %) for MAE as a consequence of the applied retrieval assimilation. A positive but less distinct impact on the second forecasted day can be observed.

Two major effects of the applied method can be deduced. Firstly, the location of large-scale cloud systems is corrected in the analyses and the forecasts. Secondly, the increased amount of lower tropospheric water in WRF leads to more breeze-induced convection, especially at the west coast of Reunion Island. On average, the retrieval assimilation adds more clouds to WRF, reduces the overestimation of GHI, and therefore acts like a sophisticated bias correction of cloudiness and solar irradiance forecasts.

Outlook

This work is a contribution to improved short-term solar irradiance forecasts in complex tropical environments. The obtained results allow to produce more accurate short-term solar power forecasts, and may have positive impacts on other applications that depend on accurate information about cloudiness.

The results that are obtained in this thesis show that increasing the LAM resolution to convection permitting resolution allows to lower forecast errors. Nevertheless, there is a need for future research on the interplay of grid spacing and the extent of nested domains in the context of satellite DA with LAMs. Moreover, the difference between radiance and cloud property assimilation in terms of GHI forecast accuracy remains a relevant objective for future work. Since the applied DA approach in this thesis makes use of an analysis ensemble, an extension of the deterministic free forecast experiments to ensemble forecasts of solar irradiance is desirable. This would allow to perform frequently updated probabilistic solar power forecasts and exploit the combination of NWP technology and geostationary satellite observations at the best.

Appendix A

GHI time series

Figures A.1, A.2 and A.3 show the time series of ground-based GHI observations that are considered as a reference for the comparisons with GHI forecasts from NWP models. The raw observations from Météo-France pyranometers are quality checked and interpolated to 15 minutes as explained in section 3.6. Figure A.1 shows four of the sites that are located on the coast line of Reunion Island. Four sites that are located in the lee of the tradewinds, in the mountains in the west of Reunion Island are shown in figure A.2. Figure A.3 shows the remaining four sites, with Gros Piton Sainte-Rose and Le Baril being also located at the coast line, but on the upwind side of the trade winds.

A large amount of clear-sky moments is visible for the coastal sites (figure A.1), compared to the four sites located in the mountains (figure A.2). This is because thermally induced clouds are often present at the sites in the mountains, but extend less often to the coast line.

As can be seen in figure A.2, all observations before 0500 UTC (9 am local time) are omitted for the sites Colimacons, Petite-France, and Cilaos. The reason for this are shadowing effects caused by the mountains that are not taken into account by WRF and the other operational models.

For the majority of the sites, the heat maps indicate that clouds appear more frequently in the afternoon than in the morning at Reunion Island. The reason for this are convective clouds created by orographic uplift at day time.

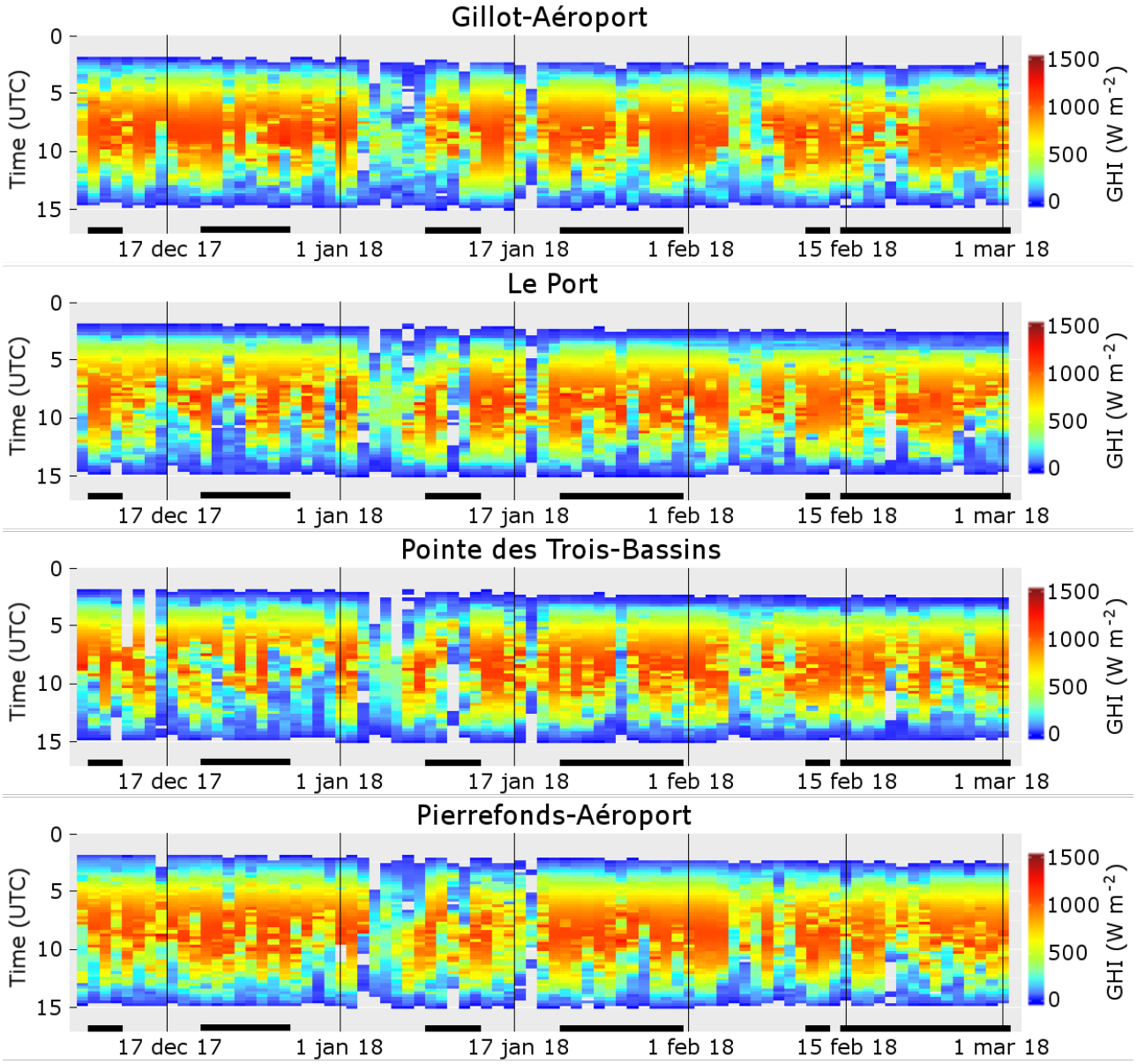

Figure A.1 – Heat maps showing the quality checked time series of GHI observations on Reunion Island that are considered as a reference for the GHI forecast evaluation. Each column represents one day with the hour of the day shown on vertical axis. The horizontal black bars indicate the days for which intraday forecasts are performed in the free forecast experiments. The coastal sites Gillot-Aéroport, Le Port, Pointe des Trois-Bassins, and Pierrefonds-Aéroport are shown.

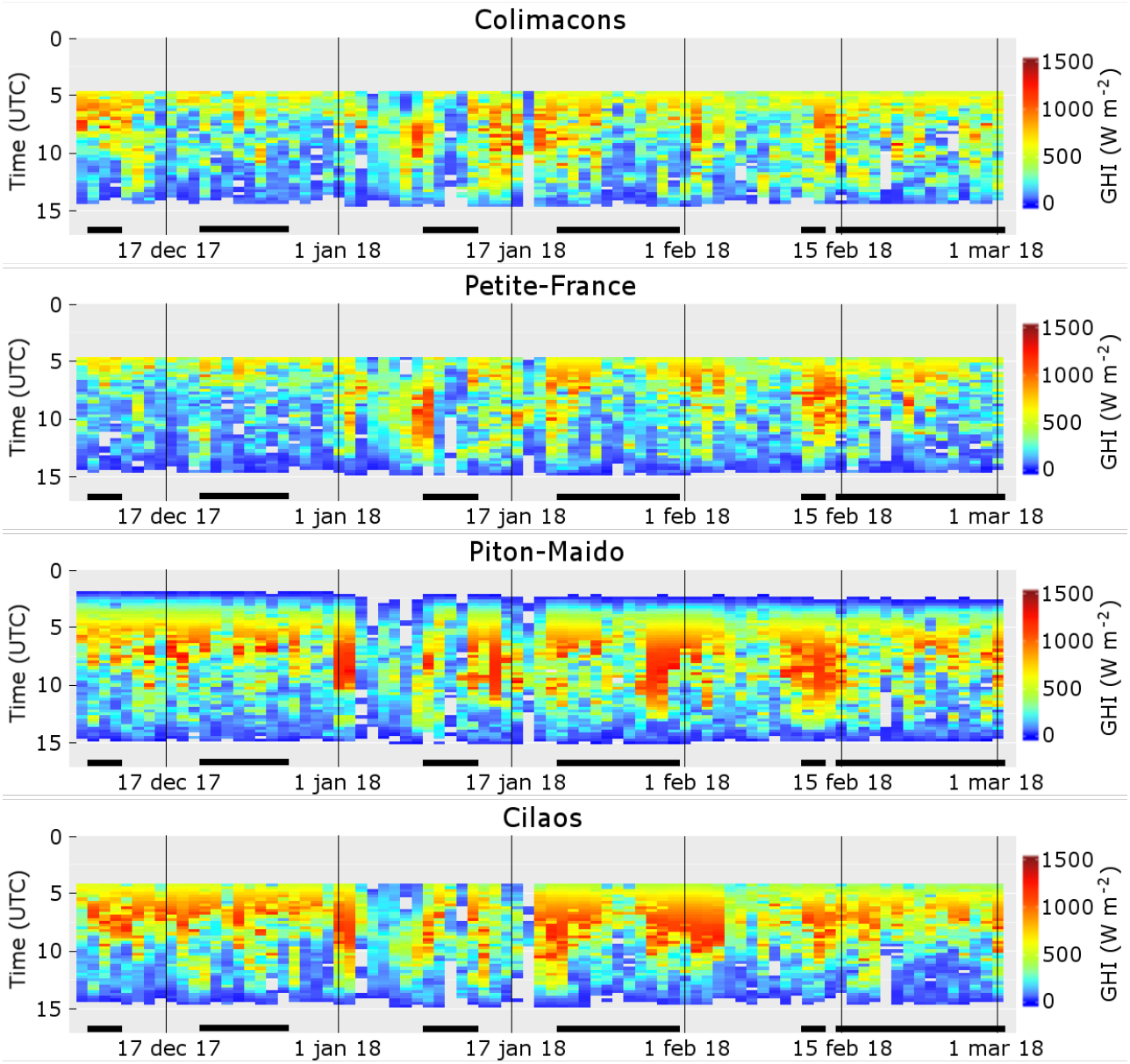

Figure A.2 – Same as figure A.1 but for four sites in the mountains: Colimacons, Petite-France, Piton-Maido, and Cilaos.

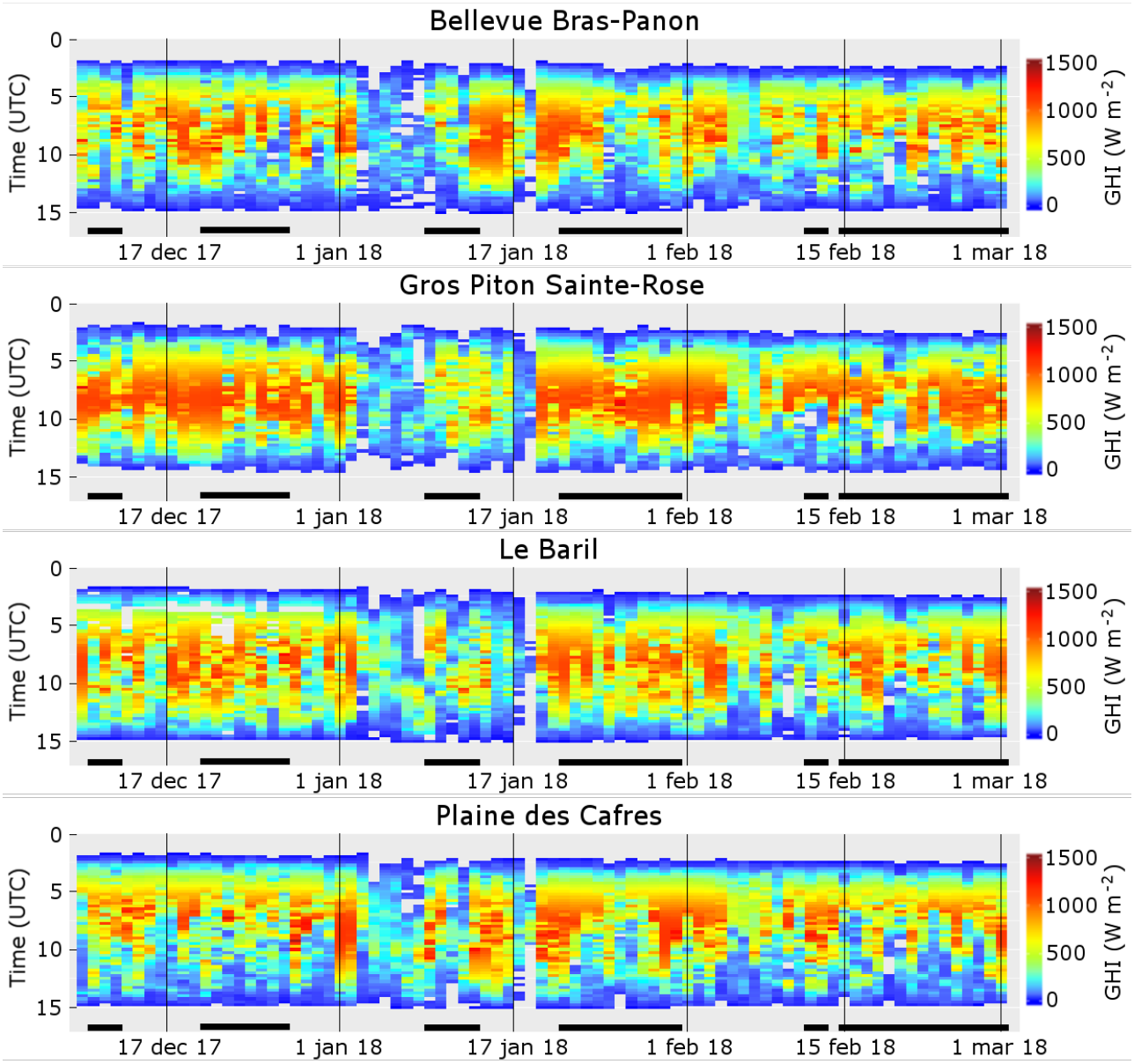

Figure A.3 – Same as figure A.1 but for the sites Bellevue Bras-Panon, Gros Piton Sainte-Rose, Le Baril, and Plaine des Cafres.

Bibliography

Abuella, M. and Chowdhury, B. (2018). Forecasting of solar power ramp events: A post-processing approach. *Renewable Energy*. doi:10.1016/j.renene.2018.09.005. (Cited on page 71.)

Albers, S. C., McGinley, J. A., Birkenheuer, D. L., and Smart, J. R. (1996). The Local Analysis and Prediction System (LAPS): Analyses of Clouds, Precipitation, and Temperature. *Wea. Forecasting*, 11(3):273–287. doi:10.1175/1520-0434(1996)011<0273:TLAAPS>2.0.CO;2. (Cited on page 40.)

Anderson, J., Hoar, T., Raeder, K., Liu, H., Collins, N., Torn, R., and Avellano, A. (2009). The Data Assimilation Research Testbed: A Community Facility. *B. Am. Meteorol. Soc.*, 90(9):1283–1296. doi:10.1175/2009BAMS2618.1. (Cited on page 36.)

Anderson, J. L. (2001). An Ensemble Adjustment Kalman Filter for Data Assimilation. *Mon. Wea. Rev.*, 129(12):2884–2903. doi:10.1175/1520-0493(2001)129<2884:AEAKFF>2.0.CO;2. (Cited on page 60.)

Anderson, J. L. (2007). An adaptive covariance inflation error correction algorithm for ensemble filters. *Tellus A*, 59(2):210–224. doi:10.1111/j.1600-0870.2006.00216.x. (Cited on page 59.)

Anderson, J. L. (2009). Spatially and temporally varying adaptive covariance inflation for ensemble filters. *Tellus A*, 61(1):72–83. doi:10.1111/j.1600-0870.2008.00361.x. (Cited on page 59.)

Aryaputera, A. W., Yang, D., and Walsh, W. M. (2015). Day-Ahead Solar Irradiance Forecasting in a Tropical Environment. *J. Sol. Energy Eng*, 137(5):051009. doi:10.1115/1.4030231. (Cited on page 11.)

Auligné, T. (2014a). Multivariate Minimum Residual Method for Cloud Retrieval. Part I: Theoretical Aspects and Simulated Observation Experiments. *Mon. Wea. Rev.*, 142(12):4383–4398. doi:10.1175/MWR-D-13-00172.1. (Cited on page 44.)

Auligné, T. (2014b). Multivariate Minimum Residual Method for Cloud Retrieval. Part II: Real Observations Experiments. *Mon. Wea. Rev.*, 142(12):4399–4415. doi:10.1175/MWR-D-13-00173.1. (Cited on page 44.)

Badosa, J., Haeffelin, M., and Chepfer, H. (2013). Scales of spatial and temporal variation of solar irradiance on Reunion tropical island. *Sol. Energy*, 88:42–56. doi:10.1016/j.solener.2012.11.007. (Cited on page 92.)

Badosa, J., Haeffelin, M., Kalecinski, N., Bonnardot, F., and Jumaux, G. (2015). Reliability of day-ahead solar irradiance forecasts on Reunion Island depending on synoptic wind and humidity conditions. *Sol. Energy*, 115:306–321. doi:10.1016/j.solener.2015.02.039. (Cited on pages 11 and 81.)

Bannister, R. N. (2017). A review of operational methods of variational and ensemble-variational data assimilation. *Q.J.R. Meteorol. Soc.*, 143(703):607–633. doi:10.1002/qj.2982. (Cited on page 25.)

Barker, D., Huang, X.-Y., Liu, Z., Auligné, T., Zhang, X., Rugg, S., Ajjaji, R., Bourgeois, A., Bray, J., Chen, Y., Demirtas, M., Guo, Y.-R., Henderson, T., Huang, W., Lin, H.-C., Michalakes, J., Rizvi, S., and Zhang, X. (2012). The Weather Research and Forecasting Model's Community Variational/Ensemble Data Assimilation System: WRFDA. *B. Am. Meteorol. Soc.*, 93(6):831–843. doi:10.1175/BAMS-D-11-00167.1. (Cited on pages 29 and 57.)

Bauer, P., Auligné, T., Bell, W., Geer, A., Guidard, V., Heilliette, S., Kazumori, M., Kim, M.-J., Liu, E. H.-C., McNally, A. P., Macpherson, B., Okamoto, K., Renshaw, R., and Riishøjgaard, L.-P. (2011a). Satellite cloud and precipitation assimilation at operational NWP centres. *Q.J.R. Meteorol. Soc.*, 137(661):1934–1951. doi:10.1002/qj.905. (Cited on pages 30, 31, 47 and 48.)

Bauer, P., Ohring, G., Kummerow, C., and Auligne, T. (2011b). Assimilating Satellite Observations of Clouds and Precipitation into NWP Models. *Bull. Amer. Meteor. Soc.*, 92(6):ES25–ES28. doi:10.1175/2011BAMS3182.1. (Cited on pages 20, 28, 31, 32 and 48.)

Bayler, G. M., Aune, R. M., and Raymond, W. H. (2000). NWP Cloud Initialization Using GOES Sounder Data and Improved Modeling of Non-precipitating Clouds. *Mon. Wea. Rev.*, 128(11):3911–3920. doi:10.1175/1520-0493(2001)129<3911:NCIUGS>2.0.CO;2. (Cited on pages 43 and 48.)

Bengtsson, L., Steinheimer, M., Bechtold, P., and Geleyn, J.-F. (2013). A stochastic parametrization for deep convection using cellular automata. *Q.J.R. Meteorol. Soc.*, 139(675):1533–1543. doi:10.1002/qj.2108. (Cited on page 49.)

Benjamin, S., Alexander, C., Weygandt, S., Dowell, D., Hu, M., Alcott, T., Smirnova, T., Olson, J., Brown, J., James, E., and Kenyon, J. (2016a). Improvements in HRRRv2/RAPv3 for Aug 2016 Implementation at NCEP for More Accurate Warm-Season and Cold-Season NWP. Technical report, NOAA Earth System Research Laboratory, Boulder, CO. (Cited on page 51.)

Benjamin, S. G., Dévényi, D., Weygandt, S. S., Brundage, K. J., Brown, J. M., Grell, G. A., Kim, D., Schwartz, B. E., Smirnova, T. G., Smith, T. L., and Manikin, G. S. (2004). An Hourly Assimilation–Forecast Cycle: The RUC. *Mon. Wea. Rev.*, 132(2):495–518. doi:10.1175/1520-0493(2004)132<0495:AHACTR>2.0.CO;2. (Cited on page 50.)

Benjamin, S. G., Weygandt, S. S., Brown, J. M., Hu, M., Alexander, C. R., Smirnova, T. G., Olson, J. B., James, E. P., Dowell, D. C., Grell, G. A., Lin, H., Peckham, S. E., Smith, T. L., Moninger, W. R., Kenyon, J. S., and Manikin, G. S. (2016b). A North American Hourly Assimilation and Model Forecast Cycle: The Rapid Refresh. *Mon. Wea. Rev.*, 144(4):1669–1694. doi:10.1175/MWR-D-15-0242.1. (Cited on page 50.)

Bennartz, R. and Greenwald, T. (2011). Current problems in scattering radiative transfer modelling for data assimilation. *Q.J.R. Meteorol. Soc.*, 137(661):1952–1962. doi:10.1002/qj.953. (Cited on page 31.)

Bessafi, M., Mihailović, D., Malinović-Milićević, S., Mihailović, A., Jumaux, G., Bonnardot, F., Fanchette, Y., and Chabriat, J.-P. (2018). Spatial and Temporal

Non-Linear Dynamics Analysis and Predictability of Solar Radiation Time Series for La Reunion Island (France). *Entropy*, 20(12):946. doi:10.3390/e20120946. (Cited on pages 2 and 92.)

Beucher, F. (2010). *Météorologie tropicale : des alizés au cyclone*. Météo-France, Ecole Nationale de la Météorologie, Paris, Toulouse. (Cited on page 10.)

Blaga, R., Sabadus, A., Stefu, N., Dughir, C., Paulescu, M., and Badescu, V. (2019). A current perspective on the accuracy of incoming solar energy forecasting. *Progress in Energy and Combustion Science*, 70:119–144. doi:10.1016/j.pecs.2018.10.003. (Cited on page 10.)

Blanco, J. and Malato, S. (2009). *Solar Energy Conversion And Photoenergy System - Volume I*. EOLSS Publications. (Cited on page 5.)

Brousseau, P., Seity, Y., Ricard, D., and Léger, J. (2016). Improvement of the forecast of convective activity from the AROME-France system. *Q.J.R. Meteorol. Soc.*, 142(699):2231–2243. doi:10.1002/qj.2822. (Cited on page 51.)

Chen, Y., Wang, H., Min, J., Huang, X.-Y., Minnis, P., Zhang, R., Haggerty, J., and Palikonda, R. (2015). Variational Assimilation of Cloud Liquid/Ice Water Path and Its Impact on NWP. *J. Appl. Meteor. Climatol.*, 54(8):1809–1825. doi:10.1175/JAMC-D-14-0243.1. (Cited on pages 42, 43, 45, 46, 47 and 48.)

Chen, Y., Zhang, R., Meng, D., Min, J., and Zhang, L. (2016). Variational assimilation of satellite cloud water/ice path and microphysics scheme sensitivity to the assimilation of a rainfall case. *Adv. Atmos. Sci.*, 33(10):1158–1170. doi:10.1007/s00376-016-6004-3. (Cited on pages 43, 45, 46, 47 and 48.)

Cintineo, R., Otkin, J. A., Xue, M., and Kong, F. (2014). Evaluating the Performance of Planetary Boundary Layer and Cloud Microphysical Parameterization Schemes in Convection-Permitting Ensemble Forecasts Using Synthetic GOES-13 Satellite Observations. *Mon. Wea. Rev.*, 142(1):163–182. doi:10.1175/MWR-D-13-00143.1. (Cited on pages 9 and 10.)

Cintineo, R. M., Otkin, J. A., Jones, T. A., Koch, S., and Stensrud, D. J. (2016). Assimilation of Synthetic GOES-R ABI Infrared Brightness Temperatures and WSR-88d Radar Observations in a High-Resolution OSSE. *Mon. Wea. Rev.*, 144(9):3159–3180. doi:10.1175/MWR-D-15-0366.1. (Cited on page 36.)

Collard, A. (2017). Radiance Assimilation at NOAA/NCEP/EMC. CWB Visit. Boulder, CO. (Cited on page 59.)

Copernicus (2019). Seasonal forecasts. Available at https://climate.copernicus.eu/seasonal-forecasts. Accessed 29 January 2019. (Cited on page 8.)

CRE (2014). Recommandation de la CRE no 40 du 12 juin 2014 (R. 2014-40). (Cited on page 3.)

CRE (2018). Propositions de la CRE relatives aux zones non interconnectées. (Cited on page 2.)

Cros, S., Turpin, M., Lallemand, C., and Guérin, A. (2018). Solar irradiance and variability forecasting using Himawari-8 satellite images. 5th International Conference Energy & Meteorology, Shanghai, China. (Cited on page 6.)

DARC (2016). Introduction to data assimilation. Data Assimilation Research Centre (DARC), University of Reading, Reading, UK. (Cited on page 21.)

de Haan, S. and van der Veen, S. H. (2014). Cloud Initialization in the Rapid Update Cycle of HIRLAM. *Wea. Forecasting*, 29(5):1120–1133. doi:10.1175/WAF-D-13-00071.1. (Cited on pages 41 and 49.)

DEAL-Réunion (2017). Révision de la programmation pluriannuelle de l'énergie (PPE) de la Réunion - période 2019 – 2028. Direction de l'Environnementde l'Aménagement et du Logement de La Réunion. Available at http://www.reunion.developpement-durable.gouv.fr/revision-de-la-programmation-pluriannuelle-de-l-a704.html. Accessed 8 January 2019. (Cited on page 3.)

Derrien, M. and Le Gléau, H. (2005). MSG/SEVIRI cloud mask and type from SAFNWC. *Int. J. Remote Sens.*, 26(21):4707–4732. doi:10.1080/01431160500166128. (Cited on page 14.)

Descombes, G., Auligné, T., Lin, H.-C., Xu, D., Schwartz, C., and Vandenberghe, F. (2014). Multi-sensor Advection Diffusion nowCast (MADCast) for cloud analysis and short-term prediction. NCAR Technical Note NCAR/TN-509+STR. (Cited on page 44.)

Diagne, M., David, M., Boland, J., Schmutz, N., and Lauret, P. (2014). Post-processing of solar irradiance forecasts from WRF model at Reunion Island. *Sol. Energy*, 105:99–108. doi:10.1016/j.solener.2014.03.016. (Cited on page 11.)

Diagne, M., David, M., Lauret, P., Boland, J., and Schmutz, N. (2013). Review of solar irradiance forecasting methods and a proposition for small-scale insular grids. *Renew. Sust. Energ. Rev.*, 27:65–76. doi:10.1016/j.rser.2013.06.042. (Cited on pages 6 and 9.)

Dillon, M. E., Skabar, Y. G., Ruiz, J., Kalnay, E., Collini, E. A., Echevarría, P., Saucedo, M., Miyoshi, T., and Kunii, M. (2016). Application of the WRF-LETKF Data Assimilation System over Southern South America: Sensitivity to Model Physics. *Weather Forecast.*, 31(1):217–236. doi:10.1175/WAF-D-14-00157.1. (Cited on page 57.)

Dudhia, J. (1989). Numerical Study of Convection Observed during the Winter Monsoon Experiment Using a Mesoscale Two-Dimensional Model. *J. Atmos. Sci.*, 46(20):3077–3107. doi:10.1175/1520-0469(1989)046<3077:NSOCOD>2.0.CO;2. (Cited on page 57.)

ECMWF (2016). Training course on data assimilation, Reading, UK. (Cited on pages 21 and 23.)

Errico, R. M., Bauer, P., and Mahfouf, J.-F. (2007a). Issues Regarding the Assimilation of Cloud and Precipitation Data. *J. Atmos. Sci.*, 64(11):3785–3798. doi:10.1175/2006JAS2044.1. (Cited on pages 31 and 44.)

Errico, R. M., Fillion, L., Nychka, D., and Lu, Z.-Q. (2000). Some statistical considerations associated with the data assimilation of precipitation observations. *Q.J.R. Meteorol. Soc.*, 126(562):339–359. doi:10.1002/qj.49712656217. (Cited on page 31.)

Errico, R. M., Ohring, G., Weng, F., Bauer, P., Ferrier, B., Mahfouf, J.-F., and Turk, J. (2007b). Assimilation of Satellite Cloud and Precipitation Observations in Numerical Weather Prediction Models: Introduction to the JAS Special Collection. *J. Atmos. Sci.*, 64(11):3737–3741. doi:10.1175/2007JAS2622.1. (Cited on page 49.)

Espinar, B., Blanc, P., Wald, L., Hoyer-Klick, C., Homscheidt, M. S., and Wanderer, T. (2012). On quality control procedures for solar radiation and meteorological measures, from subhourly to monthly average time periods. EGU General Assembly, Vienna, Austria, 22-27 April 2012. (Cited on page 70.)

Evensen, G. (1994). Sequential data assimilation with a nonlinear quasi-geostrophic model using Monte Carlo methods to forecast error statistics. *J. Geophys. Res.*, 99(C5):10143–10162. doi:10.1029/94JC00572. (Cited on page 24.)

Fisher, M. (2003). Background error covariance modelling. Proceedings of the ECMWF Seminar on recent developments in data assimilation for atmosphere and ocean, , 8–12 September 2003, ECMWF, Reading, UK. (Cited on page 23.)

Fox, B., Flynn, D., Bryans, L., Jenkins, N., Milborrow, D., O'Malley, M., Watson, R., and Anaya-Lara, O. (2007). *Wind Power Integration: Connection and System Operational Aspects*. IET. (Cited on page 3.)

Galvin, J. F. P. (2016). *An Introduction to the Meteorology and Climate of the Tropics*. Wiley. (Cited on page 10.)

Gaspari, G. and Cohn, S. E. (1999). Construction of correlation functions in two and three dimensions. *Q. J. Roy. Meteor. Soc.*, 125(554):723–757. doi:10.1002/qj.49712555417. (Cited on pages 25 and 64.)

Geer, A. J. and Bauer, P. (2011). Observation errors in all-sky data assimilation. *Q.J.R. Meteorol. Soc.*, 137(661):2024–2037. doi:10.1002/qj.830. (Cited on page 34.)

Geer, A. J., Lonitz, K., Weston, P., Kazumori, M., Okamoto, K., Zhu, Y., Liu, E. H., Collard, A., Bell, W., Migliorini, S., Chambon, P., Fourrié, N., Kim, M.-J., Köpken-Watts, C., and Schraff, C. (2017). All-sky satellite data assimilation at operational weather forecasting centres. *Q.J.R. Meteorol. Soc.* doi:10.1002/qj.3202. (Cited on pages 11, 28, 30 and 32.)

Ghil, M. and Malanotte-Rizzoli, P. (1991). Data Assimilation in Meteorology and Oceanography. In *Advances in Geophysics*, volume 33, pages 141–266. Elsevier. doi:10.1016/S0065-2687(08)60442-2. (Cited on page 24.)

Greenwald, T. J., Hertenstein, R., and Vukićević, T. (2002). An All-Weather Observational Operator for Radiance Data Assimilation with Mesoscale Forecast Models. *Mon. Wea. Rev.*, 130(7):1882–1897. doi:10.1175/1520-0493(2002)130<1882:AAWOOF>2.0.CO;2. (Cited on page 32.)

Greenwald, T. J., Vukićević, T., Grasso, L. D., and Vonder Haar, T. H. (2004). Adjoint sensitivity analysis of an observational operator for visible and infrared cloudy-sky radiance assimilation. *Q.J.R. Meteorol. Soc.*, 130(597):685–705. doi:10.1256/qj.03.44. (Cited on page 32.)

Guidard, V., Fischer, C., Nuret, M., and Džiedžic, A. (2006). Evaluation of the ALADIN 3d-VAR with observations of the MAP campaign. *Meteorol. Atmos. Phys.*, 92(3-4):161–173. doi:10.1007/s00703-005-0156-5. (Cited on pages 41, 42 and 43.)

Guidard, V. and Fourrié, N. (2010). Status of cloudy infrared radiance assimilation at Météo-France. Proceedings of the ECMWF-JCSDA Workshop on Assimilating Satellite Observations of Clouds and Precipitation into NWP Models, ECMWF, Reading, UK. European Centre for Medium-Range Weather Forecasts. (Cited on page 51.)

Gustafsson, N., Berre, L., Hornquist, S., Huang, X.-Y., Lindskog, M., Navascues, B., Mogensen, K. S., and Thorsteinsson, S. (2001). Three-dimensional variational data assimilation for a limited area model. Part I: General formulation and the background error constraint. *Tellus A*, 53(4):425–446. doi:10.1111/j.1600-0870.2001.00425.x. (Cited on page 32.)

Gustafsson, N., Janjić, T., Schraff, C., Leuenberger, D., Weissmann, M., Reich, H., Brousseau, P., Montmerle, T., Wattrelot, E., Bučánek, A., Mile, M., Hamdi, R., Lindskog, M., Barkmeijer, J., Dahlbom, M., Macpherson, B., Ballard, S., Inverarity, G., Carley, J., Alexander, C., Dowell, D., Liu, S., Ikuta, Y., and Fujita, T. (2018). Survey of data assimilation methods for convective-scale numerical weather prediction at operational centres. *Q.J.R. Meteorol. Soc.* doi:10.1002/qj.3179. (Cited on pages 12, 20, 48 and 50.)

Haiden, T. and Trentmann, J. (2015). Verification of cloudiness and radiation forecasts in the greater Alpine region. *Meteorol. Z.*, 25(1):3–15. doi:10.1127/metz/2015/0630. (Cited on page 9.)

Hamill, T. M., Whitaker, J. S., and Snyder, C. (2001). Distance-Dependent Filtering of Background Error Covariance Estimates in an Ensemble Kalman Filter. *Mon. Wea. Rev.*, 129(11):2776–2790. doi:10.1175/1520-0493(2001)129<2776:DDFOBE>2.0.CO;2. (Cited on page 25.)

Han, Y., van Delst, P., Liu, Q., Weng, F., Treadon, R., and Derber, J. (2006). JCSDA Community Radiative Transfer Model (CRTM) : version 1. Technical Report NOAA Tech. Rep. NESDIS 122. (Cited on page 37.)

Harnisch, F., Weissmann, M., and Periáñez, . (2016). Error model for the assimilation of cloud-affected infrared satellite observations in an ensemble data assimilation system. *Q.J.R. Meteorol. Soc.*, 142(697):1797–1808. doi:10.1002/qj.2776. (Cited on pages 26, 33 and 34.)

Hohenegger, C. and Schär, C. (2007). Predictability and Error Growth Dynamics in Cloud-Resolving Models. *J. Atmos. Sci.*, 64(12):4467–4478. doi:10.1175/2007JAS2143.1. (Cited on pages 48 and 56.)

Hollingsworth, A. and Lönnberg, P. (1986). The statistical structure of short-range forecast errors as determined from radiosonde data. Part I: The wind field. *Tellus A*, 38A(2):111–136. doi:10.1111/j.1600-0870.1986.tb00460.x. (Cited on page 23.)

Honda, T., Kotsuki, S., Lien, G.-Y., Maejima, Y., Okamoto, K., and Miyoshi, T. (2018a). Assimilation of Himawari-8 All-Sky Radiances Every 10 Minutes:

Impact on Precipitation and Flood Risk Prediction. *J. Geophys. Res.-Atmos.*, 123(2):965–976. doi:10.1002/2017JD027096. (Cited on page 37.)

Honda, T., Miyoshi, T., Lien, G.-Y., Nishizawa, S., Yoshida, R., Adachi, S. A., Terasaki, K., Okamoto, K., Tomita, H., and Bessho, K. (2018b). Assimilating All-Sky Himawari-8 Satellite Infrared Radiances: A Case of Typhoon Soudelor (2015). *Mon. Wea. Rev.*, 146(1):213–229. doi:10.1175/MWR-D-16-0357.1. (Cited on page 37.)

Houtekamer, P. L. and Mitchell, H. L. (2001). A Sequential Ensemble Kalman Filter for Atmospheric Data Assimilation. *Mon. Wea. Rev.*, 129(1):123–137. doi:10.1175/1520-0493(2001)129<0123:ASEKFF>2.0.CO;2. (Cited on page 25.)

Houtekamer, P. L. and Zhang, F. (2016). Review of the Ensemble Kalman Filter for Atmospheric Data Assimilation. *Mon. Wea. Rev.*, 144(12):4489–4532. doi:10.1175/MWR-D-15-0440.1. (Cited on page 25.)

Hu, M., Weyg, S., Xue, M., and Benjamin, S. (2007). Development and Testing of a New Cloud Analysis Package using Radar, Satellite, and Surface Cloud Observations within GSI for Initializing Rapid Refresh. Proceedings of the 18th Conference on Numerical Weather Prediction, Park City, UT, USA. American Meteorological Society. (Cited on page 50.)

Inman, R. H., Pedro, H. T., and Coimbra, C. F. (2013). Solar forecasting methods for renewable energy integration. *Prog. Energ. Combust.*, 39(6):535–576. doi:10.1016/j.pecs.2013.06.002. (Cited on page 9.)

Jimenez, P. A., Hacker, J. P., Dudhia, J., Ellen Haupt, S., Ruiz-Arias, J. A., Gueymard, C. A., Thompson, G., Eidhammer, T., and Deng, A. (2016). WRF-Solar: Description and Clear-Sky Assessment of an Augmented NWP Model for Solar Power Prediction. *Bull. Amer. Meteor. Soc.*, 97(7):1249–1264. doi:10.1175/BAMS-D-14-00279.1. (Cited on page 9.)

Jolliffe, I. T. and Stephenson, D. B., editors (2012). *Forecast verification: a practitioner's guide in atmospheric science*. Wiley-Blackwell, Chichester, 2. ed edition. (Cited on page 25.)

Jones, T. A., Koch, S., and Li, Z. (2017). Assimilating synthetic hyperspectral sounder temperature and humidity retrievals to improve severe weather forecasts. *Atmospheric Research*, 186(Supplement C):9–25. doi:10.1016/j.atmosres.2016.11.004. (Cited on page 36.)

Jones, T. A., Otkin, J. A., Stensrud, D. J., and Knopfmeier, K. (2013a). Assimilation of Satellite Infrared Radiances and Doppler Radar Observations during a Cool Season Observing System Simulation Experiment. *Mon. Wea. Rev.*, 141(10):3273–3299. doi:10.1175/MWR-D-12-00267.1. (Cited on pages 36 and 67.)

Jones, T. A., Otkin, J. A., Stensrud, D. J., and Knopfmeier, K. (2014). Forecast Evaluation of an Observing System Simulation Experiment Assimilating Both Radar and Satellite Data. *Mon. Wea. Rev.*, 142(1):107–124. doi:10.1175/MWR-D-13-00151.1. (Cited on page 36.)

Jones, T. A., Stensrud, D., Wicker, L., Minnis, P., and Palikonda, R. (2015). Simultaneous Radar and Satellite Data Storm-Scale Assimilation Using an Ensemble Kalman Filter Approach for 24 May 2011. *Mon. Wea. Rev.*, 143(1):165–194. doi:10.1175/MWR-D-14-00180.1. (Cited on pages 45, 46, 60, 63, 64, 67 and 88.)

Jones, T. A., Stensrud, D. J., Minnis, P., and Palikonda, R. (2013b). Evaluation of a Forward Operator to Assimilate Cloud Water Path into WRF-DART. *Mon. Wea. Rev.*, 141(7):2272–2289. doi:10.1175/MWR-D-12-00238.1. (Cited on pages 39, 44, 45, 46, 49, 53, 60, 64 and 88.)

Kain, J. S. (2004). The Kain–Fritsch Convective Parameterization: An Update. *J. Appl. Meteorol.*, 43(1):170–181. doi:10.1175/1520-0450(2004)043<0170:TKCPAU>2.0.CO;2. (Cited on page 57.)

Kalnay, E. (2003). *Atmospheric Modeling, Data Assimilation, and Predictability*. Cambridge University Press, New York. (Cited on pages 7, 8, 11, 12, 13, 21 and 25.)

Kalnay, E., Li, H., Miyoshi, T., Yang, S.-C., and Ballabrera-Poy, J. (2007). 4-D-Var or ensemble Kalman filter? *Tellus A*, 59(5):758–773. doi:10.1111/j.1600-0870.2007.00261.x. (Cited on page 25.)

Kleissl, J. (2013). *Solar Energy Forecasting and Resource Assessment*. Academic Press, 1 edition. (Cited on page 4.)

Kostka, P. M., Weissmann, M., Buras, R., Mayer, B., and Stiller, O. (2014). Observation Operator for Visible and Near-Infrared Satellite Reflectances. *J. Atmos. Oceanic Technol.*, 31(6):1216–1233. doi:10.1175/JTECH-D-13-00116.1. (Cited on pages 30, 31 and 33.)

Kumar, P. and Varma, A. K. (2016). Assimilation of INSAT-3d Hydro-Estimator Method Retrieved Rainfall for Short Range Weather Prediction. *Q.J.R. Meteorol. Soc.*, 143(702):384–394. doi:10.1002/qj.2929. (Cited on pages 43, 46, 47 and 49.)

Lahoz, W., Khattatov, B., and Menard, R., editors (2010). *Data Assimilation*. Springer Berlin Heidelberg, Berlin, Heidelberg. (Cited on pages 21 and 25.)

Lara-Fanego, V., Ruiz-Arias, J. A., Pozo-Vázquez, A. D., Gueymard, C. A., and Tovar-Pescador, J. (2012). Evaluation of DNI forecast based on the WRF mesoscale atmospheric model for CPV applications. In *AIP Conference Proceedings*, volume 1477, pages 317–322, 8th International Conference on Concentrating Photovoltaic Systems: CPV-8, Toledo, Spain, 16-18 April 2012. doi:10.1063/1.4753895. (Cited on pages 56 and 70.)

Lauret, P., Lorenz, E., and David, M. (2016). Solar Forecasting in a Challenging Insular Context. *Atmosphere*, 7(2):18. doi:10.3390/atmos7020018. (Cited on page 11.)

Lauwaet, D., De Ridder, K., and Pandey, P. (2011). Assimilating remotely sensed cloud optical thickness into a mesoscale model. *Atmos. Chem. Phys.*, 11(19):10269–10281. doi:10.5194/acp-11-10269-2011. (Cited on pages 11, 42 and 44.)

Lenfle, S. (2018). De l'interpolation optimale au 4d-Var : l'émergence d'un nouveau dominant design en assimilation de données météorologiques. *La Météorologie*, (100 Spécial Anniversaire 25 ans):37. doi:10.4267/2042/65141. (Cited on pages 12, 20 and 21.)

Liandrat, O., Cros, S., Braun, A., Saint-Antonin, L., Decroix, J., and Schmutz, N. (2017). Cloud cover forecast from a ground-based all sky infrared thermal camera. In *Proc. SPIE 10424*, volume 104240B. doi:10.1117/12.2278636. (Cited on page 6.)

Lima, F. J. L., Martins, F. R., Pereira, E. B., Lorenz, E., and Heinemann, D. (2016). Forecast for surface solar irradiance at the Brazilian Northeastern region using NWP model and artificial neural networks. *Renewable Energy*, 87, Part 1:807–818. doi:10.1016/j.renene.2015.11.005. (Cited on page 11.)

Lindskog, M., Gustafsson, N., Navascues, B., Mogensen, K. S., Huang, X.-Y., Yang, X., Andrae, U., Berre, L., Thorsteinsson, S., and Rantakokko, J. (2001). Three-dimensional variational data assimilation for a limited area model. Part II: Observation handling and assimilation experiments. *Tellus A*, 53(4):447–468. doi:10.1111/j.1600-0870.2001.00447.x. (Cited on page 32.)

Lipton, A. E. (1993). Cloud Shading Retrieval and Assimilation in a Satellite-Model Coupled Mesoscale Analysis System. *Mon. Wea. Rev.*, 121(11):3062–3081. doi:10.1175/1520-0493(1993)121<3062:CSRAAI>2.0.CO;2. (Cited on page 39.)

Lipton, A. E. and Modica, G. D. (1999). Assimilation of Visible-Band Satellite Data for Mesoscale Forecasting in Cloudy Conditions. *Mon. Wea. Rev.*, 127(3):265–278. doi:10.1175/1520-0493(1999)127<0265:AOVBSD>2.0.CO;2. (Cited on page 48.)

Lipton, A. E. and Vonder Haar, T. H. (1990a). Mesoscale Analysis by Numerical Modeling Coupled with Sounding Retrieval from Satellites. *Mon. Wea. Rev.*, 118(6):1308–1329. doi:10.1175/1520-0493(1990)118<1308:MABNMC>2.0.CO;2. (Cited on page 39.)

Lipton, A. E. and Vonder Haar, T. H. (1990b). Preconvective Mesoscale Analysis over Irregular Terrain with a Satellite-Model Coupled System. *Mon. Wea. Rev.*, 118(6):1330–1358. doi:10.1175/1520-0493(1990)118<1330:PMAOIT>2.0.CO;2. (Cited on page 39.)

Lohmann, G. (2018). Irradiance Variability Quantification and Small-Scale Averaging in Space and Time: A Short Review. *Atmosphere*, 9(7):264. doi:10.3390/atmos9070264. (Cited on page 71.)

López-Coto, I., Bosch, J. L., Mathiesen, P., and Kleissl, J. (2013). Comparison between several parameterization schemes in WRF for solar forecasting in coastal zones. In *SOLAR Conference Proceedings*, 42nd ASES Annual Conference, Baltimore, Maryland, USA, 16-20 April 2013. (Cited on pages 9 and 10.)

Macpherson, B., Wright, B. J., Hand, W. H., and Maycock, A. J. (1996). The Impact of MOPS Moisture Data in the U.K. Meteorological Office Mesoscale Data Assimilation Scheme. *Mon. Wea. Rev.*, 124(8):1746–1766. doi:10.1175/1520-0493(1996)124<1746:TIOMMD>2.0.CO;2. (Cited on page 39.)

Mallet, P.-t., Pujol, O., Brioude, J., Evan, S., and Jensen, A. (2018). Marine aerosol distribution and variability over the pristine Southern Indian Ocean. *Atmospheric Environment*, 182:17–30. doi:10.1016/j.atmosenv.2018.03.016. (Cited on page 70.)

Marquez, R. and Coimbra, C. F. M. (2012). Proposed Metric for Evaluation of Solar Forecasting Models. *J. Sol. Energy Eng.*, 135(1):011016–011016. doi:10.1115/1.4007496. (Cited on page 71.)

Mass, C. F., Ovens, D., Westrick, K., and Colle, B. A. (2002). Does Increasing Horizontal Resolution Produce More Skillful Forecasts? *B. Am. Meteorol. Soc.*, 83(3):407–430. doi:10.1175/1520-0477(2002)083<0407:DIHRPM>2.3.CO;2. (Cited on page 56.)

Mathiesen, P., Collier, C., and Kleissl, J. (2013). A high-resolution, cloud-assimilating numerical weather prediction model for solar irradiance forecasting. *Sol. Energy*, 92:47–61. doi:10.1016/j.solener.2013.02.018. (Cited on pages 41, 42, 43 and 49.)

McNally, A. P. (2002). A note on the occurrence of cloud in meteorologically sensitive areas and the implications for advanced infrared sounders. *Q.J.R. Meteorol. Soc.*, 128(585):2551–2556. doi:10.1256/qj.01.206. (Cited on page 14.)

McNider, R. T., Song, J. A., and Kidder, S. Q. (1995). Assimilation of GOES-derived solar insolation into a mesoscale model for studies of cloud shading effects. *Int. J. Remote Sens.*, 16(12):2207–2231. doi:10.1080/01431169508954552. (Cited on page 39.)

Migliorini, S. (2012). On the Equivalence between Radiance and Retrieval Assimilation. *Mon. Wea. Rev.*, 140(1):258–265. doi:10.1175/MWR-D-10-05047.1. (Cited on pages 28 and 32.)

Migliorini, S., Piccolo, C., and Rodgers, C. D. (2008). Use of the Information Content in Satellite Measurements for an Efficient Interface to Data Assimilation. *Mon. Wea. Rev.*, 136(7):2633–2650. doi:10.1175/2007MWR2236.1. (Cited on page 49.)

Minamide, M. and Zhang, F. (2017). Adaptive Observation Error Inflation for Assimilating All-Sky Satellite Radiance. *Mon. Wea. Rev.*, 145(3):1063–1081. doi:10.1175/MWR-D-16-0257.1. (Cited on page 36.)

Minamide, M. and Zhang, F. (2018). Assimilation of All-sky Infrared Radiances from Himawari-8 and Impacts of Moisture and Hydrometer Initialization on Convection-Permitting Tropical Cyclone Prediction. *Mon. Wea. Rev.* doi:10.1175/MWR-D-17-0367.1. (Cited on page 37.)

Minamide, M. and Zhang, F. (2019). An adaptive background error inflation method for assimilating all-sky radiances. *Q.J.R. Meteorol. Soc.* doi:10.1002/qj.3466. (Cited on page 36.)

Minnis, P., Bedka, K., Trepte, Q., Yost, C. R., Bedka, S. T., Scarino, B., Khlopenkov, K., and Khaiyer, M. M. (2016). A consistent long-term cloud and clear-sky radiation property dataset from the Advanced Very High Resolution

Radiometer (AVHRR). Technical Report NOAA CDR Program, 19 September, 159 pp. doi:10.789/V5HT2M8T. (Cited on pages 43 and 61.)

Minnis, P., Nguyen, L., Palikonda, R., Heck, P. W., Spangenberg, D. A., Doelling, D. R., Ayers, J. K., Smith, Jr., W. L., Khaiyer, M. M., Trepte, Q. Z., Avey, L. A., Chang, F.-L., Yost, C. R., Chee, T. L., and Szedung, S.-M. (2008). Near-real time cloud retrievals from operational and research meteorological satellites. In *Proceedings Volume 7107, Remote Sensing of Clouds and the Atmosphere XIII*, page 710703, Cardiff, Wales, UK, 15-18 September 2008. doi:10.1117/12.800344. (Cited on pages 14, 43 and 61.)

Minnis, P., Sun-Mack, S., Young, D. F., Heck, P. W., Garber, D. P., Chen, Y., Spangenberg, D. A., Arduini, R. F., Trepte, Q. Z., Smith, W. L., Ayers, J. K., Gibson, S. C., Miller, W. F., Hong, G., Chakrapani, V., Takano, Y., Liou, K.-N., Xie, Y., and Yang, P. (2011). CERES Edition-2 Cloud Property Retrievals Using TRMM VIRS and Terra and Aqua MODIS Data, Part I: Algorithms. *IEEE T. Geosci. Remote*, 49(11):4374–4400. doi:10.1109/TGRS.2011.2144601. (Cited on page 61.)

Météo-France (2017). Le modèle AROME outre-mer. Available at meteofrance.fr. Accessed 19 March 2019. Technical report. (Cited on page 72.)

NOAA/NCEI (2017). Rapid Refresh (RAP). Available at https://www.ncdc.noaa.gov/data-access/model-data/model-datasets/rapid-refresh-rap. Accessed 8 January 2019. (Cited on page 50.)

Okamoto, K. (2017). Evaluation of IR radiance simulation for all-sky assimilation of Himawari-8/AHI in a mesoscale NWP system: Evaluation of All-Sky IR Radiance of Himawari-8. *Q.J.R. Meteorol. Soc.*, 143(704):1517–1527. doi:10.1002/qj.3022. (Cited on page 37.)

Otkin, J. A. (2010). Clear and cloudy sky infrared brightness temperature assimilation using an ensemble Kalman filter. *J. Geophys. Res.-Atmos.*, 115(D19):D19207. doi:10.1029/2009JD013759. (Cited on pages 30, 31, 36 and 45.)

Otkin, J. A. (2012a). Assessing the impact of the covariance localization radius when assimilating infrared brightness temperature observations using an ensemble Kalman filter. *Mon. Wea. Rev.*, 140(2):543–561. doi:10.1175/MWR-D-11-00084.1. (Cited on pages 36 and 80.)

Otkin, J. A. (2012b). Assimilation of water vapor sensitive infrared brightness temperature observations during a high impact weather event. *J. Geophys. Res.-Atmos.*, 117(D19):D19203. doi:10.1029/2012JD017568. (Cited on page 36.)

Otkin, J. A. and Greenwald, T. J. (2008). Comparison of WRF Model-Simulated and MODIS-Derived Cloud Data. *Mon. Wea. Rev.*, 136(6):1957–1970. doi:10.1175/2007MWR2293.1. (Cited on page 10.)

Otkin, J. A., Lewis, W. E., Lenzen, A. J., McNoldy, B. D., and Majumdar, S. J. (2017). Assessing the Accuracy of the Cloud and Water Vapor Fields in the Hurricane WRF (HWRF) Model Using Satellite Infrared Brightness Temperatures.

Mon. Wea. Rev., 145(5):2027–2046. doi:10.1175/MWR-D-16-0354.1. (Cited on page 10.)

Otkin, J. A., Potthast, R., and Lawless, A. (2018). Nonlinear bias correction for satellite data assimilation using Taylor series polynomials. *Mon. Wea. Rev.* doi:10.1175/MWR-D-17-0171.1. (Cited on pages 31 and 34.)

Pan, Y., Xue, M., Zhu, K., and Wang, M. (2018). A Prototype Regional GSI-based EnKF-Variational Hybrid Data Assimilation System for the Rapid Refresh Forecasting System: Dual-Resolution Implementation and Testing Results. *Adv. Atmos. Sci.*, 35(5):518–530. doi:10.1007/s00376-017-7108-0. (Cited on page 50.)

Pan, Y., Zhu, K., Xue, M., Wang, X., Hu, M., Benjamin, S. G., Weygandt, S. S., and Whitaker, J. S. (2014). A GSI-Based Coupled EnSRF–En3dvar Hybrid Data Assimilation System for the Operational Rapid Refresh Model: Tests at a Reduced Resolution. *Mon. Wea. Rev.*, 142(10):3756–3780. doi:10.1175/MWR-D-13-00242.1. (Cited on page 57.)

Parrish, D. F. and Derber, J. C. (1992). The National Meteorological Center's Spectral Statistical-Interpolation Analysis System. *Mon. Wea. Rev.*, 120(8):1747–1763. doi:10.1175/1520-0493(1992)120<1747:TNMCSS>2.0.CO;2. (Cited on pages 23 and 57.)

Pincus, R., Patrick Hofmann, R. J., Anderson, J. L., Raeder, K., Collins, N., and Whitaker, J. S. (2011). Can Fully Accounting for Clouds in Data Assimilation Improve Short-Term Forecasts by Global Models? *Mon. Wea. Rev.*, 139(3):946–957. doi:10.1175/2010MWR3412.1. (Cited on page 14.)

Polkinghorne, R. and Vukicevic, T. (2011). Data Assimilation of Cloud-Affected Radiances in a Cloud-Resolving Model. *Mon. Wea. Rev.*, 139(3):755–773. doi:10.1175/2010MWR3360.1. (Cited on pages 30, 31, 34, 36 and 49.)

Polkinghorne, R., Vukicevic, T., and Evans, K. F. (2010). Validation of Cloud-Resolving Model Background Data for Cloud Data Assimilation. *Mon. Wea. Rev.*, 138(3):781–795. doi:10.1175/2009MWR3012.1. (Cited on pages 34 and 36.)

Praene, J. P., David, M., Sinama, F., Morau, D., and Marc, O. (2012). Renewable energy: Progressing towards a net zero energy island, the case of Reunion Island. *Renewable and Sustainable Energy Reviews*, 16(1):426–442. doi:10.1016/j.rser.2011.08.007. (Cited on page 3.)

Pérez, J. C., Díaz, J. P., González, A., Expósito, J., Rivera-López, F., and Taima, D. (2014). Evaluation of WRF Parameterizations for Dynamical Downscaling in the Canary Islands. *J. Climate*, 27(14):5611–5631. doi:10.1175/JCLI-D-13-00458.1. (Cited on page 9.)

Qin, Z., Zou, X., and Weng, F. (2013). Evaluating Added Benefits of Assimilating GOES Imager Radiance Data in GSI for Coastal QPFs. *Mon. Wea. Rev.*, 141(1):75–92. doi:10.1175/MWR-D-12-00079.1. (Cited on pages 29 and 30.)

Raymond, W. H., Wade, G. S., and Zapotocny, T. H. (2004). Assimilating GOES Brightness Temperatures. Part I: Upper-Tropospheric Moisture. *J. Appl. Meteor.*, 43(1):17–27. doi:10.1175/1520-0450(2004)043<0017:AGBTPI>2.0.CO;2. (Cited on pages 37 and 38.)

Renshaw, R. and Francis, P. N. (2011). Variational assimilation of cloud fraction in the operational Met Office Unified Model. *Q.J.R. Meteorol. Soc.*, 137(661):1963–1974. doi:10.1002/qj.980. (Cited on pages 39 and 41.)

Rigollier, C., Bauer, O., and Wald, L. (2000). On the clear sky model of the ESRA — European Solar Radiation Atlas — with respect to the heliosat method. *Sol. Energy*, 68(1):33–48. doi:10.1016/S0038-092X(99)00055-9. (Cited on page 71.)

Riihimaki, L., Berg, L. K., Kosovic, B., McCaa, J. R., and Lantz, K. O. (2018). Incorporating Observed Solar Variability into Model Forecasts: New Developments in WRF-Solar v2. AGU Fall Meeting 2018, Washington DC, USA, 10-14 Dec 2018. (Cited on page 9.)

Ruiz-Arias, J. A., Arbizu-Barrena, C., Santos-Alamillos, F. J., Tovar-Pescador, J., and Pozo-Vázquez, D. (2016). Assessing the Surface Solar Radiation Budget in the WRF Model: A Spatiotemporal Analysis of the Bias and Its Causes. *Mon. Wea. Rev.*, 144(2):703–711. doi:10.1175/MWR-D-15-0262.1. (Cited on page 9.)

Sahu, D. K., Yang, H., and Kleissl, J. (2018). Assimilating observations to simulate marine layer stratocumulus for solar forecasting. *Sol. Energy*, 162:454–471. doi:10.1016/j.solener.2018.01.006. (Cited on page 9.)

Sawada, Y., Okamoto, K., Kunii, M., and Miyoshi, T. (2019). Assimilating every-10-minute Himawari-8 infrared radiances to improve convective predictability. *J. Geophys. Res.-Atmos.* doi:10.1029/2018JD029643. (Cited on page 37.)

Schipper, J. and Mathiesen, P. (2015). Advanced Cloud Simulations for Improved Dayahead Solar Power Forecasts. 5th Solar Integration Workshop, Brussels, Belgium. (Cited on page 43.)

Schmela, M., Beauvais, A., Chevillard, N., Guillén Paredes, M., Heisz, M., and Rossi, R. (2018). Global Market Outlook for Solar Power 2018-2022. SolarPower Europe. (Cited on page 2.)

Schomburg, A., Schraff, C., and Potthast, R. (2014). A concept for the assimilation of satellite cloud information in an Ensemble Kalman Filter: single-observation experiments. *Q.J.R. Meteorol. Soc.*, 141(688):893–908. doi:10.1002/qj.2407. (Cited on pages 41, 45 and 49.)

Schraff, C., Reich, H., Rhodin, A., Schomburg, A., Stephan, K., Periáñez, A., and Potthast, R. (2016). Kilometre-scale ensemble data assimilation for the COSMO model (KENDA). *Q. J. Roy. Meteor. Soc.*, 142(696):1453–1472. doi:10.1002/qj.2748. (Cited on pages 33 and 57.)

Seaman, C. J., Sengupta, M., and Vonder Haar, T. H. (2010). Mesoscale satellite data assimilation: impact of cloud-affected infrared observations on a cloud-free initial model state. *Tellus A*, 62(3):298–318. doi:10.1111/j.1600-0870.2010.00436.x. (Cited on pages 30, 31, 34, 36 and 45.)

Sengupta, M., Habte, A., Gueymard, C., Wilbert, S., Renné, D., and Stoffel, T. (2017). Best Practices Handbook for the Collection and Use of Solar Resource Data for Solar Energy Applications: Second Edition. Technical Report, National Renewable Energy Laboratory (NREL). (Cited on pages 4, 6 and 9.)

Shao, H., Derber, J., Huang, X.-Y., Hu, M., Newman, K., Stark, D., Lueken, M., Zhou, C., Nance, L., Kuo, Y.-H., and Brown, B. (2016). Bridging Research to Operations Transitions: Status and Plans of Community GSI. *Bull. Amer. Meteor. Soc.*, 97(8):1427–1440. doi:10.1175/BAMS-D-13-00245.1. (Cited on page 29.)

Shepard, D. (1968). A two-dimensional interpolation function for irregularly-spaced data. In *Proceedings of the 1968 23rd ACM national conference*, pages 517–524, New York, NY, USA, 27-29 August 1968. doi:10.1145/800186.810616. (Cited on page 70.)

Singh, R., Ojha, S. P., Kishtawal, C. M., Pal, P. K., and Kiran Kumar, A. S. (2016). Impact of the assimilation of INSAT-3d radiances on short-range weather forecasts. *Q.J.R. Meteorol. Soc.*, 142(694):120–131. doi:10.1002/qj.2636. (Cited on pages 29 and 30.)

Singh, R., Pal, P. K., and Joshi, P. C. (2010). Assimilation of Kalpana very high resolution radiometer water vapor channel radiances into a mesoscale model. *J. Geophys. Res.-Atmos.*, 115(D18):D18124. doi:10.1029/2010JD014027. (Cited on pages 29, 30 and 48.)

Skamarock, W. C., Klemp, J. B., Dudhia, J., Gill, D. O., Barker, D. M., Duda, M. G., Huang, X.-Y., Wang, W., and Powers, J. G. (2008). A Description of the Advanced Research WRF Version 3. NCAR Technical Note NCAR/TN–475+STR, National Center for Atmospheric Research, Boulder, CO. (Cited on page 9.)

Sommer, M. and Weissmann, M. (2014). Observation impact in a convective-scale localized ensemble transform Kalman filter: Observation Impact in a Convective-Scale LETKF. *Q.J.R. Meteorol. Soc.*, 140(685):2672–2679. doi:10.1002/qj.2343. (Cited on page 33.)

Souto, M. J., Balseiro, C. F., Pérez-Muñuzuri, V., Xue, M., and Brewster, K. (2003). Impact of Cloud Analysis on Numerical Weather Prediction in the Galician Region of Spain. *J. Appl. Meteor.*, 42(1):129–140. doi:10.1175/1520-0450(2003)042<0129:IOCAON>2.0.CO;2. (Cited on page 39.)

SPLEnergiesRéunion (2018). Le bilan énergétique de l'île de La Réunion 2017. (Cited on pages 2 and 3.)

Stöckli, R. (2018). Aerosol Optical Thickness. Maps accessible at https://neo.sci.gsfc.nasa.gov/view.php?datasetId=MYDAL2_m_aer_od. Accessed 2 September 2018. (Cited on page 70.)

Stengel, M., Lindskog, M., Undén, P., and Gustafsson, N. (2013). The impact of cloud-affected IR radiances on forecast accuracy of a limited-area NWP model. *Q.J.R. Meteorol. Soc.*, 139(677):2081–2096. doi:10.1002/qj.2102. (Cited on page 32.)

Stengel, M., Lindskog, M., Undén, P., Gustafsson, N., and Bennartz, R. (2010). An extended observation operator in HIRLAM 4d-VAR for the assimilation of cloud-affected satellite radiances. *Q.J.R. Meteorol. Soc.*, 136(649):1064–1074. doi:10.1002/qj.621. (Cited on page 32.)

Stengel, M., Undén, P., Lindskog, M., Dahlgren, P., Gustafsson, N., and Bennartz, R. (2009). Assimilation of SEVIRI infrared radiances with HIRLAM 4d-Var. *Q.J.R. Meteorol. Soc.*, 135(645):2100–2109. doi:10.1002/qj.501. (Cited on page 32.)

Stensrud, D. J. (2007). *Parameterization Schemes: Keys to Understanding Numerical Weather Prediction Models*. Cambridge University Press, Cambridge. doi:10.1017/CBO9780511812590. (Cited on page 8.)

Suzue, H., Imai, T., and Mouri, K. (2016). High-resolution Cloud Analysis Information derived from Himawari-8 data. Technical Report Meteorological satellite center technical note, No.61. (Cited on page 14.)

Taylor, R. B. E., Renshaw, R. J., Saunders, R. W., and Francis, P. N. (2008). Assimilation of SEVIRI cloud-top parameters in the Met Office regional forecast model. Technical report, Met Office, Exeter, UK. (Cited on pages 39, 41, 42, 43 and 48.)

Thompson, G., Field, P. R., Rasmussen, R. M., and Hall, W. D. (2008). Explicit Forecasts of Winter Precipitation Using an Improved Bulk Microphysics Scheme. Part II: Implementation of a New Snow Parameterization. *Mon. Wea. Rev.*, 136(12):5095–5115. doi:10.1175/2008MWR2387.1. (Cited on page 57.)

Trepte, Q. Z., Minnis, P., Sun-Mack, S., Yost, C. R., Chen, Y., Jin, Z., Chang, F.-L., Smith, William L., J., Bedka, K. M., and Chee, L. (2019). Global cloud detection for CERES Edition 4 using Terra and Aqua MODIS data. *IEEE T. Geosci. Remote.* in review. (Cited on page 61.)

UCAR (2015). WRF Physics Use Survey, Available at http://www2.mmm.ucar.edu/wrf/users/. Accessed 8 January 2019. Technical report. (Cited on page 57.)

Vallance, L., Charbonnier, B., Paul, N., Dubost, S., and Blanc, P. (2017). Towards a standardized procedure to assess solar forecast accuracy: A new ramp and time alignment metric. *Sol. Energy*, 150:408–422. doi:10.1016/j.solener.2017.04.064. (Cited on page 71.)

van der Veen, S. H. (2013). Improving NWP Model Cloud Forecasts Using Meteosat Second-Generation Imagery. *Mon. Wea. Rev.*, 141(5):1545–1557. doi:10.1175/MWR-D-12-00021.1. (Cited on pages 41, 42, 43 and 48.)

van Leeuwen, P. J. (2001). An Ensemble Smoother with Error Estimates. *Mon. Wea. Rev.*, 129(4):709–728. doi:10.1175/1520-0493(2001)129<0709:AESWEE>2.0.CO;2. (Cited on page 50.)

Verbois, H., Huva, R., Rusydi, A., and Walsh, W. (2018). Solar irradiance forecasting in the tropics using numerical weather prediction and statistical learning. *Sol. Energy*, 162:265–277. doi:10.1016/j.solener.2018.01.007. (Cited on pages 11 and 70.)

Vukicevic, T., Greenwald, T., Zupanski, M., Zupanski, D., Vonder Haar, T., and Jones, A. S. (2004). Mesoscale Cloud State Estimation from Visible and Infrared Satellite Radiances. *Mon. Wea. Rev.*, 132(12):3066–3077. doi:10.1175/MWR2837.1. (Cited on page 32.)

Vukicevic, T., Sengupta, M., Jones, A. S., and Vonder Haar, T. (2006). Cloud-Resolving Satellite Data Assimilation: Information Content of IR Window Observations and Uncertainties in Estimation. *J. Atmos. Sci.*, 63(3):901–919. doi:10.1175/JAS3639.1. (Cited on pages 30, 31, 32, 47 and 50.)

Weng, F. (2007). Advances in Radiative Transfer Modeling in Support of Satellite Data Assimilation. *J. Atmos. Sci.*, 64(11):3799–3807. doi:10.1175/2007JAS2112.1. (Cited on page 31.)

Weng, Y. and Zhang, F. (2016). Advances in Convection-Permitting Tropical Cyclone Analysis and Prediction through EnKF Assimilation of Reconnaissance Aircraft Observations. *Journal of the Meteorological Society of Japan. Ser. II*, 94(4):345–358. doi:10.2151/jmsj.2016-018. (Cited on page 37.)

Weygandt, S., Benjamin, S. G., Dévényi, D., Brown, J. M., and Minnis, P. (2006). Cloud and hydrometeor analysis using metar, radar, and satellite data within the RUC/Rapid-Refresh model. In *Proceedings of the 12th Conference on Aviation Range and Aerospace Meteorology*, Atlanta, GA, USA. American Metrological Society. (Cited on page 50.)

White, A. T., Pour-Biazar, A., Doty, K., Dornblaser, B., and McNider, R. T. (2018). Improving Cloud Simulation for Air Quality Studies Through Assimilation of Geostationary Satellite Observations in Retrospective Meteorological Modeling. *Mon. Wea. Rev.*, 146:29–48. doi:10.1175/MWR-D-17-0139.1. (Cited on pages 41, 42 and 49.)

Xu, D., Auligné, T., and Huang, X.-Y. (2015). A validation of the multivariate and minimum residual method for cloud retrieval using radiance from multiple satellites. *Adv. Atmos. Sci.*, 32(3):349–362. doi:10.1007/s00376-014-3258-5. (Cited on page 44.)

Yang, C., Liu, Z., Gao, F., Childs, P. P., and Min, J. (2017). Impact of assimilating GOES imager clear-sky radiance with a rapid refresh assimilation system for convection-permitting forecast over Mexico. *J. Geophys. Res.-Atmos.*, 122(10):5472–5490. doi:10.1002/2016JD026436. (Cited on pages 29 and 30.)

Yang, H. and Kleissl, J. (2016). Preprocessing WRF initial conditions for coastal stratocumulus forecasting. *Sol. Energy*, 133:180–193. doi:10.1016/j.solener.2016.04.003. (Cited on pages 9, 11 and 43.)

Ying, Y., Zhang, F., and Anderson, J. L. (2018). On the Selection of Localization Radius in Ensemble Filtering for Multiscale Quasigeostrophic Dynamics. *Mon. Wea. Rev.*, 146(2):543–560. doi:10.1175/MWR-D-17-0336.1. (Cited on page 80.)

Yucel, I., James Shuttleworth, W., Gao, X., and Sorooshian, S. (2003). Short-Term Performance of MM5 with Cloud-Cover Assimilation from Satellite Observations. *Mon. Wea. Rev.*, 131(8):1797–1810. doi:10.1175//2565.1. (Cited on pages 40, 41 and 48.)

Yucel, I., Shuttleworth, W. J., Pinker, R. T., Lu, L., and Sorooshian, S. (2002). Impact of Ingesting Satellite-Derived Cloud Cover into the Regional Atmospheric Modeling System. *Mon. Wea. Rev.*, 130(3):610–628. doi:10.1175/1520-0493(2002)130<0610:IOISDC>2.0.CO;2. (Cited on pages 9, 39, 40, 41 and 42.)

Zapotocny, T. H., Menzel, W. P., Jung, J. A., and Nelson, J. P. (2005). A Four-Season Impact Study of Rawinsonde, GOES, and POES Data in the Eta Data Assimilation System. Part I: The Total Contribution. *Wea. Forecasting*, 20(2):161–177. doi:10.1175/WAF837.1. (Cited on page 48.)

Zhang, F., Weng, Y., Sippel, J. A., Meng, Z., and Bishop, C. H. (2009). Cloud-Resolving Hurricane Initialization and Prediction through Assimilation of Doppler Radar Observations with an Ensemble Kalman Filter. *Mon. Wea. Rev.*, 137(7):2105–2125. doi:10.1175/2009MWR2645.1. (Cited on page 37.)

Zhang, Y., Zhang, F., and Stensrud, D. J. (2018). Assimilating All-Sky Infrared Radiances from GOES-16 ABI using an Ensemble Kalman Filter for Convection-Allowing Severe Thunderstorms Prediction. *Mon. Wea. Rev.* doi:10.1175/MWR-D-18-0062.1. (Cited on pages 37 and 57.)

Zhou, X., Liu, Y., Lin, W., Endo, S., and Yoo, S. (2018). Exploring Effects of Cloud Microphysics and Domain Size on Surface Solar Radiation Using a New WRF-Solar Based Evaluation Framework. AGU Fall Meeting 2018, Washington DC, USA, 10-14 Dec 2018. (Cited on pages 56 and 70.)

Zhu, M., Leeuwen, V., J, P., and Zhang, W. (2017). Estimating model error covariances using particle filters. *Q.J.R. Meteorol. Soc.* doi:10.1002/qj.3132. (Cited on page 22.)

Zou, X. and Da, C. (2014). An objective regional cloud mask algorithm for GOES infrared imager radiance assimilation. *J. Geophys. Res.-Atmos.*, 119(11):6666–6680. doi:10.1002/2014JD021455. (Cited on page 29.)

Zou, X., Qin, Z., and Weng, F. (2011). Improved Coastal Precipitation Forecasts with Direct Assimilation of GOES-11/12 Imager Radiances. *Mon. Wea. Rev.*, 139(12):3711–3729. doi:10.1175/MWR-D-10-05040.1. (Cited on pages 29, 30 and 48.)

Zupanski, D., Zupanski, M., Grasso, L. D., Brummer, R., Jankov, I., Lindsey, D., Sengupta, M., and Demaria, M. (2011). Assimilating synthetic GOES-R radiances in cloudy conditions using an ensemble-based method. *Int. J. Remote Sens.*, 32(24):9637–9659. doi:10.1080/01431161.2011.572094. (Cited on pages 31, 37 and 38.)

POLE RECHERCHE
Ecoles **D**octorales

LETTRE D'ENGAGEMENT DE NON-PLAGIAT

Je, soussigné(e) Frederik KURZROCK……, en ma qualité de doctorant(e) de l'Université de La Réunion, déclare être conscient(e) que le plagiat est un acte délictueux passible de sanctions disciplinaires. Aussi, dans le respect de la propriété intellectuelle et du droit d'auteur, je m'engage à systématiquement citer mes sources, quelle qu'en soit la forme (textes, images, audiovisuel, internet), dans le cadre de la rédaction de ma thèse et de toute autre production scientifique, sachant que l'établissement est susceptible de soumettre le texte de ma thèse à un logiciel anti-plagiat.

Fait à Saint-Pierre, le (date) 06/05/2019

Signature : 

Extrait du Règlement intérieur de l'Université de La Réunion
(validé par le Conseil d'Administration en date du 11 décembre 2014)

Article 9. Protection de la propriété intellectuelle – Faux et usage de faux, contrefaçon, plagiat

L'utilisation des ressources informatiques de l'Université implique le respect de ses droits de propriété intellectuelle ainsi que ceux de ses partenaires et plus généralement, de tous tiers titulaires de tels droits.
En conséquence, chaque utilisateur doit :
- utiliser les logiciels dans les conditions de licences souscrites ;
- ne pas reproduire, copier, diffuser, modifier ou utiliser des logiciels, bases de données, pages Web, textes, images, photographies ou autres créations protégées par le droit d'auteur ou un droit privatif, sans avoir obtenu préalablement l'autorisation des titulaires de ces droits.

La contrefaçon et le faux
Conformément aux dispositions du code de la propriété intellectuelle, toute représentation ou reproduction intégrale ou partielle d'une œuvre de l'esprit faite sans le consentement de son auteur est illicite et constitue un délit pénal.
L'article 444-1 du code pénal dispose : « Constitue un faux toute altération frauduleuse de la vérité, de nature à causer un préjudice et accomplie par quelque moyen que ce soit, dans un écrit ou tout autre support d'expression de la pensée qui a pour objet ou qui peut avoir pour effet d'établir la preuve d'un droit ou d'un fait ayant des conséquences juridiques ».
L'article L335_3 du code de la propriété intellectuelle précise que : « Est également un délit de contrefaçon toute reproduction, représentation ou diffusion, par quelque moyen que ce soit, d'une œuvre de l'esprit en violation des droits de l'auteur, tels qu'ils sont définis et réglementés par la loi. Est également un délit de contrefaçon la violation de l'un des droits de l'auteur d'un logiciel (…) ».

Le plagiat est constitué par la copie, totale ou partielle d'un travail réalisé par autrui, lorsque la source empruntée n'est pas citée, quel que soit le moyen utilisé. Le plagiat constitue une violation du droit d'auteur (au sens des articles L 335-2 et L 335-3 du code de la propriété intellectuelle). Il peut être assimilé à un délit de contrefaçon. C'est aussi une faute disciplinaire, susceptible d'entraîner une sanction.
Les sources et les références utilisées dans le cadre des travaux (préparations, devoirs, mémoires, thèses, rapports de stage…) doivent être clairement citées. Des citations intégrales peuvent figurer dans les documents rendus, si elles sont assorties de leur référence (nom d'auteur, publication, date, éditeur…) et identifiées comme telles par des guillemets ou des italiques.
Les délits de contrefaçon, de plagiat et d'usage de faux peuvent donner lieu à une sanction disciplinaire indépendante de la mise en œuvre de poursuites pénales.